PROGRAMA DE PÓS-GRADUAÇÃO EM ENGENHARIA MECÂNICA
CENTRO TECNOLÓGICO
PRÓ-REITORIA DE PESQUISA E PÓS-GRADUAÇÃO
UNIVERSIDADE FEDERAL DO ESPÍRITO SANTO

Manuelle Corbani Romero

TRIBOLOGICAL BEHAVIOR OF ZnO@GO CORE-SHELL NANOPARTICLES AS WATER-BASED LUBRICANT ADDITIVES AND IN COMPOSITE COBALT-BASED COATINGS PREPARED VIA CATHODIC PLASMA ELECTROLYTIC DEPOSITION.

Vitória, ES
2023

PROGRAMA DE PÓS-GRADUAÇÃO EM ENGENHARIA MECÂNICA
CENTRO TECNOLÓGICO
PRÓ-REITORIA DE PESQUISA E PÓS-GRADUAÇÃO
UNIVERSIDADE FEDERAL DO ESPÍRITO SANTO

Manuelle Corbani Romero

TRIBOLOGICAL BEHAVIOR OF ZnO@GO CORE-SHELL NANOPARTICLES AS WATER-BASED LUBRICANT ADDITIVES AND IN COMPOSITE COBALT-BASED COATINGS PREPARED VIA CATHODIC PLASMA ELECTROLYTIC DEPOSITION.

Tese apresentada ao Programa de Pós Graduação em Engenharia Mecânica da Universidade Federal do Espírito Santo, como requisito parcial para obtenção do Grau de Doutor em Engenharia Mecânica.

Orientador: Prof. Dr.Cherlio Scandian
Coorientador: Prof. Dr.André Paulo Tschiptschin

Vitória, ES

2023

PROGRAMA DE PÓS-GRADUAÇÃO EM ENGENHARIA MECÂNICA
CENTRO TECNOLÓGICO
UNIVERSIDADE FEDERAL DO ESPÍRITO SANTO

TRIBOLOGICAL BEHAVIOR OF ZnO@GO CORE-SHELL NANOPARTICLES AS WATER-BASED LUBRICANTS ADDITIVE AND IN COMPOSITE COBALT-BASED COATINGS PREPARED VIA CATHODE PLASMA ELECTROLYSIS DEPOSITION

MANUELLE CORBANI ROMERO

COMISSÃO EXAMINADORA

Prof. Dr. Cherlio Scandian
(Orientador – PPGEM/UFES)

Prof. Dr. André Paulo Tschiptschin
(Coorientador - USP)

Prof. Dr. Nathan Fantecelle Strey
(Examinador Interno - UFES)

Drª. Valdicleide Silva e Mello
(Examinadora Interna – PPGEM/UFES)

Profª. Drª. Henara Lillian Costa Murray
(Examinadora Externa – FURG)

Profª. Drª. Lúcia Vieira
(Examinadora Externa - UNIVAP)

Tese apresentada ao Programa de Pós-Graduação em Engenharia Mecânica da Universidade Federal do Espírito Santo como parte dos requisitos necessários à obtenção do título de Doutor em Engenharia Mecânica

Vitória/ES, 22 de junho de 2023

Datas e horários baseados em Brasília, Brasil
Sincronizado com o NTP.br e Observatório Nacional (ON) em 29/06/2023 às 11:45:20

Documentos TESE Manuelle Corbani Romero

Data e Hora de Criação: 23/06/2023 às 16:10:17

Documentos que originaram esse envelope:

- Avaliac¸a~o CAPES tese Manuelle Corbani Romero _preenchido.pdf (Arquivo PDF) - 1 página(s)
- Comissão Examinadora MANUELLE CORBANI ROMERO.pdf (Arquivo PDF) - 1 página(s)
- Ata 19 TESE Manuelle Corbani Romero.pdf (Arquivo PDF) - 1 página(s)

Hashs únicas referente à esse envelope de documentos

[SHA256]: 671d0a11bcb68bb4e3d7cde8e6474f229df84f9bdb3b953c919160f1ae2f6c04
[SHA512]: ae63404ca8906ac3e0d0ce795761a34bfbf3e21c75a0460b09ef88caddf64a08e081cdecfb0cf9f7e22835ac657324668f2cb1d5ebaaf9f6aa7c4c2134cf6e46

Lista de assinaturas solicitadas e associadas à esse envelope

☑ **ASSINADO - André Paulo Tschiptschin (antschip@usp.br)**
Data/Hora: 24/06/2023 - 07:09:04, IP: 177.81.33.220, Geolocalização: [-23.540297, -46.709224]
[SHA256]: c7f81b44aebd93370a642f7f086627c9df8551fba16424d35dbbce23f9453518

☑ **ASSINADO - Cherlio Scandian (cherlio@hotmail.com)**
Data/Hora: 23/06/2023 - 16:56:25, IP: 200.137.65.108
[SHA256]: 80ebde1e227c4931e319b95c413eb73def516b114b1804b2a4b3e2a92e705631

☑ **ASSINADO - Henara Lillian Costa Murray (henaracosta@furg.br)**
Data/Hora: 23/06/2023 - 18:00:34, IP: 177.22.171.96, Geolocalização: [-31.757596, -52.273543]
[SHA256]: 3ebc92938c5d3ebc171cbb40dd7d13e1b7218b4212b733206c87c194699273a7

☑ **ASSINADO - Lúcia Vieira (lucia.vieira@univap.br)**
Data/Hora: 24/06/2023 - 07:20:15, IP: 201.95.149.251, Geolocalização: [-23.142931, -45.785278]
[SHA256]: e4edf8b215c572303e2e532c55273d0ccfc89e0affcca8d8cd1f09e7bb06da44

☑ **ASSINADO - Nathan Fantecelle Strey (nathan.strey@ufes.br)**
Data/Hora: 24/06/2023 - 14:46:30, IP: 200.137.65.104
[SHA256]: cea4b01c91629fea1ba78be6cc7479c58b95f66bbf7e00fc64441e8ed5250a6c

☑ **ASSINADO - Valdicleide Silva e Mello (valdicleide.mello@ufes.br)**
Data/Hora: 29/06/2023 - 11:45:20, IP: 189.94.166.42
[SHA256]: 0ed519b4f9c11e255d2d9b113699fc9e77ac823b79199d019b134f36bdcb8caa

Histórico de eventos registrados neste envelope

29/06/2023 11:45:20 - Envelope finalizado por valdicleide.mello@ufes.br, IP 189.94.166.42
29/06/2023 11:45:20 - Assinatura realizada por valdicleide.mello@ufes.br, IP 189.94.166.42
24/06/2023 14:46:30 - Assinatura realizada por nathan.strey@ufes.br, IP 200.137.65.104
24/06/2023 14:45:52 - Envelope visualizado por nathan.strey@ufes.br, IP 200.137.65.104
24/06/2023 07:20:15 - Assinatura realizada por lucia.vieira@univap.br, IP 201.95.149.251
24/06/2023 07:20:03 - Envelope visualizado por lucia.vieira@univap.br, IP 201.95.149.251
24/06/2023 07:09:04 - Assinatura realizada por antschip@usp.br, IP 177.81.33.220
23/06/2023 18:00:34 - Assinatura realizada por henaracosta@furg.br, IP 177.22.171.96
23/06/2023 18:00:20 - Envelope visualizado por henaracosta@furg.br, IP 177.22.171.96
23/06/2023 16:56:25 - Assinatura realizada por cherlio@hotmail.com, IP 200.137.65.108
23/06/2023 16:56:04 - Envelope visualizado por cherlio@hotmail.com, IP 200.137.65.108
23/06/2023 16:14:07 - Envelope registrado na Blockchain por andreia.eyng@ufes.br, IP 200.137.65.106
23/06/2023 16:14:05 - Envelope encaminhado para assinaturas por andreia.eyng@ufes.br, IP 200.137.65.106
23/06/2023 16:10:19 - Envelope criado por andreia.eyng@ufes.br, IP 200.137.65.106

Ficha catalográfica disponibilizada pelo Sistema Integrado de Bibliotecas - SIBI/UFES e elaborada pelo autor

---

Corbani Romero, Manuelle, 1993-
C789t TRIBOLOGICAL BEHAVIOR OF ZnO@GO CORE SHELL NANOPARTICLES AS WATER-BASED LUBRICANT ADDITIVES AND IN COMPOSITE COBALT BASED COATINGS PREPARED VIA CATHODIC PLASMA ELECTROLYTIC DEPOSITION / Manuelle Corbani Romero. - 2023.
89 f. : il.

Orientador: Cherlio Scandian.
Coorientador: André Paulo Tschiptschin.
Tese (Doutorado em Engenharia Mecânica) - Universidade Federal do Espírito Santo, Centro Tecnológico.

1. Tribologia. 2. Revestimentos - Processos. 3. Nanopartículas. 4. Revestimentos - Processos. 5. Plasma (Gases ionizados). 6. Desgaste mecânico. I. Scandian, Cherlio. II. Tschiptschin, André Paulo. III. Universidade Federal do Espírito Santo. Centro Tecnológico. IV. Título.

CDU: 621

Abstract

Core-shell nanoparticles are hybrid nanostructure. This thesis addresses the electrostatic self-assembly of core-shell nanoparticles with hardcore of ZnO and soft graphene oxide (GO) shells. The assembled structures (ZnO@GO) were used as additive in water-based lubricants and in cobalt-based coatings. In the second chapter, the GO nanoparticles were synthesized and assembled with ZnO using a surface modifier, forming a ZnO@GO core-shell nanostructures. ZnO@GO, GO and ZnO were used as additives in water nanofluids which were wear tested in a ball-on-plate configuration using AISI 52100 as the ball and AISI 304 as the plate. ZnO@GO were efficient in reducing wear by the formation of a GO-rich protective tribolayer. The third chapter regards the production of cobalt coatings by cathodic plasma electrolytic deposition (CPED). The deposition mechanism and the effect of polyethylene glycol (PEG) on it are discussed. CPED was efficient in forming nanocrystalline and wear-resistant coatings. PEG decreased the current needed for deposition and affected the thickness and morphology of coatings, while not altering wear or friction. In the fourth chapter, the ZnO@GO nanoparticles were added to the electrolytic bath forming a composite cobalt-based coating. Coatings were tested against an AISI 52100 ball in sliding wear tests. Nanoparticles increased coatings hardness and decreased surface roughness. Composite coatings had a superior tribological performance when compared to pure Co-coatings due to the entrapment of exfoliated GO nanoparticles on the wear track, protecting the surface.

Keywords: Core-shell; Water-based lubricants; Cathodic Plasma Electrolytic Deposition; Sliding wear; Cobalt coatings; Zinc Oxide; Graphene Oxide.

Dedication

I dedicate this work, foremost, to God the creator of all things seen and unseen. *“For of Him, and through Him, and to Him, are all things: to whom be glory forever. Amen.” Romans 11:36.*

Acknowledgments

First, I have to thank my parents for their endless love, encouragement and support throughout my life. My husband deserves my wholehearted thanks as well for his support and for giving me strength to pursue this dream.

To my BFF friends, Carlos, Rubson, Renan, Adler, Paulo Victor, Pâmella and Val for their companionship. You made the hard times easier.

Professor Cherlio for his guidance during my whole academic life and especially his confidence in me.

Professor Alfredo, Professor Jair, Professor Tschiptschin and MSc. Tainara for their technical support.

Table of Contents

List of figure

List of Table

Nomeclature

AE	Acoustic emission
APTES	(3-aminopropyl)trethoxysilane
DC	Direct current
DI	Distilled water
EDS	Energy-dispersive X-ray spectroscopy
EPD	Electrolytic plasma deposition
FCC	Face-Centered Cubic
FESEM	Field-emission scanning electron microscopy
FTIR	Fourier transform infrared spectroscopy
FWHM	Full width at half maximum
HCP	Hexagonal Closed-Packed
HSC	High speed camera
LIB	Lithium-ion batteries
NP	Nanoparticle
PEG	Polyethylene Glycol
PEO	Plasma Electrolytic Oxidation
PES	Plasma Electrolytic Saturation
rGO	Reduced graphene oxide
TEM	Transmission electron microscopy
WCA	Water contact angle
XRD	X-ray diffraction
ZnO@APTES	APTES-functionalized ZnO
ZnO@GO	Core-shell ZnO and GO nanoparticles

Chapter 1

1. Introduction

Tribology, defined as “The science and technology of interacting surfaces in relative motion – and of associated subjects and practices” (Jost, 1990), has a crucial role on the search for more efficient and sustainable systems and processes. It is divided in three areas: friction, wear and lubrication, which have interdependent phenomena. In sliding components, such as bearing, and joints, low friction is desirable to reduce energy losses and reduce wear, increasing service life [1].

The global economic impact of friction, wear, and lubrication is extremally relevant. About 20% of all energy produced is dissipated as friction thus aiming to obtain efficient systems, friction must be understood and controlled [2]. Attention to tribology, regarding research, education and application can save up to 1.6% of the gross national product (GNP) of an industrialized country [3].

Among the several approaches to reduce friction and enhance wear resistance, the use of coatings has become an increasingly popular option in a range of industrial applications, due to the cost reduction given that allows the use of cheaper materials as substrate. Besides, composite coatings can be manufactured, resulting in unique, and multifunctional properties [4, 5].

Electrodeposition are a versatile and low-cost option for coating manufacturing. In addition, it has high deposition rates and allows efficient control of film thickness and the deposition of components with complex shapes. The plasma electrolysis technique is derived from this group, which combines the conventional electrolysis with atmospheric plasma processing, resulting in coatings with high hardness, high adhesion, nanocrystalline size, wear resistant and corrosion resistant [6, 7].

Nanocrystalline cobalt coatings are well discussed in literature due to its magnetic properties, high hardness and high wear and corrosion resistance. Besides, cobalt is an environmental-friendly alternative to chromium plates which uses a hazardous electrolyte. Tribological behavior of cobalt can be improved by nanoparticles additions, which can seal pores and reduce grain size, wear and corrosion [8, 9].

Graphene is a carbon nanomaterial, known as a promising solid lubricant due to the low friction coefficient observed in several sliding applications. And its tribological properties can be further improved by its wrapping with other nanoparticles, as ceramics [8]. Core-shell structures, using a hardcore, such as ZnO or SiC, with a soft shell, graphene, leads to synergistic effect further reducing friction and wear. This hybrid nanoparticles can be used as additives in environmental-friendly water-based lubricants and could also be added to metallic coatings [10, 11].

1.1. Objectives

Considering the above arguments, the main goal of this thesis is to investigate the contribution to tribological performance of core-shell ZnO@GO nanoparticles when used as additives in water-based lubricants and in composite cobalt coatings deposited by CPED. In order to achieve this goal, the thesis is mainly concerned with:

- The synthesis of ZnO@GO core-shell nanostructure.
- Investigate the effect of ZnO@GO addition in the tribological performance of water-based lubricants.
- Investigate the effect of ZnO@GO addition in the tribological performance of cobalt-based coatings deposited using the CPED.
- Deposit nanocrystalline cobalt-based coatings using CPED method;
- Establish a relationship between CPED process parameters and coating properties.
- Investigate the PEG effect on process parameters and coating deposition;

1.2. Thesis Outline and Contributions

The major points concerning each chapter, which are like article format, are described below:

- Chapter 02:

The chapter is entitled “Tribological behavior of ZnO@GO core-shell nanoparticles as water-based lubricant additive for AISI 52100/AISI 304 steel pair. In this paper, graphene oxide (GO) was synthesized by modified Hummer’s method using graphite from spent ion-lithium batteries as precursor. ZnO@GO core-shell nanoparticles were synthetized by electrostatic self-assembly. The nanoparticles were dispersed in pure water, forming water-based lubricants. ZnO@GO concentration effect on the tribological behavior was determined. Friction and wear performance were investigated in ball-on-plate sliding wear test. Literature concerning core-shell nanoparticles in WBL is scarce. This work shows that additives such as ZnO@GO can increase load bearing capacity, allowing WBL usage in steel contact

- Chapter 03:

The chapter named “Influence of Polyethylene Glycol addition on the deposition and tribological performance of cobalt coatings prepared via cathode plasma electrolytic deposition” presents the production of nanocrystalline cobalt coatings via cathodic plasma electrolysis deposition (CPED). The effect of polyethylene glycol addition on the CPED process, surface morphology, and tribological behavior was determined. Coatings were characterized, and tribological performance was assessed using sliding wear tests. The main contribution of this chapter is the proposed mechanism of coating formation during CPED and its close relationship to a single process parameter: the density of current peaks.

- Chapter 4:

The chapter named “On the tribological behavior of cobalt-based nanocomposite coatings containing ZnO@Graphene oxide core-shell nanoparticles” presents the article published in the journal “Wear”. In this chapter, ZnO@GO core-shell nanoparticles were added to the electrolytic bath and cobalt-based composite coatings were deposited using CPED. The effect of core-shell addition on surface topography, mechanical properties and tribological behavior of coating was investigated. No literature was found regarding the addition of core-shell nanoparticles in coatings prepared via CPED.

References

[1] JOST, P. Tribology: How the word was coined 40 years ago. Tribology and Lubrication Technology, v. 3, p. 24-29, Março 2006.

[2] HOLMBERG, K.; ERDEMIR, A. Global Impact of Friction on Energy Use in Transportation and Industry. Proceedings of the Second Internation Brasilian Conference on Tribology, 2014.

[3] JOST, H. P. Tribology - Origin and Future. Wear, v. 136, p. 1-17, 1990.

[4] TOOSINEZHAD, Amirhosein; ALINEZHADFAR, Mohammad; MAHDAVI, Soheil. Cobalt/graphene electrodeposits: Characteristics, tribological behavior, and corrosion properties. Surface and Coatings Technology, v. 385, p. 125418, 2020.

[5] KHADEM, Mahdi et al. Tribology of multilayer coatings for wear reduction: A review. Friction, v. 5, n. 3, p. 248-262, 2017.

[6] PARFENOV, E. V. et al. Towards smart electrolytic plasma technologies: An overview of methodological approaches to process modelling. Surface and Coatings Technology, v. 269, p. 2-22, 2015.

[7] QUAN, Cheng; HE, Yedong. Microstructure and characterization of a novel cobalt coating prepared by cathode plasma electrolytic deposition. Applied Surface Science, v. 353, p. 1320-1325, 2015.

[8] LIU, Cansen; SU, Fenghua; LIANG, Jizhao. Producing cobalt–graphene composite coating by pulse electrodeposition with excellent wear and corrosion resistance. Applied Surface Science, v. 351, p. 889-896, 2015.

[9] WANG, Liping et al. A comparative study on the tribological behavior of nanocrystalline nickel and cobalt coatings correlated with grain size and phase structure. Materials Chemistry and Physics, v. 99, n. 1, p. 96-103, 2006.

[10] ZHANG, Jiangshan et al. Graphene encapsulated SiC nanoparticles as tribology-favoured nanofillers in aluminium composite. Composites Part B: Engineering, v. 162, p. 445-453, 2019.

[11] REN, Baijing et al. Tribological properties and anti-wear mechanism of ZnO@ graphene core-shell nanoparticles as lubricant additives. Tribology International, v. 144, p. 106114, 2020.

Chapter 2

2. Tribological behavior of ZnO@GO core-shell nanoparticles as water-based lubricant additives for AISI 52100/AISI 304 steel pair.

2.1. Abstract

The tribological performance of ZnO@GO (zinc oxide / graphene oxide) core-shell nanoparticles as water-based lubricant additive was investigated via ball-on-plate sliding wear tests using AISI 52100 and AISI 304 steel types as the ball and the plate materials, respectively. ZnO@GO nanoparticles were synthetized by electrostatic self-assembly and fully characterized using X-ray diffraction, Raman spectroscopy and solid-state nuclear magnetic resonance, among other techniques. The results obtained in the wear tests revealed that the presence of ZnO@GO nanoparticles in water led to a reduction of friction coefficient and wear, which were more significant than the results obtained using ZnO and GO separately. The best tribological performance was achieved using a concentration of 0.3 wt. % ZnO@GO in water, which led to a 25% wear reduction and 0.07 friction coefficient. Delamination of oxide layer was the main wear mechanism when using pure water as lubricant. Raman spectroscopy results showed that, for GO and ZnO@GO nanofluids, a GO protective layer was formed on the worn surface and a decrease in the I_D/I_G ratio was observed, suggesting the occurrence of thermal reduction in the GO layer.

2.2. Introduction

Water-based lubricants (WBL) are an environment-friendly alternative over oil that has been attracting attention, especially in the recent years, due to the increasingly resource scarcity [1, 2]. Water is probably the most economic lubricant. It has unique advantages such as non-inflammability, non-toxicity, large reserves, cleaning, high cooling capacity and safe disposal, such that it has aroused widespread interest from researchers and, to some extent, from the industry [3, 4]. WBL applications include a range of cutting fluids and metalworking fluids [5, 6].

However, water has low viscosity, poor bearing capacity and corrosive properties, especially for steel and related materials, which are commonly used on contact surfaces of machine elements [1, 4, 7]. In an effort to overcome these drawbacks, high-quality additives for water lubricants can be employed to improve tribological performance, allowing WBL to be used in steel contact [7]. Many different nano-additives, such as metals [8], ceramics [9], organic materials [10] and carbon materials [2, 7, 11] are introduced as additives and to improve tribological properties.

Graphene is a single-atom-thick sheet of sp^2 hybridized carbon atoms with a two-dimensional honeycomb lattice derived from a single layer of graphite. Recently, it has become an attractive additive owing to its mechanical performance, high electrical and thermal conductivity, low surface energy and friction and wear reducing properties in various testing conditions [7, 12, 13]. However, due to the π-π stacking and Van der Walls interactions, graphene sheets easily agglomerate, being difficult to disperse them in water. On the other hand, graphene oxide (GO) is a material that can be used as a precursor for large scale production of graphene, which easily dissolves in water and maintains the dispersion for longer periods. GO is a graphene derivative containing a large number of oxygen-containing groups (e.g., hydroxyl, carboxyl, and epoxy groups) attached to the layers, besides water molecules in the interlayer space [14]. The good hydrophilicity of these groups ensures then the enhanced dispersibility of GO in water [4, 7, 12].

Berman et al. [15] reported that the addition of an ethanol solution containing graphene to a self-mated steel pair during sliding wear test resulted in a decrease of wear and friction coefficient by factors of 4 and 6, respectively. A conformal protective coating was formed on the worn surfaces, facilitating shear and reducing tribo-corrosion. Liang et al. [16] were able to disperse in-situ exfoliated graphene in water with the assistance of a non-ionic surfactant. The graphene nanofluid was used to lubricate steel/steel contact under sliding conditions and led to 81.3% and 61.3% reduction of friction and wear, respectively, compared to pure water.

Graphene and GO were used as additive in water to lubricate magnesium alloy/steel contact. Both nanoparticles (NPs) greatly reduced friction and wear, but GO nanofluid exhibited the best tribological performance due to the higher load bearing capacity and lubrication film endurance [17]. Kinoshita et al. [7] also used GO as a WBL on WC ball sliding against stainless steel plate. The GO addition resulted in very low friction coefficient (0.05) and enabled the formation of a protective coating.

Furthermore, combinations of different nanoparticles including graphenic materials can further improve tribological behavior through a synergistic effect [17-19]. Xie et al. [19] mixed SiO_2 and graphene sheets in WBL and observed that the tribological performance was superior to SiO_2 or graphene nanofluids separately. Huang et al. [2] dispersed a combination of GO and Al_2O_3 NPs in water. GO formed a tribo-film that prevented the contact of surface asperities while Al_2O_3 acted as a load bearing to strengthen the GO film, enhancing tribological behavior. The effect of ZrO_2, TiO_2 addition along with GO was investigated on a block-on-ring test. Huang et al. [20] reported that ring roughness affected lubrication performance and the nanoparticles deposited on the surface, preventing surface asperities contact.

Furthermore, nanoparticles can be encapsulated by graphene sheets, forming a core-shell structure. The synergistic effect of a hard core combined with a graphene soft shell has a great potential in the tribological field. Taking advantage of the negatively charged surface of GO sheets, GO can encapsulate other positively charged NPs, forming a core-shell structure by electrostatic self-assembly. Song et al. [11] synthetized core-shell Ag@C nanospheres through a green hydrothermal method. The Ag core provides internal support by a tri-dimensional contact with the carbon shell. The hybrid NPs were used in WBL and exhibited excellent lubricating property.

Yang et al. [21] reported the tribological performance of WBL with GO@PTFE additives. The core-shell solved the poor dispersibility of PTFE nanoparticles and increased the wettability of PTFE. The friction coefficient was 77% lower compared to pure water and lower than PTFE and GO separately.

ZnO@GO core-shell NPs were synthetized by Ren et al. [18]. These NPs were dispersed in ester base oil. ZnO particles were functionalized using PAH solution and GO wrapping occurred through electrostatic assembly. The hard-core and soft-shell NPs further enhanced lubrication performance of oil due to the selfrepairing characteristic of graphene along with the high load carrying capacity of the lubricating film provided by the ZnO core. ZnO is a multifunctional material with a high surface energy, high mechanical and thermal stability [22] that had shown excellent lubricant properties in oil [18]. Literature concerning the use of core-shell nanoparticles as additives to WBL is still scarce.

In this work, ZnO@GO core-shell nanoparticles were synthetized and used in different concentrations as additives in water-based lubricants. GO and ZnO NPs were also dispersed in water by means of comparison. Friction and wear performance were investigated using an AISI 304-AISI 52100 ball-on-plate configuration. In addition, anti-wear and anti-friction mechanisms of NPs and the synergistic effect associated with the core-shell arrangement were discussed by analyzing the wear tracks.

2.3. Materials and methods

2.3.1. Synthesis of GO

GO was prepared by a modified Hummers method [23] using recycled graphite derived from spent lithium-ion batteries (LIBs) used in mobile phones as the precursor [24]. Spent LIBs were dismantled into different components: cathode, anode, organic separator, plastic and metallic shell. The obtained anode consisted of graphite paste deposited on the copper foils. Firstly, the graphite was separated from the copper foil by copper dissolution in concentrated nitric acid solution, then graphite powder was filtered, washed with distilled water and oven-dried at 100°C for 24 h. For the GO synthesis, 1 g of recycled graphite, 0.5 g of $NaNO_3$ and 70 ml of H_2SO_4 were mixed together. The mixture was stirred in an ice bath. Then, 3 g of $KMnO_4$ were added gradually and the solution was stirred for another 2 h. Finally, 3 mL of 30% H_2O_2 were added slowly. Afterwards, the solution was diluted in distilled water until the color of the solution changed from dark brown to bright yellow. The material was then centrifuged at 4000 rpm and washed with distilled water to obtain a dispersion with pH in the range 6-7. The final products, which is the GO, were dried at 60°C for 24 h.

2.3.2. Synthesis of ZnO@GO nanoparticles

ZnO@GO nanoparticles were prepared by electrostatic self-assembly [22, 25]. Firstly, the ZnO nanoparticles (50 nm spherical-shaped nanoparticles supplied by Sigma-Aldrich) were functionalized with (3-aminopropyl)triethoxysilane (APTES) (99%, ChemImpex) to introduce amino groups onto the ZnO surface. To achieve this functionalization, 1 g of ZnO was dispersed in a mixture of 105 ml ethanol and 45 ml distilled water with a magnetic stirrer for 10 min at room temperature; then, 0.2 g of APTES was added to the solution to prepare positively-charged ZnO nanoparticles. The solution was stirred for 7 h at room temperature to promote the hydrolysis of APTES and complete the grafting reaction. The APTES-functionalized ZnO (ZnO@APTES) nanoparticles were centrifuged at 4000 rpm, washed four times with ethanol, and dried at 80°C for 15 h.

To produce the core-shell nanoparticles, 0.5 g of solid GO was added to a mixture of 700 ml distilled water and 35 ml of ethanol. The solution was ultrasonicated for 20 min and stirred for 40 min to obtain a well-dispersed GO aqueous solution. Then, 1 g of ZnO@APTES was added to the solution under stirring for 1 h. The ZnO@GO nanoparticles were obtained by centrifugation at 4000 rpm, followed by washing with ethanol (three times) and drying at 70 °C for 24 h. Finally, the nanoparticles were dispersed into different volumes of distilled water using an ultrasonic probe for 30 min to ensure uniform dispersion, in order to obtain lubricants with additives at different mass fractions. The amounts of ZnO@GO used as lubricant nanoadditives in water were 0.1, 0.2, 0.3 and 0.4 wt. %. For comparison with the lubrication performance of the developed water-based lubricants, distilled water and mixtures containing 0.1 wt. % GO and 0.1 wt. % ZnO dispersed into distilled water were also used as lubricants.

2.3.3. Characterization of nanoparticles

GO, ZnO and ZnO@GO samples were analyzed by a suite of physicochemical characterization methods, as detailed in the sequence. Raman spectra were recorded using a LabRam HR Evolution spectrometer from Horiba, using a 633 nm laser, 50x objective and 90 mW laser power. The Fourier-transform infrared (FTIR) spectroscopy analyses were carried out using a Perkin Elmer FTIR Spectrum 400 spectrometer with the KBr pellet technique. X-ray diffraction (XRD) measurements were undertaken on a Rigaku Ultima diffractometer using molybdenum radiation ($\lambda = 7.0926\ \mathrm{nm}$) to identify the crystalline phases present in the material. Solid-state ^{13}C NMR experiments were conducted at room temperature in a Varian/Agilent VNMR 400 MHz spectrometer (NMR frequency of 100.52 MHz, magnetic field of 9.4 T), with the powdered samples packed into 4 mm diameter zirconia rotors for magic angle spinning (MAS) experiments at the spinning rate of 14 kHz; the spectra were recorded using direct excitation of the ^{13}C nuclei (π/2 pulse of 4.3 µs), with a recycle delay of 15 s and accumulation of ca. 4000 transients; the chemical shifts were referenced to tetramethylsilane (TMS), using hexamethylbenzene as a secondary reference (signal at 17.3 ppm). A FEI-Inspect F50 field-emission scanning electron microscopy (FESEM) equipped with X-ray energy dispersive spectrometer (EDS) was employed to study morphology and composition of the ZnO@GO nanoparticles. A high-resolution electron microscope (HRTEM, JEOL JEM 2100F) with energy dispersive x-ray spectroscopy (EDXS) was also used to characterize the structures.

2.3.4. Tribological tests

Tribological tests were done on a PLINT TE67 tribometer (Phoenix Tribology Ltd, Kingsclere, England) using a reciprocating ball-on-plate configuration with a stroke length of approximately 2.5 mm, a sliding frequency of 3 Hz, a load of 850 N and rubbing time of 90 min. Test parameters were chosen after preliminary tests. The initial Hertz contact pressure was calculated to be approximately 2.9 GPa. A single AISI 52100 steel ball with a diameter of 11 mm rolled on a rectangular-shaped AISI 304 specimen (30x10x3 mm^3) [2]. The average surface roughness (R_a) of the body and counter-body were measured using a 2D profilometer. R_a values of the ball and the plate were 0.15 and 0.17 µm, respectively. The sample was completely submerged in lubricant fluid, as shown in the scheme (Figure 2-1). The lubricant volume used was 20 ml. Three replicates were done for each studied lubricant and tests were conducted in randomized order.

The worn surfaces of the plate were investigated by SEM, energy dispersive X-ray spectroscopy (EDS) and Raman spectroscopy. At the end of the tests, mass loss was measured with a precision balance. Friction force was monitored through a load cell (resolution: 0.3 N). The thickness of the nanofluid film was calculated by Hamrock-Dowson model [26].

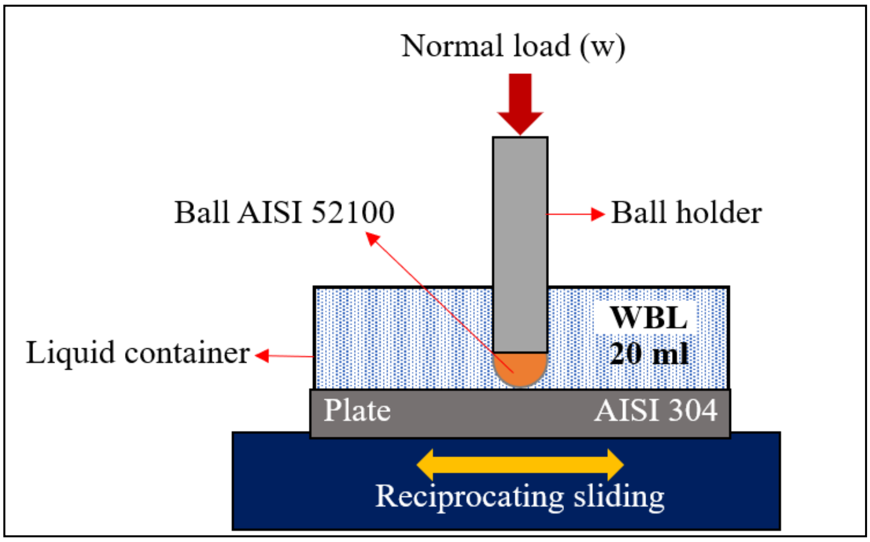

Figure 2-1 – Schematic of the ball-on-plate reciprocating tribometer used for lubricated tests.

2.4. Results and Discussion

2.4.1. Samples characterization

Raman spectra of GO, ZnO and the hybrid ZnO@GO are shown in Figure 2-2. The GO spectrum exhibits 2 strong characteristic peaks, known as D band (at 1337 cm^{-1}) and G band (at 1584 cm^{-1}). The D band is associated with the breathing mode of rings of sp^2 carbon atoms in regions limited in size and/or containing structural defects; on the other hand, the G band corresponds to the in-plane stretching of C=C bonds [27, 28]. The ratio of the intensities of these two bands (named I_D/I_G ratio) is thus frequently taken as an indication of the disorder present in a graphene-like layer [29]. The Raman spectrum obtained for the GO sample (shown in Figure 2-2) exhibits an I_D/I_G ratio of 1.22, confirming that, during the oxidation of graphite, sp^3 carbon sites (associated with oxygen-containing functional groups) and other defects, vacancies and structural distortions occur [13, 30, 31]. The Raman spectrum of ZnO reflects the formation of hexagonal wurtzite ZnO. The peak at 339 cm^{-1} corresponds to A1 vibration mode, while the peak at 441 cm^{-1} represents E2 high non-polar mode associated with oxygen atoms vibration [30]. Besides these peaks, a broad band around 1154 cm^{-1} is related to the A1 transversal optical (TO) and longitudinal optical (LO) modes [13].

All these peaks are also present in the ZnO@GO Raman spectrum; However, they are shifted to lower frequencies, A1 (326 cm^{-1}) and E2^{H} (433 cm^{-1}). This effect can be attributed to the relaxation of lattice stress in the ZnO core promoted by the formation of a GO shell [32]. The D and G bands due to GO are also detected in the ZnO@GO Raman spectrum, with nearly the same intensities observed for the GO sample ($I_D/I_G = 1.22$).

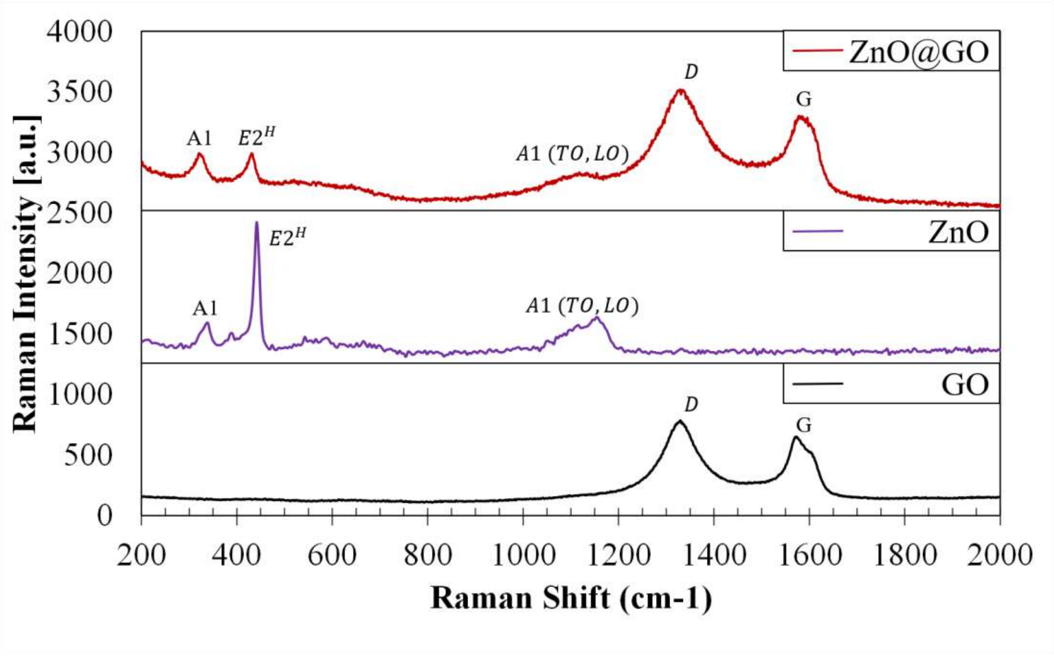

Figure 2-2 – Raman spectra of GO, ZnO and ZnO@GO samples.

XRD patterns of GO, ZnO and ZnO@GO samples are shown in Figure 2-3. The diffraction peaks observed in the case of the ZnO sample clearly show the formation of the hexagonal wurtzite phase, with the Miller indices corresponding to each set of lattice planes also indicated in Figure 2-3 [13]. The XRD pattern obtained for the ZnO@GO sample shows a combination of Bragg peaks due to ZnO and GO. A wide peak at 2θ = 11.2° in the ZnO@GO pattern confirms the presence of the GO structure, with an interlayer spacing (d-spacing) of 0.79 nm. This value is in good agreement with the range of d-spacing values expected for GO samples with high degree oxidation, which are typically above 0.7 nm [30, 31].

The average crystalline size of ZnO sample calculated using Scherrer's equation is 51.2 nm while ZnO@GO sample size is 44.3 nm. A decrease on ZnO particle size is possibly due to the core shell formation, where GO wraps around ZnO core, making ZnO unit cells closer [30].

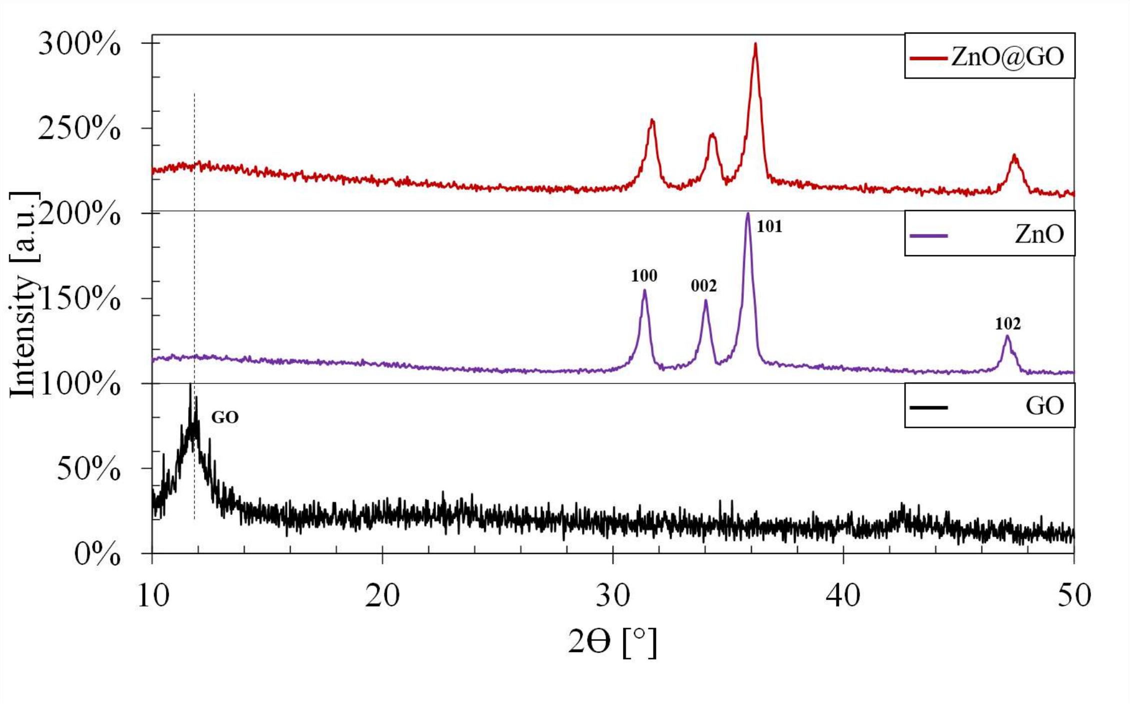

Figure 2-3 - XRD patterns of GO, ZnO and ZnO@GO samples.

The FTIR spectra of ZnO, functionalized ZnO (ZnO@APTES), GO and ZnO@GO samples are shown in Figure 2-4. For ZnO a broad peak at 3447 cm^{-1} attributed to O-H bond can be observed. The absorption band characteristic of the Zn-O bond can be observed at 690 cm^{-1} [33]. The FTIR spectrum of the sample functionalized with APTES (ZnO@APTES sample) exhibits a broad peak at 3270 cm^{-1}, attributed to O-H and N-H bonds [34], besides a new peak at 1062 cm^{-1}, associated with the Si-O- bonds of the ligand, and the band around 690 cm^{-1} due to the Zn-O bond. The GO spectrum shows peaks at 1727 cm^{-1} (C=O bond), 1590 cm^{-1} (C=C bond), 1232 cm^{-1} and 1050 cm^{-1} (C-O-C and C-OH bonds, respectively) [12, 35]. There is also a peak in the GO FTIR spectrum at 3412 cm^{-1}, associated with the stretching of O-H bonds in water molecules and in C-OH groups present in the GO structure. Finally, the FTIR spectrum of the ZnO@GO sample contains almost all peaks observed in the GO spectrum, besides the weak contributions due the Si-O- and Zn-O bonds, confirming the successful presence of the functionalized ZnO NPs embedded into the GO structure [34].

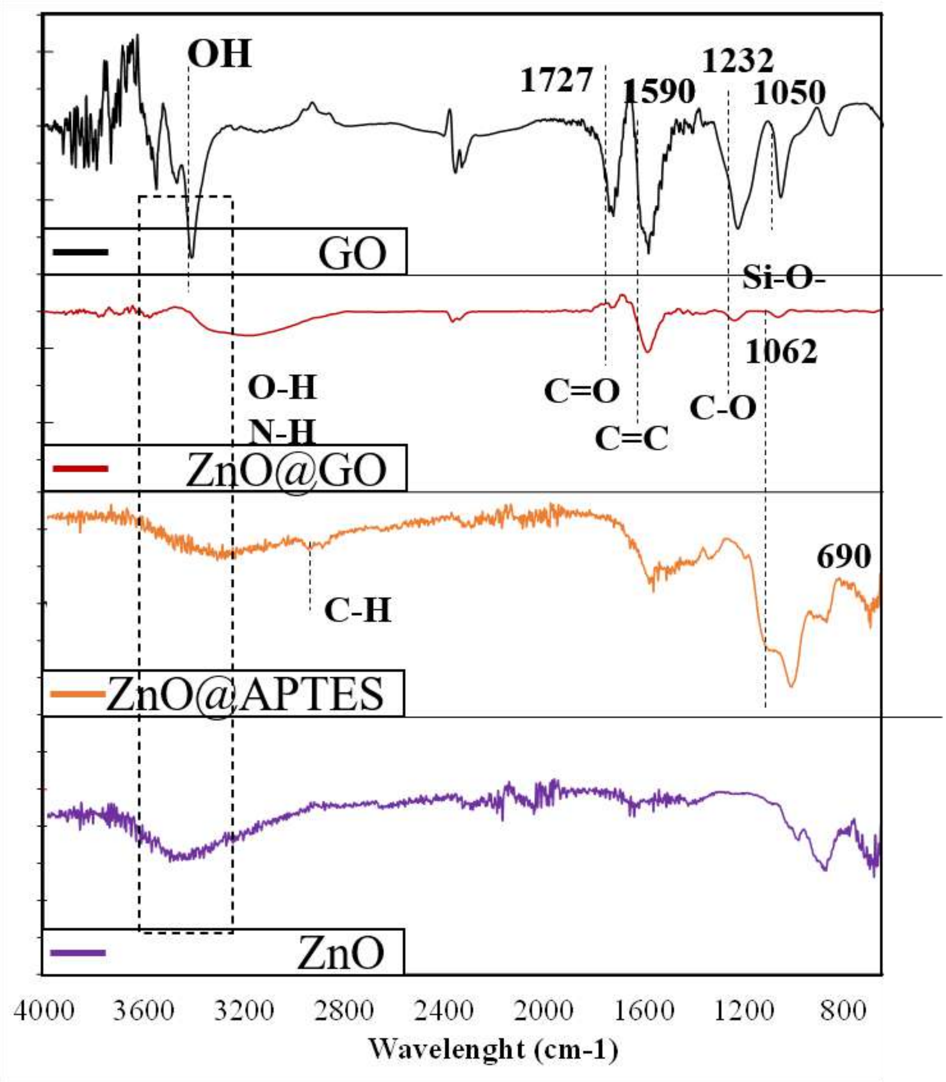

Figure 2-4 - FTIR spectra of ZnO, APTES-functionalized ZnO (ZnO@APTES), GO and ZnO@GO samples.

FESEM micrographs of ZnO@GO NPs are shown in Figure 2-5. ZnO particles are anchored on GO sheets and a uniform distribution of those particles on the hybrid was achieved. The GO sheets seem to be easily agglomerated in large sheets, so that it is not possible to measure the actual sheet size in the lubricant by this technique. TEM image of TEM image of ZnO@GO NPs (Figure 2-6) the wrapping of ZnO NPs by a thin layer of GO. The EDXS (Figure 2-7) analysis at nanometer scale confirms that Zn, C and O are the dominant elements present in the material, with no significant impurities detected. Besides, Zn is concentrated in the core as can be seen in the mapping of Zn of Figure 2-7. All above indicates that the successful formation of the core-shell structure.

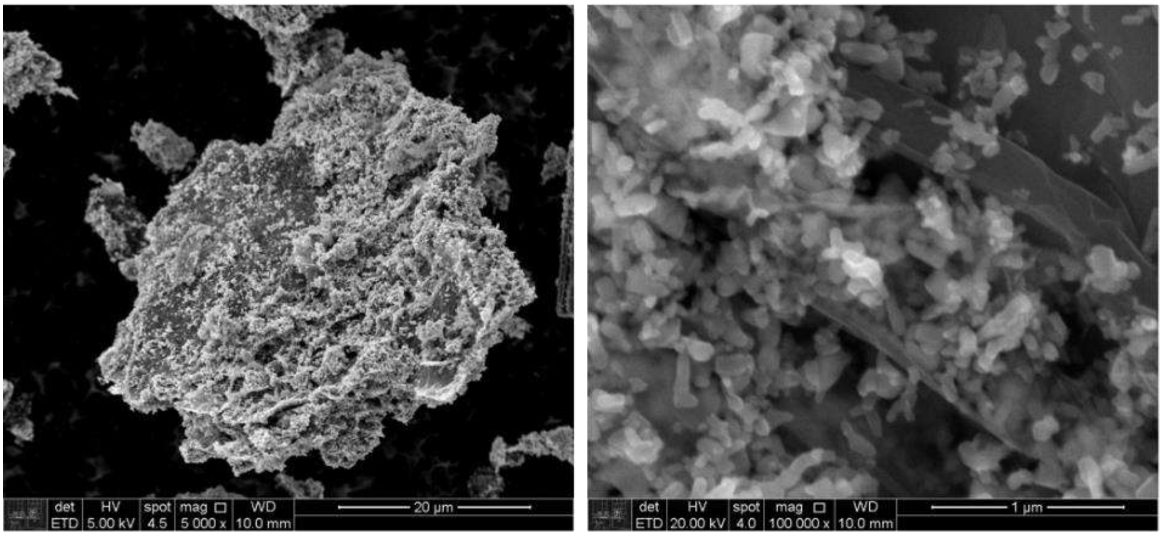

Figure 2-5 – FESEM micrographs and EDS mapping of ZnO@GO sample.

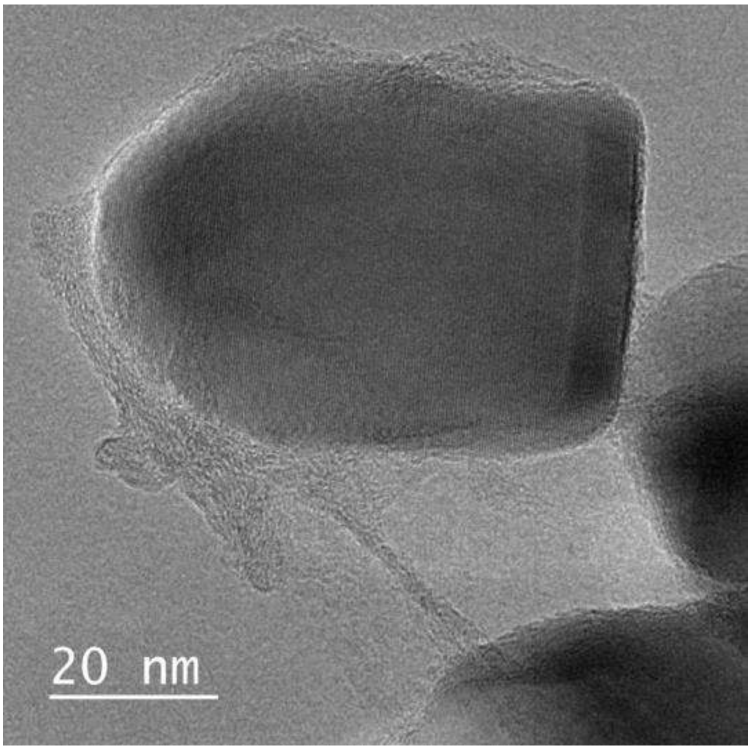

Figure 2-6 – TEM image of ZnO@GO nanoparticle.

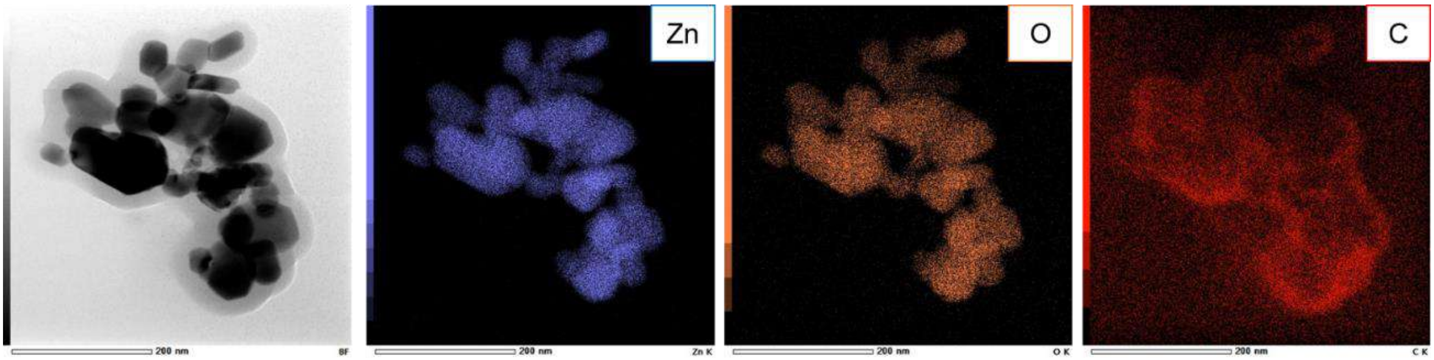

Figure 2-7 - EDXS of ZnO@GO nanoparticles with elemental mapping of Zn, O and C.

Figure 2-8 shows the solid-state ^{13}C NMR spectra recorded for the synthesized GO and ZnO@GO samples. The spectra exhibit some typical signals associated with the GO structure, at the following approximate chemical shifts: 60 ppm: C-O-C (epoxy) groups; 70 ppm: C-OH groups; 100 ppm: lactols; 130 ppm: C=C bonds in sp^2-hybridized regions; 170 and 195 ppm: carbonyl groups in esters (or carboxylic acids) and ketones, respectively [36-38].

The spectrum obtained for the ZnO@GO sample shows a severe decrease in the intensity of the signals associated with the oxygen-containing functions (such as C-O-C and C-OH groups). This could indicate the occurrence of some chemical reduction in the GO structure, with the consequent removal of the originally present oxygen-containing groups, as a consequence of the interaction with the APTES-functionalized ZnO particles. This effect is also accompanied by a decrease in the chemical shift of the signal associated with the sp^2 carbons, reaching 121 ppm in the case of ZnO@GO as opposed to 132 ppm in the ^{13}C NMR spectrum of the GO precursor. Such behavior is related to the effects caused by the circulation of electrons in the sp^2 regions whose size grows with the removal of the oxygen-containing groups, as it has been previously observed in other GO-systems involving functionalization with amine, sulfonic and other groups [39, 40].

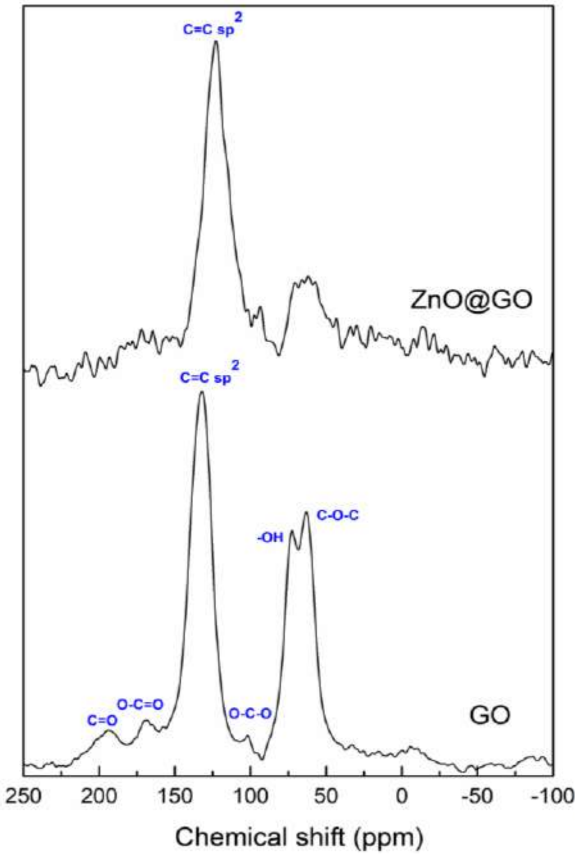

Figure 2-8 - Solid-state ^{13}C NMR spectra of GO and ZnO@GO samples.

As shown in Figure 2-9, a good dispersion and stability of the nanofluids were obtained. No particle precipitation could be observed after 7 days, except for fluids containing ZnO, where agglomerated particles are seen in the bottom.

Figure 2-9 – Dispersion of ZnO, GO and ZnO@GO in water.

2.4.2. Friction and wear behavior

Friction curves are displayed in Figure 2-10. It can be observed that the addition of 0.1% ZnO did not decrease friction when compared to pure H2O. The 0.1% GO solution exhibited a long running-in period with low friction coefficient (around 0.04) and later stabilization at a higher level (0.08). It is worth mentioning that the duration of the running-period had a large variation between replicates. The effect of concentration of the hybrid ZnO@GO NPs on friction was also investigated and is depicted in Figure 2-10. The influence of hybrid particles mixed the effects observed for 0.1% ZnO and 0.1% GO solutions. At lower concentrations (0.1 and 0.2 %), the friction coefficient did not seem to be affected by the NPs addition, just as occurred for the 0.1% ZnO lubricants. However, as the concentration increased (0.3 and 0.4%), the friction coefficient decreased when compared to water. The friction coefficient retained low values right from the beginning of the test, i.e., short running-in periods were observed, which can be considered as an advantage over the 0.1% GO lubricants.

The lubrication regime can be approximately determined by the value of parameter λ given by the ratio between the theoretical minimum film thickness (h_{min}) and the combined roughness of surfaces of friction pairs (R_q). According to the Stribeck curve, there are three different lubrication regimes: boundary lubrication ($\lambda < 1$), mixed lubrication ($1 < \lambda < 3$) and hydrodynamic lubrication ($\lambda < 3$) [26].

$$\lambda = \frac{h_{min}}{R'} \tag{1}$$

$$h_{min} = 3.63R'(\alpha E')^{0.49}\left(\frac{\eta u}{E'R'}\right)^{0.68}\left(\frac{w}{E'R'^2}\right)^{-0.073}(1 - e^{-0.68k}) \tag{2}$$

$$R' = \sqrt{R_{ball}^2 + R_{plate}^2} \tag{3}$$

Where R’ is the radius of the ball, η is bulk the viscosity (25°C, ≈0.897 cP) [41], E' is the effective modulus of elasticity, w is the applied normal load, u is the sliding speed, α is the viscosity-pressure coefficient ($\alpha = 2.2 \times 10^{-8}\, m^2/N$), k is the elliptical parameter ($k \approx 1.03$) and, R_{ball} and R_{plate} are the surface roughness of ball and plate, respectively. Using the test parameters and materials properties, the theoretical minimum thickness of the lubricant film is 51.12 nm for 850 N and 0.06 m/s. Knowing that the combined roughness is 0.227 µm for the studied friction pair, the calculated λ was 0.225, which is below 1. Hence the tests were carried out under a boundary lubrication regime. In this lubricant regime, the fluid is not sufficiently thick to overcome surfaces asperities. The contact between mating surfaces takes place in a very small contact area, under a high contact pressure.

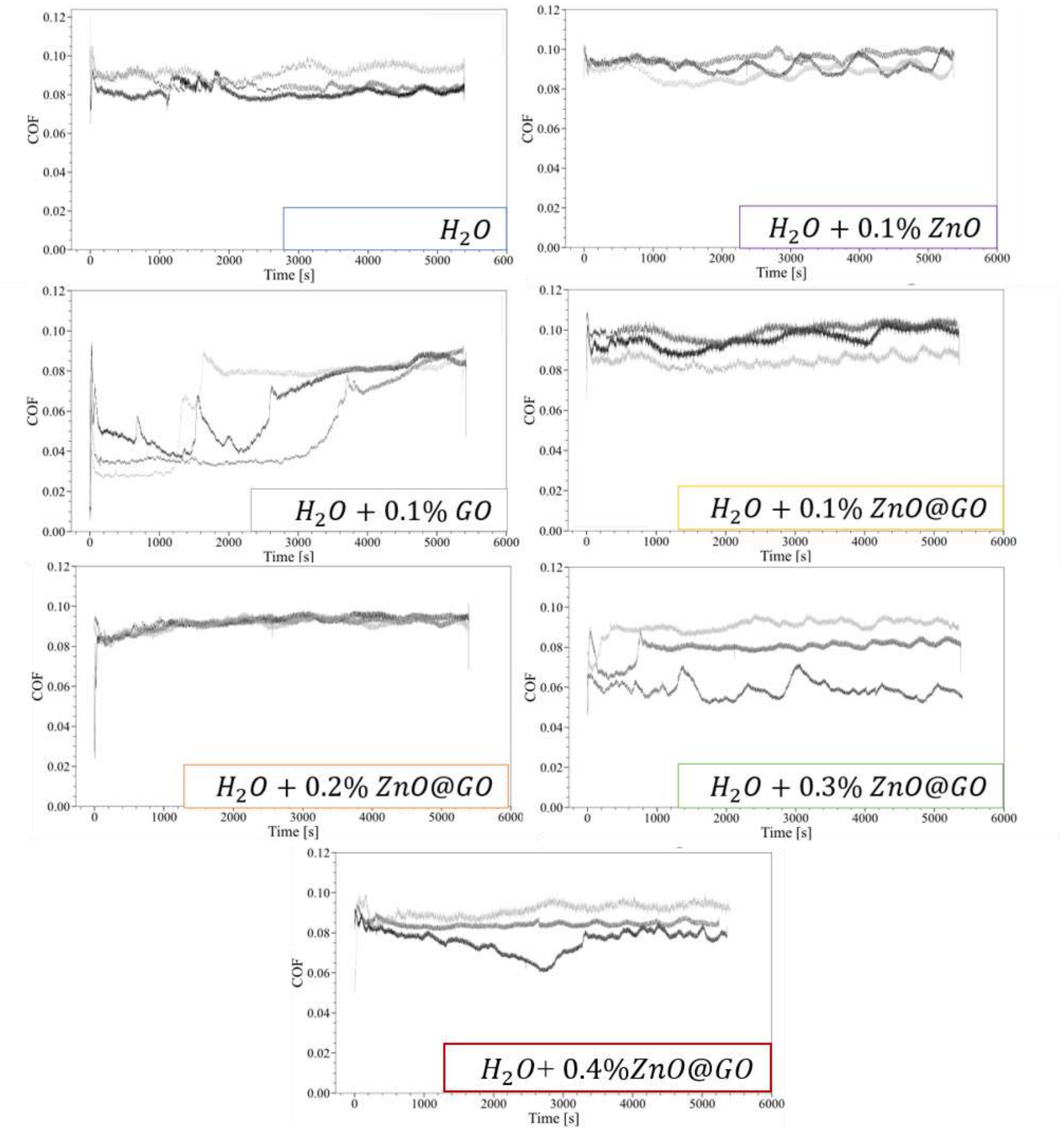

Figure 2-10 - Friction coefficient (COF) curves for WBL: pure H_2O, 0.1% ZnO, 0.1%GO, and ZnO@GO solutions in different concentrations (0.1, 0.2, 0.3 and 0.4%).

NPs affected wear differently from friction. As can be seen in Figure 2-11, despite showing the same friction of pure water, the addition of 0.1% ZnO led to a 60% wear reduction. The 0.1% GO lubricant had a 75 % wear reduction when compared to pure water. Regardless of concentration, the addition of ZnO@GO led to lower wear compared to the other lubricants. The most significant wear reduction (93%) was obtained with the addition of 0.3 % ZnO@GO, whereas the addition of 0.1 and 0.2 % of the hybrid NPs led to the same mass loss. It is evident that ZnO@GO NPs exhibit better wear-reducing abilities than GO and ZnO separately, confirming the synergistic effect of both, GO and ZnO, during sliding process. Ren et al. [18] also reported a superior tribological performance of oil lubricant with ZnO@graphene addition when compared to those with pure ZnO addition, which was attributed to the synergetic effect of both NPs.

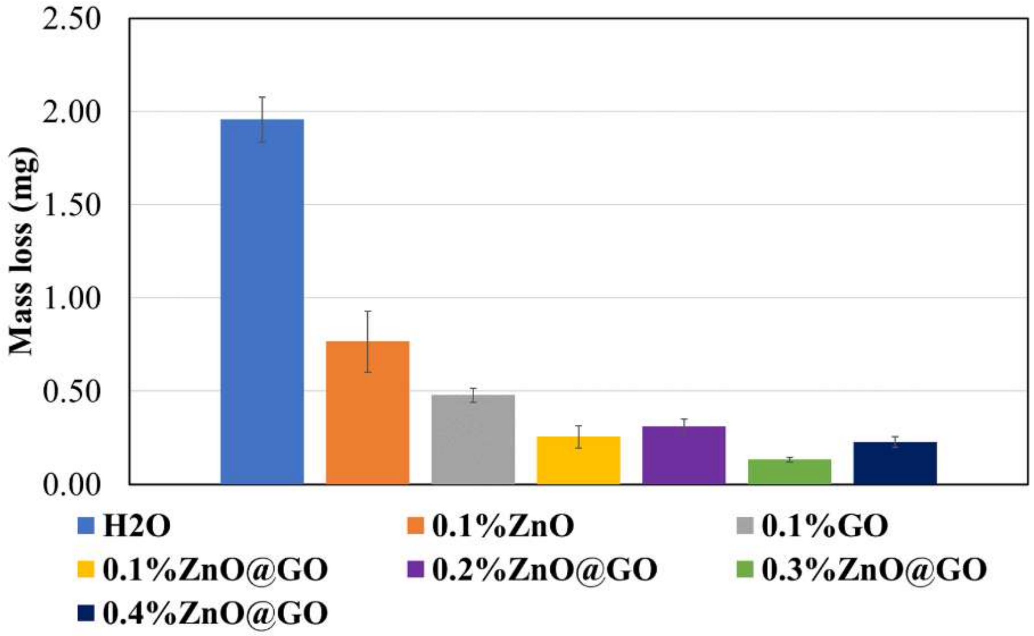

Figure 2-11 - Mass loss of samples tested using different lubricants.

2.4.3. Worn surface analysis

Aiming to better understand how the synergistic effect of ZnO and GO NPs works at the steel/steel interface, the wear tracks were closely examined using FESEM and Raman spectroscopy. Figure 2-12 shows the typical worn surface morphologies formed on AISI 304 plate, along with the corresponding Raman spectra, using pure water, 0.1% ZnO, 0.1% GO and 0.3% ZnO@GO lubricants. It is evident from the images (Figure 2-12, A and B) that the worn surface lubricated with pure water exhibits severe delamination and material removal in the form of plate-like debris. Raman spectrum (Figure 2-12, C) exhibited peaks at 225 cm^{-1}, 337 cm^{-1}, 460 cm^{-1} and 667 cm^{-1} confirming the presence of oxides on the surface. The peak at 225 cm^{-1} refers to hematite formation, while the peak at 667 cm^{-1} corresponds to magnetite formation [42]. Strong peaks at 337 cm^{-1} and 460 cm^{-1} confirm the presence of Cr-enriched spinel type of magnetite [43]. EDS of the oxide layer formed under pure water lubrication confirms the presence of Cr, Fe and O, as shown in Figure 2-13. Kuang et al. [43] showed that oxide films composed of an outer layer of hematite and an inner layer of Cr-enriched magnetite are formed on AISI 304 immersed in oxygenated water at 290 °C for at least 1 h. The dominant wear mechanism is delamination of the oxide film.

With the addition of ZnO (Figure 2-12, D, E and F) to water, delamination is still observed, however, fewer oxide plates had been removed by the end of the test. The dark patches observed in the figure are due to magnetite and Cr-enriched magnetite. No peaks associated with to hematite are found on the worn surface. The increase in wear resistance with ZnO addition can be associated with the formation of a more compact and adherent tribo-film, with no hematite, than in pure water. Besides, ZnO NPs can act as nano-rolling bearing, promoting separation of contact interfaces, and thus increasing the number of cycles needed to remove the oxide plates [18]. However, no effect on friction was observed by the addition of these NPs. Friction is apparently controlled by oxide film formation.

Figure 2-12 G, H, I show the results corresponding to the worn surface lubricated with 0.1% GO fluid. Shallower grooves are seen and the area covered by oxide plates with visible cracks bound to be removed is smaller compared to the cases when 0.1 % ZnO solution and pure water are used as lubricants. Small cracks inside the track indicating delamination wear occur, but in a lesser extent. Raman spectra were recorded on three regions of the worn surface (center and both sides). In two regions, the D band at 1340 cm^{-1} and the G band at 1589 cm^{-1} were present, with an I_D/I_G ratio in the range 0.6-0.7. This indicates that a protective film composed of GO was formed, which explains the lower friction and wear observed for the 0.1 % GO lubricants.

The addition of 0.3% ZnO@GO further enhanced the tribological properties. The worn surface (Figure 2-12, J, K and L) exhibits few abrasion grooves, but, differently from the others nanofluids, delamination is no longer the main wear mechanism and cracks are hardly seen. Oxide formation occur in small regions of the wear track. The strong D and G bands of GO at 1340 and 1589 cm^{-1} are observed in the three analyzed regions, with an I_D/I_G ratio around 0.6-0.7. This confirms the formation of a GO protective layer throughout the whole surface, which is responsible for the superior tribological performance of this lubricant. It is worth noting that no peak attributed to ZnO was detect in any of these Raman spectra, which is probably due the small ZnO amount used in all lubricants and the partial superposition of the ZnO peaks with the peaks due to iron oxides in the Raman spectra.

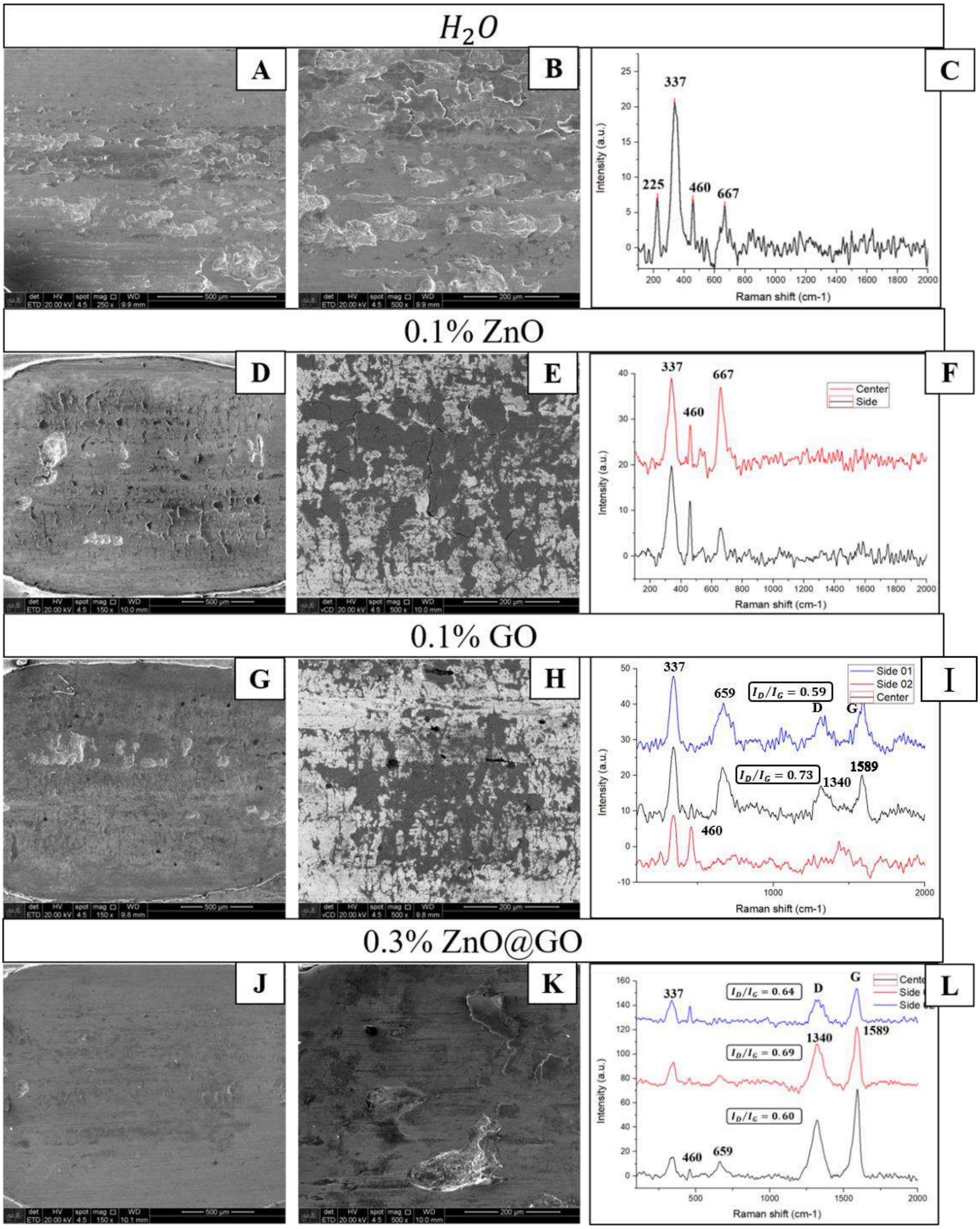

Figure 2-12 - FESEM micrographs and Raman spectra on the wear tracks obtained with the use of pure water (A,B,C), 0.1%ZnO (D,E,F), 0.1%GO (G,H,I), and 03%ZnO@GO (J,K,L) lubricants.

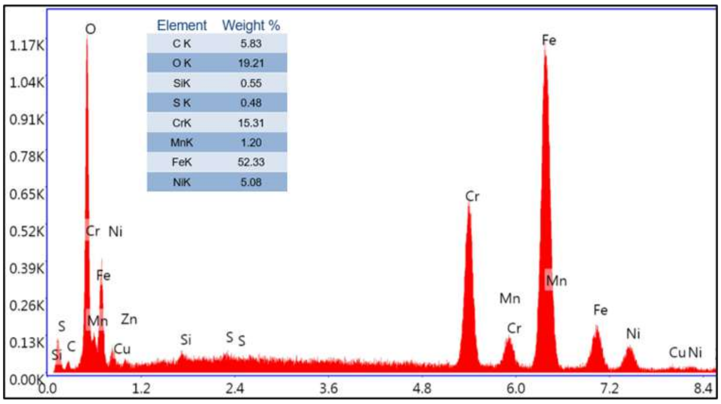

Element	Weight %
C K	5.83
O K	19.21
SiK	0.55
S K	0.48
CrK	15.31
MnK	1.20
FeK	52.33
NiK	5.08

Figure 2-13 - EDS results of oxide layer formed with pure water lubrication.

Pure water lubrication led to formation of tribo-oxide layer on the sliding interface. As rubbing proceeded, the oxide layer broke due to a delamination mechanism and large plate-like debris are removed, increasing wear. With ZnO addition, the oxide layer was still formed, but, given the ZnO action as load-bearing, it took a higher number of cycles to oxide-plates removal. However, ZnO has a low dispersibility in water and agglomeration of these NPs can worsen lubricity and friction behavior. Using 0.1% GO nanofluids, GO was deposited on the surface, forming a protection film. However, by the end of the test, the film had already been damaged and it did not cover the entire worn surface. Despite the high number of oxygen-containing groups of GO that enhance the dispersibility in water, GO sheets restacking and agglomeration are expected [12]. The use of hybrid ZnO@GO NPs prevents the restacking of GO and agglomeration on ZnO. Besides, it is assumed that the hard core (ZnO) works as a rigid skeleton providing a greater load bearing capacity and increased shear friction resistance of the interfacial film [18], while the soft shell (GO) deforms itself and adheres to the surface. As a result, a compact film was formed and maintained until the end of the test, giving to these WBLs outstanding friction and wear resistances.

A decrease of the I_D/I_G ratio (from 1.22 to around 0.6) is observed after the wear tests using 0.1%GO and 0.3%ZnO@GO lubricants. These results indicate that, during sliding, some partial chemical reduction of graphene oxide occurred, leaving the material with an increased contribution of the G band in the Raman spectra. Reduced graphene oxide (rGO) results from the removal of oxygen-containing groups and the growth of sp^2 regions in the material [27, 44]. This phenomenon may have occurred due the high local temperature promoted by the sliding contact. It is interesting to note that a contrasting behavior has been previously reported, i.e., an increase of I_D/I_G ratio during sliding occurred and it has been attributed to an increase of defects on GO structure [2, 17]. However, the contact pressure used on the test and the duration of the test in those works were considerably lower than the ones used here. Xie et al. [17] performed wear tests during 30 min using a 312 MPa Hertzian stress and Huang et al. [12] tested WBL for 2 min at a maximum Hertzian stress of 122 MPa. While in this work, test duration was 90 min and maximum Hertzian stress of 2.9 GPa.

2.5. Conclusions

- GO and ZnO@GO hybrid nanoparticles were successfully synthetized.
- The lubricant produced with 0.3% ZnO@GO showed the lowest friction coefficient (0.07) and 25% wear reduction compared to pure water.
- An oxide layer was formed on the worn surface specially in the case of the samples lubricated with pure water and 0.1%ZnO nanofluids. The presence of magnetite, Cr-rich magnetite and hematite was observed. The main wear mechanism was delamination of this oxide film.
- A GO-rich protective film was formed on the worn surface when using 0.1 % GO and 0.3 % ZnO@GO solutions as lubricants. The formation of the GO protective throughout the whole surface was observed in the case of the 0.3 % ZnO@GO solution, whereas the film did not cover the entire surface in the case of the 0.1% GO solution.
- A reduction of the I_D/I_G ratio in the Raman spectra recorded at the worn surfaces was observed after the wear tests using 0.1 % GO and 0.3 % ZnO@GO lubricants, suggesting the occurrence of a partial chemical reduction of graphene oxide as a consequence of the high local temperature produced during the wear tests.

References

[1] Qiang, R., Hu, L., Hou, K., Wang, J., & Yang, S. (2019). Water-soluble graphene quantum dots as high-performance water-based lubricant additive for steel/steel contact. Tribology Letters, 67(2), 1-9.

[2] Huang, S., He, A., Yun, J. H., Xu, X., Jiang, Z., Jiao, S., & Huang, H. (2019). Synergistic tribological performance of a water-based lubricant using

graphene oxide and alumina hybrid nanoparticles as additives. Tribology International, 135, 170-180.

[3] Chen, C. Y., Wu, B. H., Chung, C. J., Li, W. L., Chien, C. W., Wu, P. H., & Cheng, C. W. (2013). Low-friction characteristics of nanostructured surfaces on silicon carbide for water-lubricated seals. Tribology Letters, 51(1), 127-133.

[4] Gan, C., Liang, T., Li, X., Li, W., Li, H., Fan, X., & Zhu, M. (2021). Ultra-dispersive monolayer graphene oxide as water-based lubricant additive: Preparation, characterization and lubricating mechanisms. Tribology International, 155, 106768.

[5] Ma, H., Li, J., Chen, H., Zuo, G., Yu, Y., Ren, T., & Zhao, Y. (2009). XPS and XANES characteristics of tribofilms and thermal films generated by two P- and/or S-containing additives in water-based lubricant. Tribology international, 42(6), 940-945.

[6] Tomala, A., Karpinska, A., Werner, W. S. M., Olver, A., & Störi, H. (2010). Tribological properties of additives for water-based lubricants. Wear, 269(11-12), 804-810.

[7] Kinoshita, H., Nishina, Y., Alias, A. A., & Fujii, M. (2014). Tribological properties of monolayer graphene oxide sheets as water-based lubricant additives. Carbon, 66, 720-723.

[8] Padgurskas, J., Rukuiza, R., Prosyčevas, I., & Kreivaitis, R. (2013). Tribological properties of lubricant additives of Fe, Cu and Co nanoparticles. Tribology International, 60, 224-232.

[9] Wu, H., Zhao, J., Cheng, X., Xia, W., He, A., Yun, J. H., ... & Jiang, Z. (2018). Friction and wear characteristics of TiO2 nano-additive water-based lubricant on ferritic stainless steel. Tribology International, 117, 24-38.

[10] Cao, Z., Xia, Y., & Chen, C. (2018). Fabrication of novel ionic liquids-doped polyaniline as lubricant additive for anti-corrosion and tribological properties. Tribology International, 120, 446-454.

[11] Song, H., Huang, J., Jia, X., & Sheng, W. (2018). Facile synthesis of core–shell Ag@ C nanospheres with improved tribological properties for water-based additives. New Journal of Chemistry, 42(11), 8773-8782.

[12] Liu, C., Guo, Y., & Wang, D. (2019). PEI-RGO nanosheets as a nanoadditive for enhancing the tribological properties of water-based lubricants. Tribology International, 140, 105851.

[13] Haghshenas, S. S. P., Nemati, A., Simchi, R., & Kim, C. U. (2019). Photocatalytic and photoluminescence properties of ZnO/graphene quasi core-shell nanoparticles. Ceramics International, 45(7), 8945-8961.

[14] Dreyer, D. R., Park, S., Bielawski, C. W., & Ruoff, R. S. (2010). The chemistry of graphene oxide. Chemical society reviews, 39(1), 228-240.

[15] Berman, D., Erdemir, A., & Sumant, A. V. (2013). Few layer graphene to reduce wear and friction on sliding steel surfaces. Carbon, 54, 454-459.

[16] Liang, S., Shen, Z., Yi, M., Liu, L., Zhang, X., & Ma, S. (2016). In-situ exfoliated graphene for high-performance water-based lubricants. Carbon, 96, 1181-1190.

[17] Xie, H., Jiang, B., Dai, J., Peng, C., Li, C., Li, Q., & Pan, F. (2018). Tribological behaviors of graphene and graphene oxide as water-based lubricant additives for magnesium alloy/steel contacts. Materials, 11(2), 206.

[18] Ren, B., Gao, L., Li, M., Zhang, S., & Ran, X. (2020). Tribological properties and anti-wear mechanism of ZnO@ graphene core-shell nanoparticles as lubricant additives. Tribology International, 144, 106114.

[19] Xie, H., Dang, S., Jiang, B., Xiang, L., Zhou, S., Sheng, H., ... & Pan, F. (2019). Tribological performances of SiO2/graphene combinations as water-based lubricant additives for magnesium alloy rolling. Applied Surface Science, 475, 847-856.

[20] Huang, S., Lin, W., Li, X., Fan, Z., Wu, H., Jiang, Z., & Huang, H. (2021). Roughness-dependent tribological characteristics of water-based GO suspensions with ZrO2 and TiO2 nanoparticles as additives. Tribology International, 161, 107073.

[21] Yang, Y., Ma, L., Wang, H., Jia, W., Zhu, J., Wang, J., & Yang, S. (2022). A novel water-based lubricating additive of GO@ PTFE: Superior tribological performances from the synergistic effect. Tribology International, 169, 107485.

[22] Baghdadi, Y. N., Youssef, L., Bouhadir, K., Harb, M., Mustapha, S., Patra, D., & Tehrani-Bagha, A. R. (2020). The effects of modified zinc oxide nanoparticles on the mechanical/thermal properties of epoxy resin. Journal of Applied Polymer Science, 137(43), 49330.

[23] Hummers Jr, W. S., & Offeman, R. E. (1958). Preparation of graphitic oxide. Journal of the american chemical society, 80(6), 1339-1339.

[24] Ribeiro, J. S., Freitas, M. B., & Freitas, J. C. (2021). Recycling of graphite and metals from spent Li-ion batteries aiming the production of graphene/CoO-based electrochemical sensors. Journal of Environmental Chemical Engineering, 9(1), 104689.

[25] Hong, J., Liu, C., Deng, X., Jiang, T., Gan, L., & Huang, J. (2016). Enhanced tribological properties in core–shell structured SiO 2@ GO hybrid fillers for epoxy nanocomposites. RSC advances, 6(92), 89221-89230. DOI 10.1039/C6RA18207K

[26] Hamrock, B. J., & Dowson, D. (1977). Isothermal elastohydrodynamic lubrication of point contacts: part III—fully flooded results. https://doi.org/10.1115/1.3453074.

[27] Díez-Betriu, X., Álvarez-García, S., Botas, C., Álvarez, P., Sánchez-Marcos, J., Prieto, C., ... & De Andrés, A. (2013). Raman spectroscopy for the study of reduction mechanisms and optimization of conductivity in graphene oxide thin films. Journal of Materials Chemistry C, 1(41), 6905-6912. https://doi.org/10.1039/C3TC31124D

[28] Ferrari, A. C. (2007). Raman spectroscopy of graphene and graphite: Disorder, electron–phonon coupling, doping and nonadiabatic effects. Solid state communications, 143(1-2), 47-57. https://doi.org/10.1016/j.ssc.2007.03.052

[29] Scardaci, V., & Compagnini, G. (2021). Raman spectroscopy investigation of graphene oxide reduction by laser scribing. C, 7(2), 48. https://doi.org/10.3390/c7020048

[30] Shankar, P., Ishak, M. H., Padarti, J. K., Mintcheva, N., Iwamori, S., Gurbatov, S. O., ... & Kulinich, S. A. (2020). ZnO@ graphene oxide core@ shell

nanoparticles prepared via one-pot approach based on laser ablation in water. Applied Surface Science, 531, 147365.

[31] Mokhtar, M., El Enein, S. A., Hassaan, M., Morsy, M., & Khalil, M. (2017). Thermally reduced graphene oxide: synthesis, structural and electrical properties. Int J Nanoparticles Nanotechnol, 3(1), 1-9.

[32] Wang, C., Chen, Z., He, Y., Li, L., & Zhang, D. (2010). Raman scattering of ZnO films prepared by the laser molecular beam epitaxy. Materials Science-Poland, 28(1), 153.

[33] Cui, Y., Ding, M., Sui, T., Zheng, W., Qiao, G., Yan, S., & Liu, X. (2020). Role of nanoparticle materials as water-based lubricant additives for ceramics. Tribology International, 142, 105978.

[34] Othman, N. H., Yahya, W. Z. N., Che Ismail, M., & Mustapha, M. (2020). Highly dispersed graphene oxide–zinc oxide nanohybrids in epoxy coating with improved water barrier properties and corrosion resistance. Journal of Coatings Technology and Research, 17(1), 101-114.

[35] Ossonon, B. D., & Bélanger, D. (2017). Synthesis and characterization of sulfophenyl-functionalized reduced graphene oxide sheets. RSC advances, 7(44), 27224-27234.

[36] He, H., Riedl, T., Lerf, A., & Klinowski, J. (1996). Solid-state NMR studies of the structure of graphite oxide. The Journal of physical chemistry, 100(51), 19954-19958. https://doi.org/10.1021/jp961563t

[37] Cai, W., Piner, R. D., Stadermann, F. J., Park, S., Shaibat, M. A., Ishii, Y., ... & Ruoff, R. S. (2008). Synthesis and solid-state NMR structural characterization of 13C-labeled graphite oxide. Science, 321(5897), 1815-1817. https://doi.org/10.1126/science.1162369

[38] Vieira, M. A., Gonçalves, G. R., Cipriano, D. F., Schettino Jr, M. A., Silva Filho, E. A., Cunha, A. G., ... & Freitas, J. C. (2016). Synthesis of graphite oxide from milled graphite studied by solid-state 13C nuclear magnetic resonance. Carbon, 98, 496-503. http://dx.doi.org/10.1016/j.carbon.2015.11.037

[39] MacIntosh, A. R., Harris, K. J., & Goward, G. R. (2016). Structure and dynamics in functionalized graphene oxides through solid-state NMR. Chemistry of Materials, 28(1), 360-367. https://doi.org/10.1021/acs.chemmater.5b04287

[40] Caliman, C. C., Mesquita, A. F., Cipriano, D. F., Freitas, J. C. C., Cotta, A. A. C., Macedo, W. A. A., & Porto, A. O. (2018). One-pot synthesis of amine-functionalized graphene oxide by microwave-assisted reactions: an outstanding alternative for supporting materials in supercapacitors. RSC advances, 8(11), 6136-6145. https://doi.org/10.1039/c7ra13514a

[41] Guo, P., Chen, L., Wang, J., Geng, Z., Lu, Z., & Zhang, G. (2018). Enhanced tribological performance of aminated nano-silica modified graphene oxide as water-based lubricant additive. ACS Applied Nano Materials, 1(11), 6444-6453.

[42] Sutton, D. C., Limbert, G., Burdett, B., & Wood, R. J. K. (2013). Interpreting the effects of interfacial chemistry on the tribology of diamond-like carbon coatings against steel in distilled water. Wear, 302(1-2), 918-928. https://doi.org/10.1016/j.wear.2013.01.089

[43] Kuang, W., Wu, X., & Han, E. H. (2010). The oxidation behaviour of 304 stainless steel in oxygenated high temperature water. Corrosion Science, 52(12), 4081-4087.

[44] Muzyka, R., Drewniak, S., Pustelny, T., Chrubasik, M., & Gryglewicz, G. (2018). Characterization of graphite oxide and reduced graphene oxide obtained from different graphite precursors and oxidized by different methods using Raman spectroscopy. Materials, 11(7), 1050.

Chapter 03

3. Influence of Polyethylene Glycol addition on the deposition and tribological performance of cobalt coatings prepared via cathode plasma electrolytic deposition.

3.1. Abstract

A nanocrystalline cobalt coating was prepared by cathode plasma electrolytic deposition (CPED) using different amounts of polyethylene glycol (PEG) (0%, 3%, 6% and 10%). Deposition mechanisms were discussed. PEG addition effect on the characteristic voltage-current curve, bubbles evolution, surface morphology and tribological performance was determined. Instant current peaks and bubble implosion have a close relationship and directly influence coating thickness. Obtained coatings were characterized by FESEM, EDS, XRD and tribologically, by linear scratch test and sliding wear test. The coatings have a face center cubic (FCC) metastable structure, higher hardness (around 550 HV), better wear resistance, lower friction coefficient than the substrate and high adhesion force (around 77 N). PEG addition decreased layer thickness, changed surface morphology but did not affect hardness, friction coefficient and wear.

3.2. Introduction

3.2.1. Electrolytic Plasma Deposition

Plasma electrolysis is a hybrid process that combines conventional electrolysis and atmospheric plasma processing. It is an emerging technology, firstly demonstrated in 1960’s, with potential use in commercial scale for cleaning and coating due to its low cost, high adhesion to substrate, high deposition rates and environmental compatibility [1]. Electrolytic plasma deposition (EPD) can be divided into two categories, according to substrate polarity: anodic, such as Plasma Electrolytic Oxidation (PEO), or cathodic, often referred to Plasma Electrolytic Saturation (PES) or Cathodic Plasma Electrolysis (CPE), for which fewer studies exist [1-3].

The process consists of applying an electrical potential, greater than in conventional electrolysis, between the workpiece and the counter-electrode immersed in an electrolyte, leading to an anomalous gas evolution that enables plasma discharge [1, 3].

At low voltages, the process obeys Faraday's law and current varies linearly with voltage according to Ohm's law. In the vicinity of cathode's surface, hydrogen ($2H^{+} + 2e^{-} \rightarrow H_2 \uparrow$) and cation reduction ($Cat^{n+} + ne^{-} \rightarrow Cat^{0} \downarrow$) take place, resulting in a partial gas shielding (H_2) of the workpiece surface. Due to gas low electrical conductivity, current rise is limited. However, current still rise in areas where the electrolyte remains in contact with the workpiece, causing local boiling near the electrode as a result of Joule's effect. Therefore, increasing the voltage, a continuous gas sheath (cluster of bubbles) is formed. Liquid phase conductivity is considerably higher than the gas and due to the high applied voltage, a high concentration of cations migrates toward the surface of the gas bubbles, thus, the gas-electrolyte interface now acts like the anode. Hence, the effective distance between the anode and the cathode is similar to bubbles diameter, resulting in high localized electrical field, reaching the breakdown voltage, initiating ionization of the gas. Together with gas ionization, current density sharply decreases due to the resistance increase of the vapor phase. During the treatment, a typical range is around 0.5 to 1 A/cm². Initially, sparking occurs rapidly in the smallest scattered bubbles, but, with further voltage increase, continuous luminous discharge throughout the envelope takes place. At higher voltages, deleterious high-energy arcing regime occurs and current density increases again [1-4].

Gupta et al. [1] described the key mechanisms by which deposition occurs. As stated previously, a cluster of bubbles shields samples surface. Locally, plasma temperature can reach over 2000 °C. However, it is surrounded by a cooler electrolyte, bubbles expand, become unstable and soon, implode on the metal surface. Plasma deposition has been reported as a consequence of bubbles expansion and implosion as discrete plasma discharges over the surface (Gupta et al., 2007). Besides, the high temperature of the plasma can locally melt the surface, but right after the collapse of bubbles, the surface is quenched by the cooler surrounding electrolyte at cooling rates reaching 10^{8} K/s, resulting in unique microstructures, such as supersaturated solid solutions and non-equilibrium compounds [1-3, 5].

The cathodic branch of EPD is used for preparing diverse metal coatings, such as Co, Ni, Cr, Mo, Al and Zn. [1, 6-9]. Gupta et al. [9] using CPED obtained Mo coating with excellent adhesion along with high deposition rates. Alloying Mo into 718 Inconel and 4340V steel substrates were attributed to the high diffusion rates that are present in CPED due to local melting and the high applied electrical potential. This diffusion layer was also observed by Aliofkhazrei and Roohaghdam [6] when depositing Al onto Ti substrates.

Quan and He [7, 10] were able to produce pure Co coating using CPED process without using any additives in the electrolyte. Differently from what is observed in conventional electrolysis, the coating had a metastable FCC cobalt phase. Co films exhibited excellent adhesion (108.5 N) and high hardness (superior to 700 HV). Cobalt is known as a wear and corrosion resistant material. It has high hardness, biocompatibility and unique magnetic properties that allows its use in microelectronics, sensor technology and in critical applications in industry and in defense [11-13].

The influence of polyethylene glycol (PEG) on CPED has been investigated. Wang et al. [14] and Liu et al. [15] found that this additive not only reduced current density during deposition, but also decreased porosity of Al_2O_3 coatings. PEG increases electrolyte viscosity, hindering bubbles migration from the cathode surface to the electrolyte, easing plasma formation and discharge. Zhang et al. [16] showed that PEG addition reduced crystalline size of Ni/graphene oxide coatings. According to the authors, considering that PEG works as a non-ionic surfactant, it led to a better nanoparticle dispersion.

In this study, the influence of PEG addition on deposition mechanism of Cobalt coating through CPED was investigated. Different amount of PEG (0%, 3%, 6% and 10%) were used and its effect on microstructure, topography and coating thickness was evaluated. Besides, sliding wear tests on the ball-on-plate configuration were done to assess tribological behavior. A correlation between instant current peak density, bubbles implosion and coating thickness was proposed.

3.3. Materials and Methods

3.3.1. Cathode plasma electrolytic deposition process

A CPED device was developed for preparing the coating. The device schematic diagram is shown in Figure 3-1. Basically, it is composed by the following parts: electrolyte cell, colling system, thermocouple, DC power supply, current and voltage monitoring system, illumination system and, recording cameras.

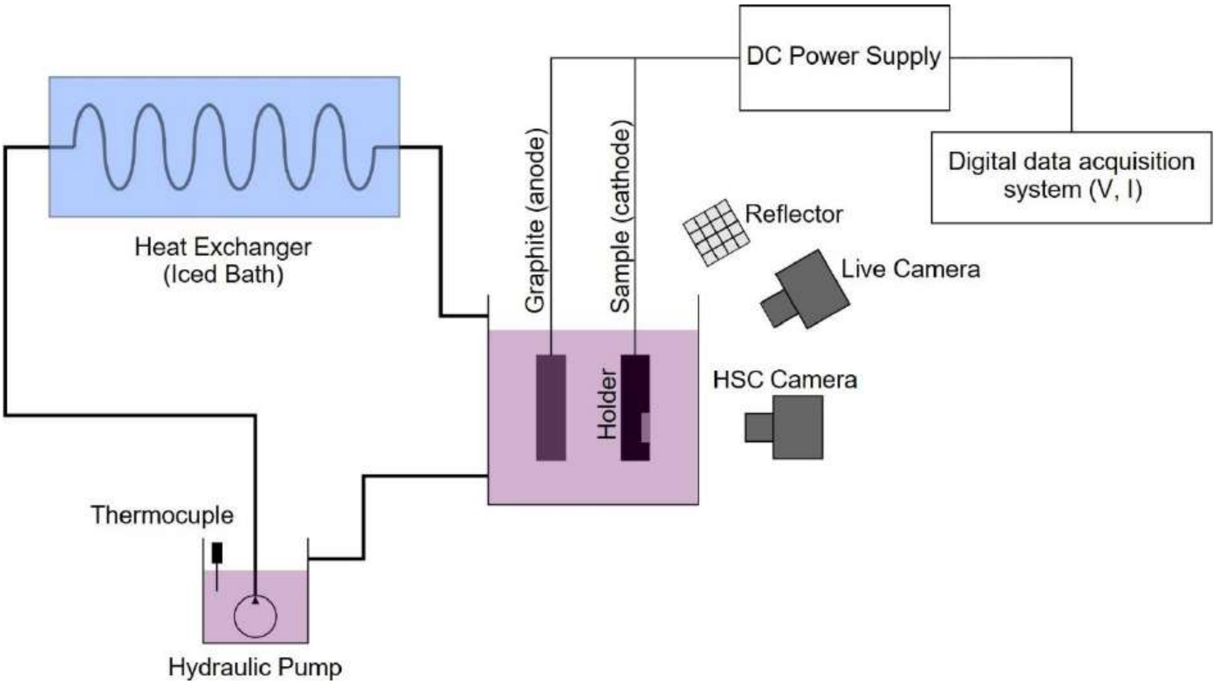

Figure 3-1 - CPED device.

A variac controlled DC power supply was used and its electrical scheme is shown in Figure 3-2. The power supply inductance and capacitance configuration were chosen by means of exploratory tests. Inductor and capacitor were used to a better current rectifying behavior and to filter current peaks. Voltage versus current density curves were obtained for four different configurations (described in Table 3-1), to determine for which stable plasma arcs took place at lower voltage and current levels.

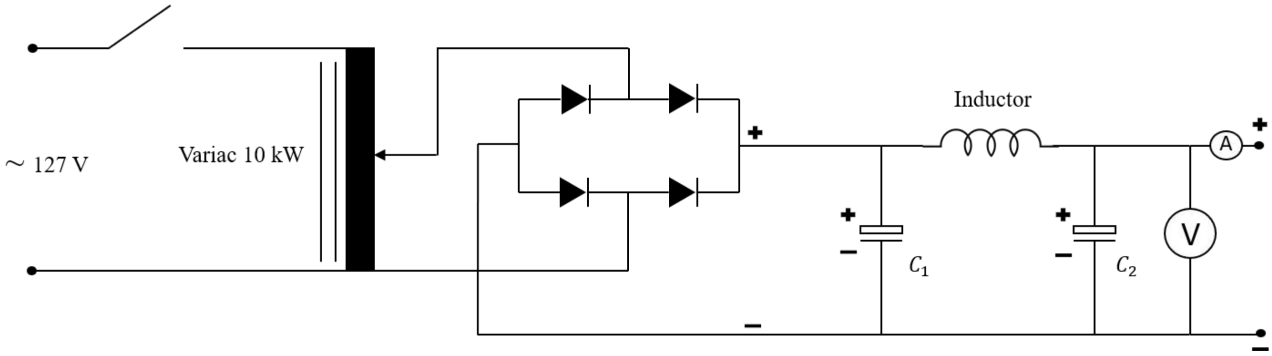

Figure 3-2 - Power supply electronic scheme.

Table 3-1 - Power supply configuration.

Code	Capacitance	
	$C_1\ [\mu F]$	$C_2 [\mu F]$
A	20	0
B	20	220
C	200	0
D	220	0

A data acquisition system connected to a computer was used to monitor instantaneous current and voltage during the process. Acquisition frequency is 5 kHz.

A rectangular-shaped acrylic recipient is used in the electrolyte cell to facilitate camera imaging of the sample. Electrolyte is recirculated through the cell, using a 200 l/h flow rate pump. The electrolyte leaves the cell and passes through a cooling system consisting of a serpentine silicone tube that is immersed in an iced bath. Electrolyte temperature is monitored during the test by a thermocouple placed inside the cell. Recirculating is not only important to cool the electrolyte but also to homogenize it. A graphite (99.9% purity) plate is used as the anode while the AISI 304 austenitic stainless-steel sample is used as the cathode. Both, anode and cathode are connected to the power supply by a metallic joint, and were placed inside an ABS polymer holder to avoid contamination of the electrolyte with other metals and to bound the deposition area.

Graphite plate has an area of 40 cm^2 and sample deposition area is 1 cm^2. The distance between the anode and the cathode was approximately 30 mm. AISI 304 samples were obtained from a flat bar, were cut (12 x 30 x 2 mm) and grounded to a 1200 grit, cleaned in acetone ultrasonically for 15 min and dried.

Cobalt (II) sulfate heptahydrate ($CoSO_4.7H_2O$) as main reactant and polyethylene glycol (PEG) were purchased from Neon reagents, Brazil. Distilled (DI) water was used as solvent in all experiments. $CoSO_4.7H_2O$ (25 g/l), H_2SO_4 (60 g/l), different contents of PEG (0, 0.75, 1.5 and 2.5 g/l) and DI water were mixed forming the electrolyte. The concentration of $CoSO_4.7H_2O$ and H_2SO_4 were chosen from the available literature [7].

During exploratory tests, deposition was carried out while the bath was stirred using a magnetic device. However, it hindered plasma formation. Thus, for tests, before the deposition, the electrolyte was magnetic stirred for 20 min. 350 ml of electrolyte was used in each test.

In order to determine the characteristic voltage versus current density for each studied condition, the voltage was increased with the rate of 0.5 V/s, from 0 to 100 V. From these curves, the deposition voltage was determined, i.e., the voltage where plasma occurs and current density reaches a minimum plateau. For CPED process itself, the voltage was directly increased to 85 V and held for 3 min. Sample codes are described in Table 3-2.

Table 3-2 - Sample codes and CPED parameters

Sample code	**Electrolyte** $\mathbf{25\ g/l\ CoSO_4 + 60\ g/lH_2SO_4}$
0%PEG	0 g/l PEG
3%PEG	0.75 g/l PEG
6%PEG	1.5 g/l PEG
10%PEG	2.5 g/l PEG

Sample surface during the CPED process was monitored using a live camera and a high-speed camera (HSC/Fastec IL-5) with 2000 fps frame rate to investigate the bubble morphology and kinetics during the deposition. An illumination system using two LED reflectors were used to improve image quality.

3.3.2. Characterization:

Field emission scanning electron microscope (FESEM, FEI-Inspect F50) was used to investigate the morphology of both, surface and cross-section. In order to better estimate coatings thickness, the cross-sections of samples were chemically etched with Nital 5% prior to FESEM imaging. Energy dispersive spectroscopy (EDS) was carried out to analyze the composition of the coatings. The topography of the coatings was assessed by an 3D optical profilometer (S Neox, Sensofar).

The X-ray diffraction (XRD, Rigaku) measurements were performed with a molybdenum radiation ($\lambda = 7{,}0926\ nm$) for identifying phases present. Besides, grain size was estimated using Scherrer's equation:

$$d = \frac{0.9\lambda}{Bcos\Theta} \qquad \text{Eq. (1)}$$

Where Ɵ is Bragg diffraction angle and B is the full width at half maximum (FWHM) of the peak (in radians).

Vickers microhardness tests using 25 gf load were carried out. At least ten indentations were done in each sample surface.

Wetting angle measurements were carried out using water and synthetic polyalphaolefin (PAO) oil. A droplet (20 µL) was dispensed onto the sample surface, then the camera captures the droplet image. The wetting angle was measured using ImageJ software. Ten replicates were done for each condition.

In order to evaluate de adhesion of the coating with the substrate, scratch tests were done using a Universal Macro-Tribometer Apex CETR-Bruker, in the linear scratch configuration. A Rockwell-C diamond cone indenter with an apex angle of 120° and 200 µm tip radius slides against the surface under a linearly increasing load from 20 N to 120 N at a rate of 10 N/mm. Scratches length were 9 mm and test speed of 2 mm/min. The surface topography and failure modes were investigated using 3D optical profilometry and stereoscopic microscope. The critical load for adhesive-related failure mode was identified based on imaging and variation of the tangential force. Thus, the adhesion force between coating and the substrate is estimated [17]. Three replicates were done for each studied condition.

3.3.3. Tribological tests

Ball-on-plate sliding tests were done on a PLINT TE67 tribometer (Phoenix Tribology Ltd) using the deposited sample as the plate (body) and a 11 mm AISI 52100 ball as the counter-body. Test parameters used are shown in Table 3-3. Friction force is monitored by a load cell with an acquisition frequency of 10 Hz. The initial Hertz contact pressure is approximately 0.7 GPa. Tests were performed in random order. Previously to the tests, samples and ball were cleaned in acetone ultrasonically for 15 min. 3 replicates were done for each coating.

Table 3-3 - Sliding test parameters.

Stroke length	2.5 mm
Sliding frequency	3 Hz
Normal load	500 N
Test duration	30 min

Samples wear losses were determined using a Sartorius analytical balance with 0.1 mg precision.

3.4. Results and discussion:

Figure 3-3 shows the evolution of the current-voltage curve for each power supply configuration. Despite the differences in capacitance and inductance, for low voltages, all curves respected Ohm’s law, where a linear relationship between current and voltage is observed. However, the curves differ in peak current, critical voltage for plasma ignition and the Ohm’s resultant resistance in region 01. CPED process can be classically divided in four regions. Region 01, where Ohm’s law is obeyed. As mentioned earlier, H_2 gas evolution on cathode’s surface, and with voltage increase, gas bubbles completely cover the surface. Due to the gas low electrical conductivity, above peak current, it is observed a current density decrease (Region 02), where few discrete luminous plasma discharges are observed. With further voltage increase, the whole surface of the cathode is taken by luminous discharge (Region 03). For higher voltages, region 04, arcing regime begins, where bright arcs are seen accompanied by loud noise. Typically, in the arcing regime there is once again a current increase with the voltage.

Condition A, C and D differs only in capacitance value. The characteristic curves were similar to that reported by Quan and He (2015). Plasma discharge were clearly observed for voltages superior to 75 V and current reached a minimum plateau around 85 V. For higher voltages, arcing regime was observed. Nevertheless, peak current is lower for condition A. Noticeably, the process resistance in region 01 is dependent on power supply capacitance, but this effect apparently is less important once the plasma discharge occurs. In condition B, an extra capacitor was added ahead of the inductor. This electrical configuration displayed the same peak current as condition D, but current stabilization was not observed even for the highest voltage level (100 V). Plasma discharge was observed but it did not cover the sample surface entirely.

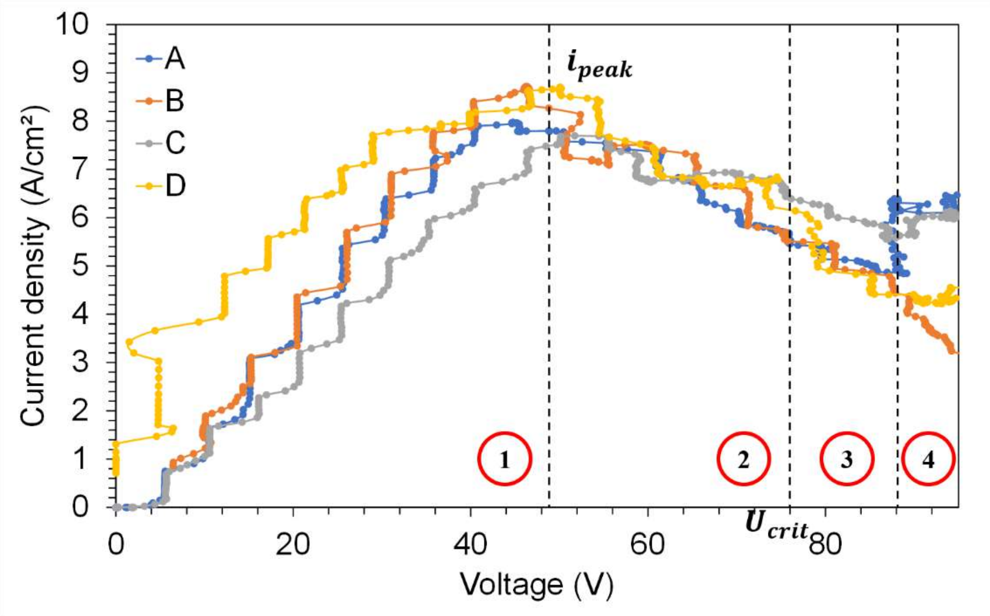

Figure 3-3 – Current density versus voltage for different power supply configurations.

Owing to the smaller peak current, when compared to condition D and the smaller plasma current in region 03, when compared to condition C, electrical configuration A of the DC power supply was selected to carry out the depositions.

Figure 3-4 shows the current-voltage characteristic curves of the different studied electrolytes. The characteristic curves were similar to that reported by Quan and He [7]. CPED process can be classically divided in four regions, Region 01, where Ohm's law is obeyed. As mentioned earlier, H_2 gas evolution on cathode's surface, and with voltage increase, gas bubbles completely cover the surface. Due to the gas low electrical conductivity, above peak current, it is observed a current density decrease (Region 02), where few discrete luminous plasma discharges are observed. With further voltage increase, the whole surface of the cathode is taken by luminous discharge (Region 03). For higher voltages, region 04, arcing regime begins, where bright arcs are seen accompanied by loud noise [1, 2, 4]. Plasma discharges were clearly observed for voltages superior to 75 V and current reached a minimum plateau around 85 V. For higher voltages, arcing regime was observed.

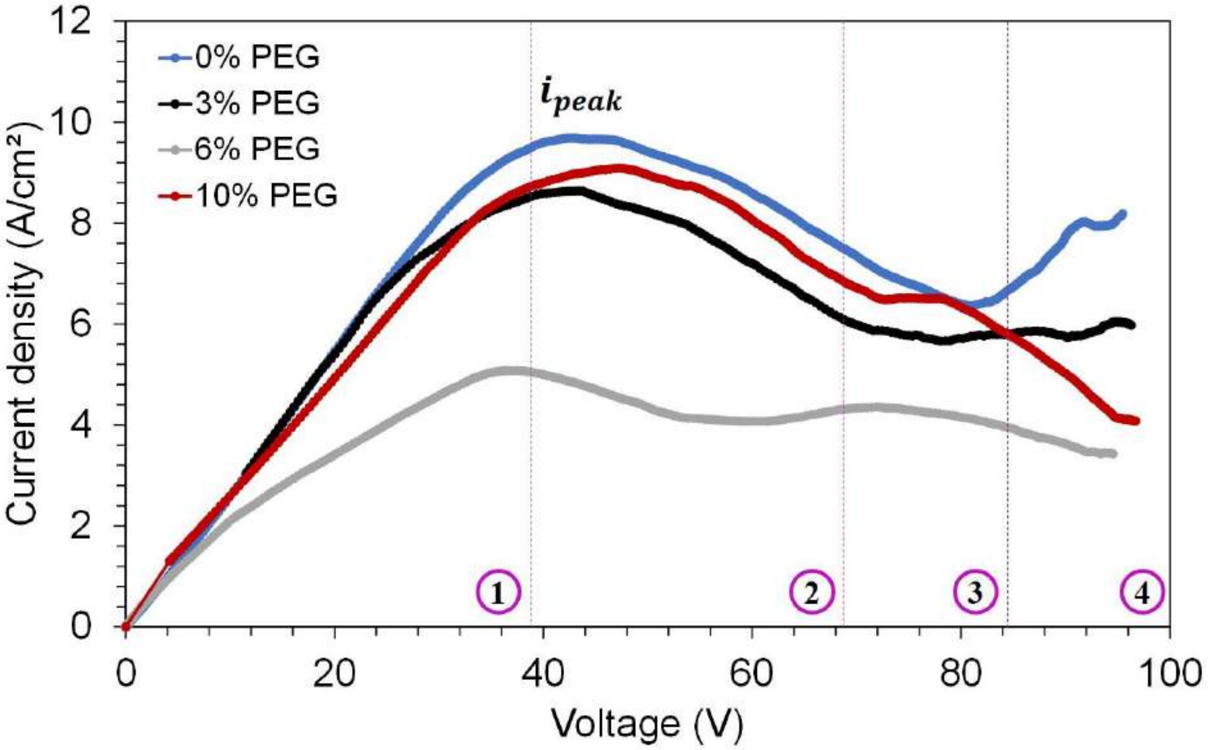

Figure 3-4 - Current density - Voltage characteristic curves for 0%, 3%, 6% and 10% PEG samples – Regions 1, 2, 3 and 4 are indicated.

It can be observed that PEG addition reduced the current density overall and delayed the occurrence of arcing regime (current rise in higher voltages). This effect has been pointed out by several authors [14, 15]. PEG increases the viscosity of the electrolyte, hindering the migration of the bubbles formed on the cathode surface towards the electrolyte. Besides, PEG is known to increase adsorption of gas on cathode surface [15]. Thus, vapor sheath needed to form plasma discharge is more easily formed due to bubbles entrapment to the surface, decreasing i_{peak}. It can be seen that 6% PEG condition has a more pronounced effect on current decrease. However, for 10% PEG condition, current stabilization associated with continuous plasma envelope throughout the surface only occurred for higher voltages (around 95 V).

Deposition was carried out for the different electrolytes at 85 V. The curves of current density-time for each condition (0, 3, 6 and 10% PEG) can be seen in Figure 3-5. Current density slightly decreases and stabilized during the deposition process. 3% PEG sample exhibited a most stable current even at the begging of deposition. Despite exhibiting the lower current at the end of the deposition, 6% PEG sample took longer to achieve a stabilization of current and of the plasma discharge process. It should be underlined that a low current density enables deposition in larger pieces, amplifying commercial potential of CPED.

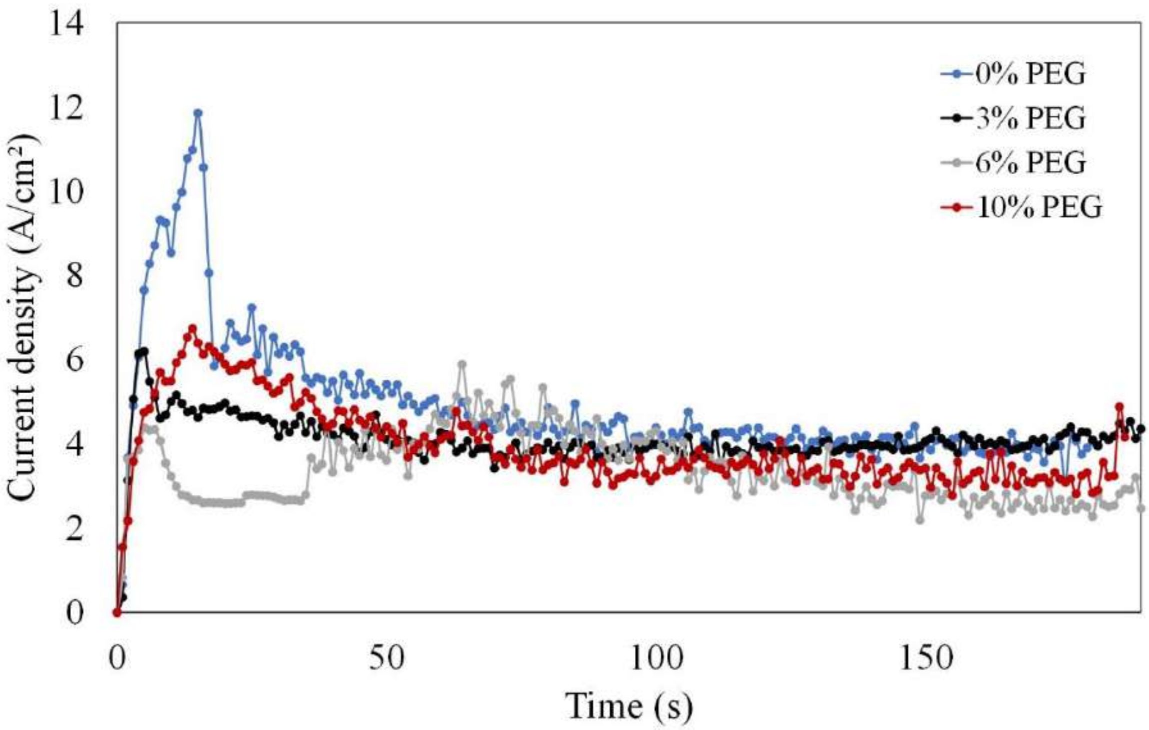

Figure 3-5 - Current density with time curves for different electrolytes: 0%, 3%, 6% and 10% PEG.

By examining the instantaneous current density during one second of deposition (Figure 3-6), it is observable that, in fact, the current has a pulsed behavior, and the frequency of these pulses is directly affected by PEG addition, although PEG did not alter pulses magnitude, which regardless of the electrolyte, it is around 15 A/cm². Using the electrolyte with no additives (0% PEG), the density of pulses in one second is higher. Apparently, PEG effect on current stems from a competitive mechanism, at 3% and 10% PEG, pulse frequency is lower than at intermediate level (6% PEG).

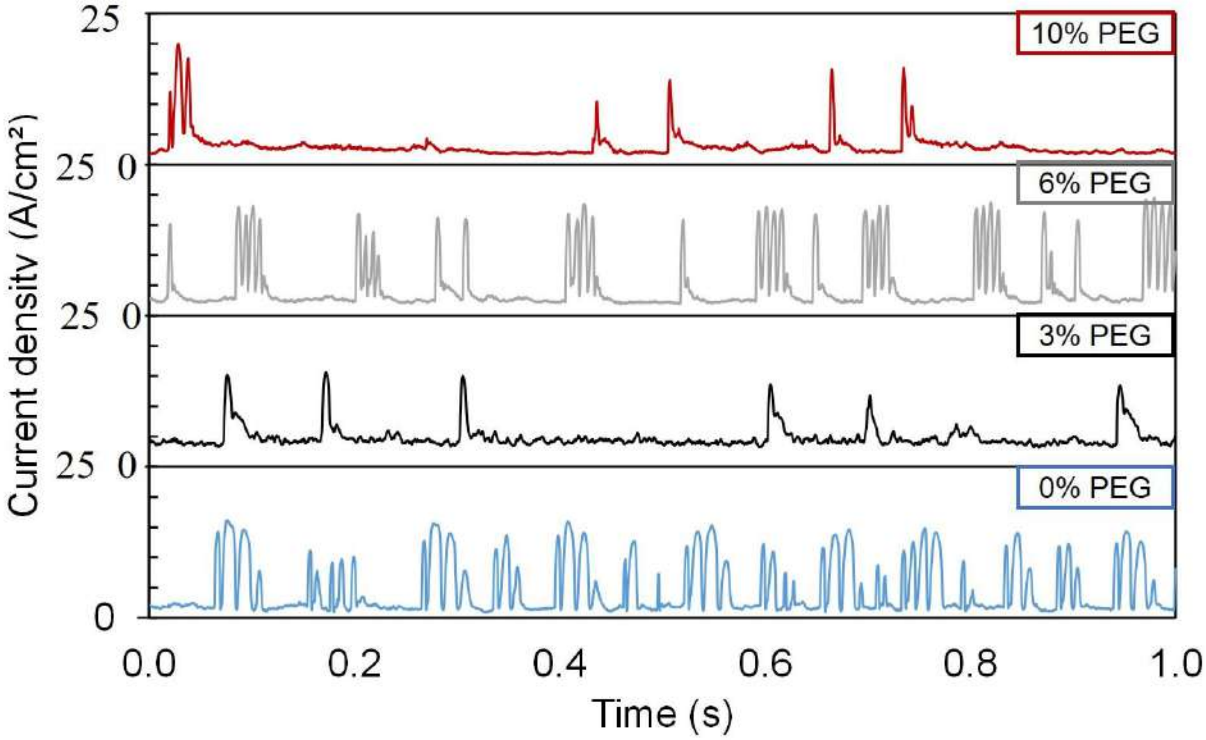

Figure 3-6 - Instantaneous current with time (1 second of data acquisition) for each studied electrolyte: 0%, 3%, 6% and 10%PEG.

Images taken by the HSC camera during deposition process help to better understand bubbles formation and coalescence. Figure 3-7 shows bubble implosion phenomenon in the different electrolytes. Initially, sample surface is covered by small bubbles where plasma discharging is occurring. With time, coalescence of small bubbles growing in adjacent nucleation sites takes place, forming a long vapor column on the sample surface which grows due the different internal and external pressures resulting from the gas and liquid interface, causing an overpressure within the bubble [3]. Eventually, this vapor column becomes unstable and implodes, releasing electrolytes microjets towards the surface and vapor moves upwards. It can be observed that quantity of bubbles increased with PEG addition. The surface of the sample cannot be seen when using 10% PEG electrolyte, as it is completely covered by bubbles, even right after the collapse. Besides, looking at the 5th figure of each sequence, it is possible to see that vapor column expansion is higher for 0% PEG than for the conditions with PEG, which probably resulted in a more severe implosion.

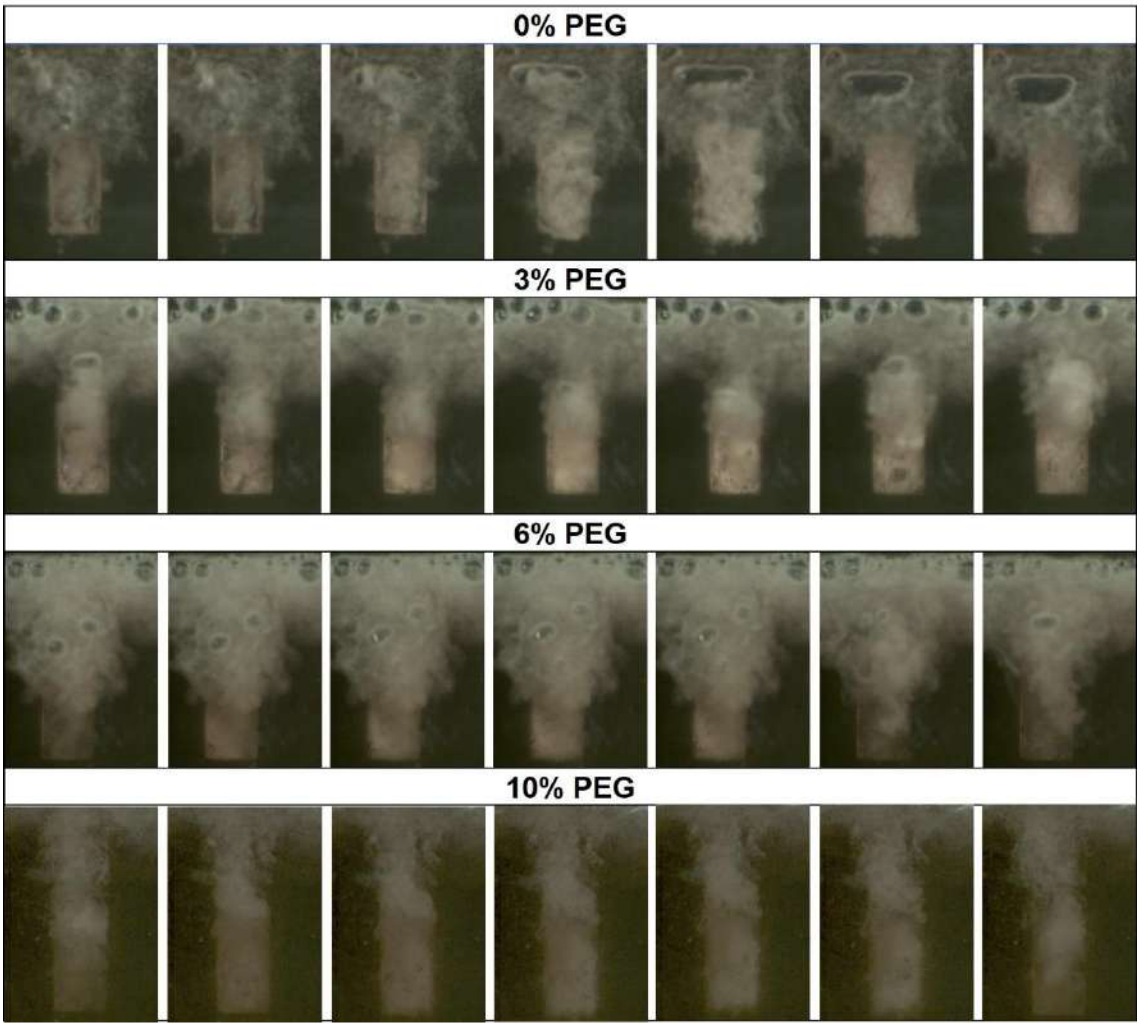

Figure 3-7 - HSC imaging showing bubble implosion mechanism for 0%, 3% and 6% PEG addition.

The bubbles collapsing process takes less than 20 ms and it occurs periodically, but its frequency depended on the used electrolyte, just as observed for the instantaneous current peaks. Table 3-4 shows the number of implosions observed in 1 second HSC recording and the number of current peaks presented in Figure 3-6. A relationship can be drawn between implosions and current peaks. A reasonable hypothesis is that when bubbles are small, plasma discharge is occurring on samples surface. As pointed out earlier, the evolving gas sheath has low electrical conductivity, leading to a low current density for a constant voltage. As bubbles coalesce and grow, they become unstable and implode, then a microjet is formed and hits the surface. At this moment, the electrolyte is in momentaneous contact with the sample not the vapor sheath. The electrolyte has a high electrical conductivity, increasing the current. However, rapidly bubbles are formed again due to the electrolysis process itself, leading to current drop. Therefore, bubbles implosion probably accounts for the current peaks observed.

Table 3-4 - Number of bubble implosion by analysis of HSC images and current peaks recorded in 1 second for each studied electrolyte (0%, 3%, 6% and 10% PEG).

Sample	**Implosions [1/s]**	**Current peaks [1/s]**
0% PEG	44	51
3% PEG	4	6
6% PEG	34	35
10% PEG	13	8

Figure 3-8 shows the surface morphologies and cross-section of the obtained coatings. PEG strongly affected both the surface morphology and coatings thickness. Figure 3-8 A and B shows the surface of the coating prepared in 0% PEG electrolyte. A spheroidal nodules morphology is observed, differently from the molten morphology shown by Quan and He [7] when depositing cobalt coatings by CPED. Gupta et al. [1] and Parfenov et al. [4] attributed the presence of microcraters and spheroidal nodules on CPED deposits to plasma bubbles implosion and quenching of localized melted surface. However, in Figure 3-8 (A and B) microcraters are not seen and porosity levels are low. Plasma temperature can reach over 2000°C [1] while the surrounding electrolyte temperature remained inferior to 60 °C, quenching and freezing the microstructures. Figure 3-8.C shows the cross-section of the same sample. A continuous and compact layer is formed, but microcracks are visible. Besides, coating-substrate interface is not completely visible, indicating that a good mechanical interlocking with the coating was obtained.

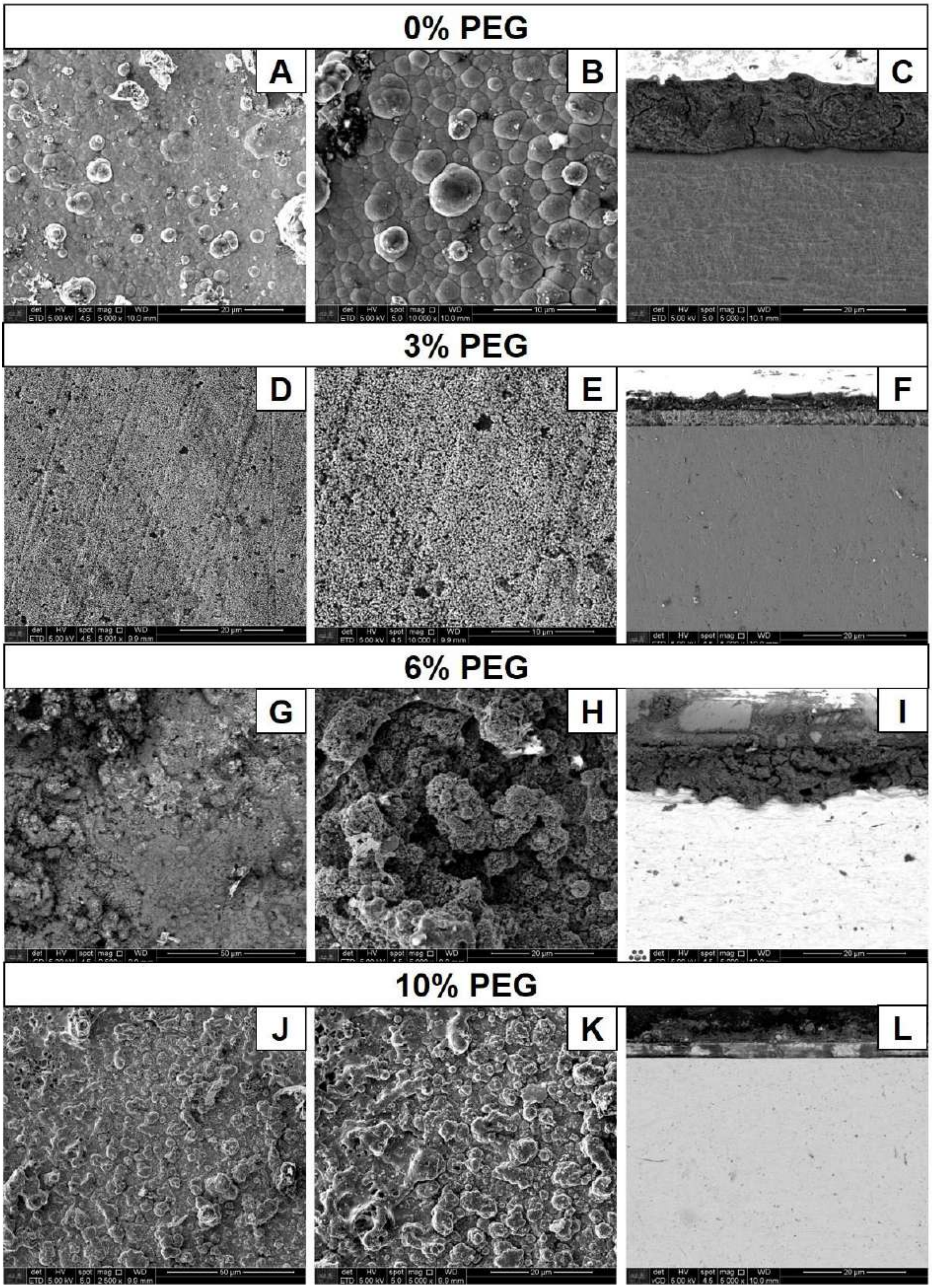

Figure 3-8 - FESEM micrographs of surface and cross-section of 0% PEG (A, B, C), 3% PEG (D, E, F), 6% PEG (G, H, I) and 10% PEG (J, K, L) samples.

Surface of coatings prepared in 3% PEG electrolyte are shown in Figure 3-8 D and E. Scratches from substrate surface preparation are still visible. Surface morphology consists of very fine nodular grain and with a higher density of pores. Cross-section Figure 3-8-F shows a compact layer with columnar grains and a smoother topography. Moreover, interface between the coating and the substrate is well-defined.

6% PEG sample surface has a porous feature, which can be seen in detailed in Figure 3-8-H. A similar morphology was observed by Huang et al. [18] when depositing Mo_2S coatings. The authors attributed this formation to a sintering effect promoted by the high temperature involved with the plasma discharge. This effect results from cataphoretic deposition of sub-macroparticles. When looking at cross-section image (Figure 3-8-I), it is possible to verify microcracks and pores on the coating, as well as a non-defined coating-substrate interface, possibly indicating a good coating adhesion.

Nodular morphology, but with a higher degree of porous compared to 0% PEG sample, is observed in 10% PEG sample. Crater-like surface is observed in Figure 3-8-K. The coating is thin, compact and with a well-defined interface just as the 3% PEG coatings. As discussed previously, current density peaks can be associated to bubbles implosion. 3% and 10% PEG samples exhibited lower current peak density and, probably, had fewer implosions during the deposition process. These samples had the more well-defined interface, which could be related to a less-efficient mechanical interlocking between coating and substrate. Mechanical interlocking is known to be associated to bubbles implosion and subsequent surface quenching [1].

3D optical profilometer images (Figure 3-9) indicated that the different electrolyte resulted in different surface topographies. It can be seen that roughness parameters, S_a and S_q, decreased with PEG content. Surfaces became smoother as PEG was added to the electrolyte. Bubble implosion is inhibited by the increased viscosity promoted by PEG addition. HSC images showed that bubble expansion was smaller for PEG samples, thus resulting in a milder implosion, which led to surfaces with smaller and sparser peaks. Besides, the obtained coatings are hydrophobic, but oleophilic (Figure 3-10). Electrodeposition of cobalt coatings in known to be a process that results in hierarchical rough surfaces with hydrophobicity [19].

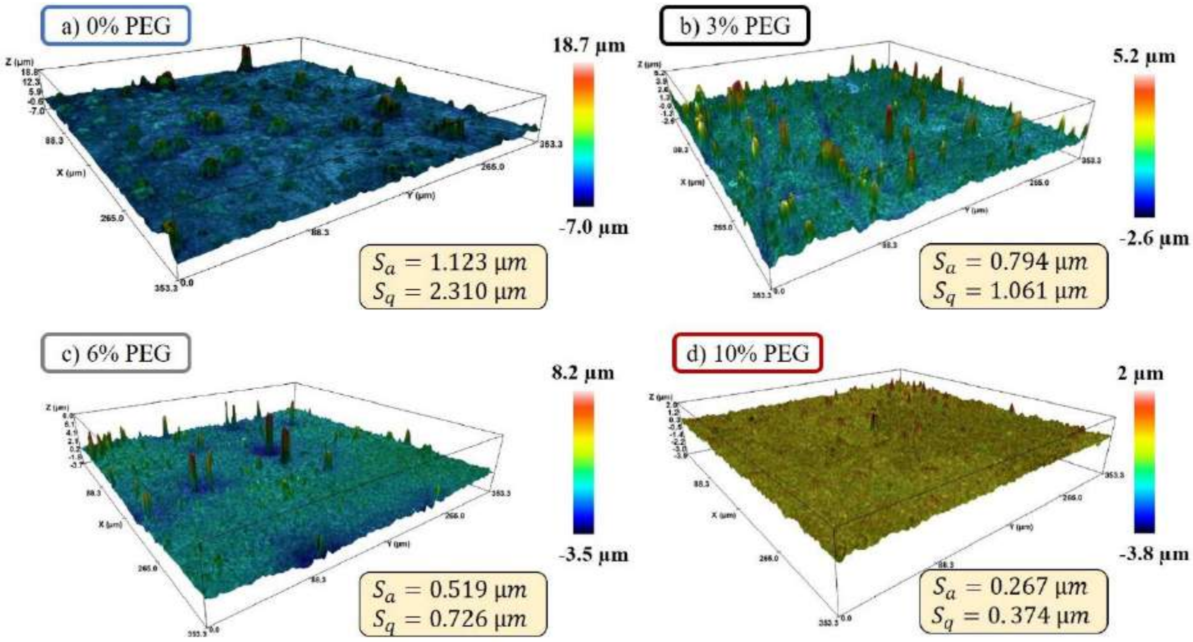

Figure 3-9 - 3D optical profilometer images showing surface topography. Roughness parameters (S_a and S_q) are indicated.

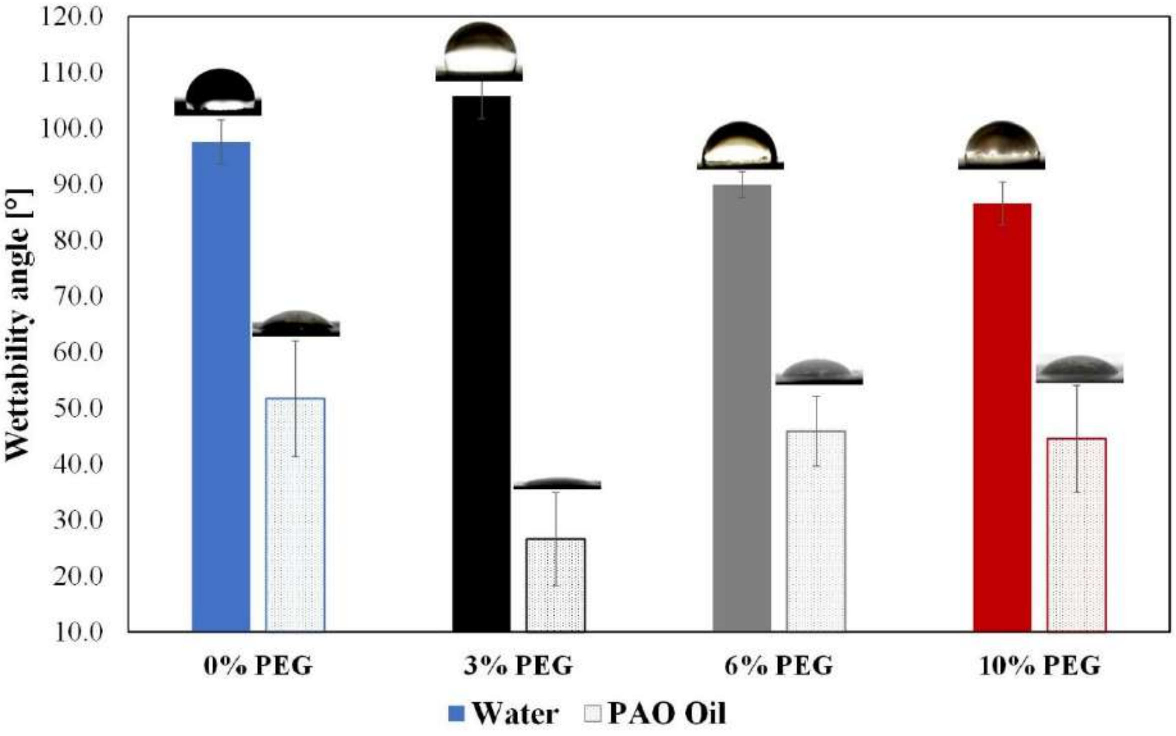

Figure 3-10 - Water and PAO oil wettability angles of 0%, 3%, 6% and 10% PEG samples.

Figure 3-11 shows scratch test results (normal load, tangential force, friction coefficient (COF) alongside with scratch distance) for 0%, 3%, 6% and 10% PEG samples. The critical loads (L_C), stereoscopic and 3D profilometer images are also displayed. Comparing the curves, it is possible to observe that 0% and 6% PEG coatings have the higher adhesion forces (76 and 74 N, respectively), which is in accordance with FESEM observations of cross-sections that showed a good mechanical interlocking with the substrate. At lower loads, ploughing of the coating material took place. As load increased, the detachment of coating from the substrate is observed in the pile-up regions. The debris from these extruded regions present grounding marks from substrate surface preparation (detailed in Figure 3-11.c), indicating the loss of adhesion between the coating and the substrate. This process is accompanied by the increase of COF variation. 3% PEG samples exhibited the lowest adhesion force (30 N). Coating spalling is clearly seen as the grounded substrate is exposed outside the crack. 10% PEG samples showed the same chipping of coating from the substrate at pile-up regions. It is detailed in Figure 3-11.d the coating almost completely detached from the substrate. Debris with grounding marks are also seen throughout the pile-up regions. 3% and 10% PEG samples exhibited lower adhesion forces as expected by its well-defined interfaces observed in FESEM images (Figure 3-8).

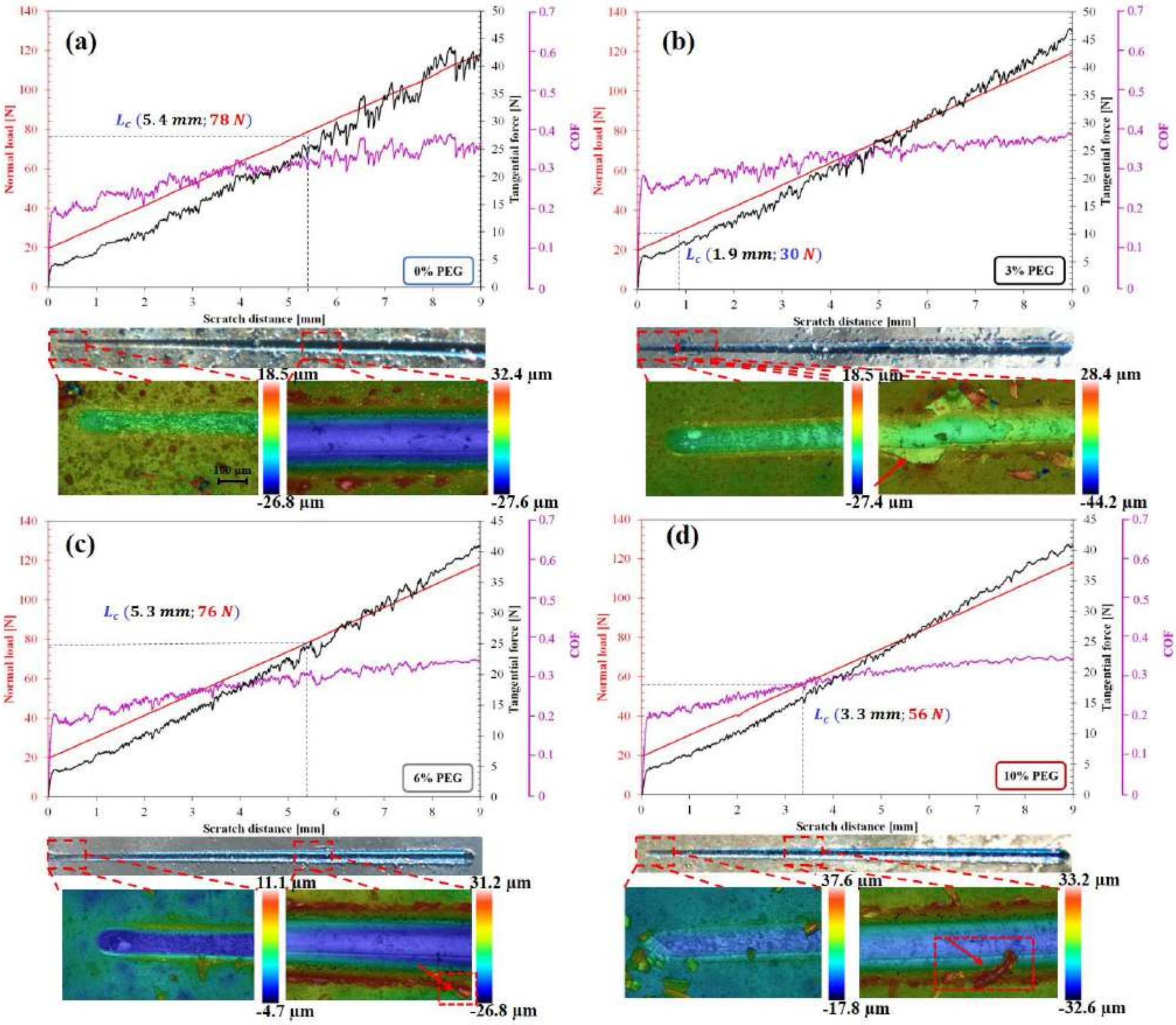

Figure 3-11 - Scratch test curves (normal load, tangential force, COF with scratch distance), stereoscopic images of the scratch and 3D profilometer images showing wear mechanisms of (a) 0%PEG, (b) 3% PEG, (c) 6%PEG and (d) 10%PEG. Critical scratch distance (L_C) and adhesion force are also indicated.

Coatings thickness and microhardness are shown in Figure 3-12. Surface hardness is around 570 $HV_{0.025kgf}$ and it is not affected by PEG addition. The measured hardness is inferior to that observed by Quan and He [7] which was around 710 $HV_{0,05kgf}$, but it is remarkably superior to that reported in conventional electrodeposition, around 200 $HV_{0,05kgf}$ [13]. The high hardness levels are attributed to the nanosized grain microstructure that resulted from the electrolyte quenching during CPED. The calculated grain size by Scherrer equation was inferior to 23 nm for all samples.

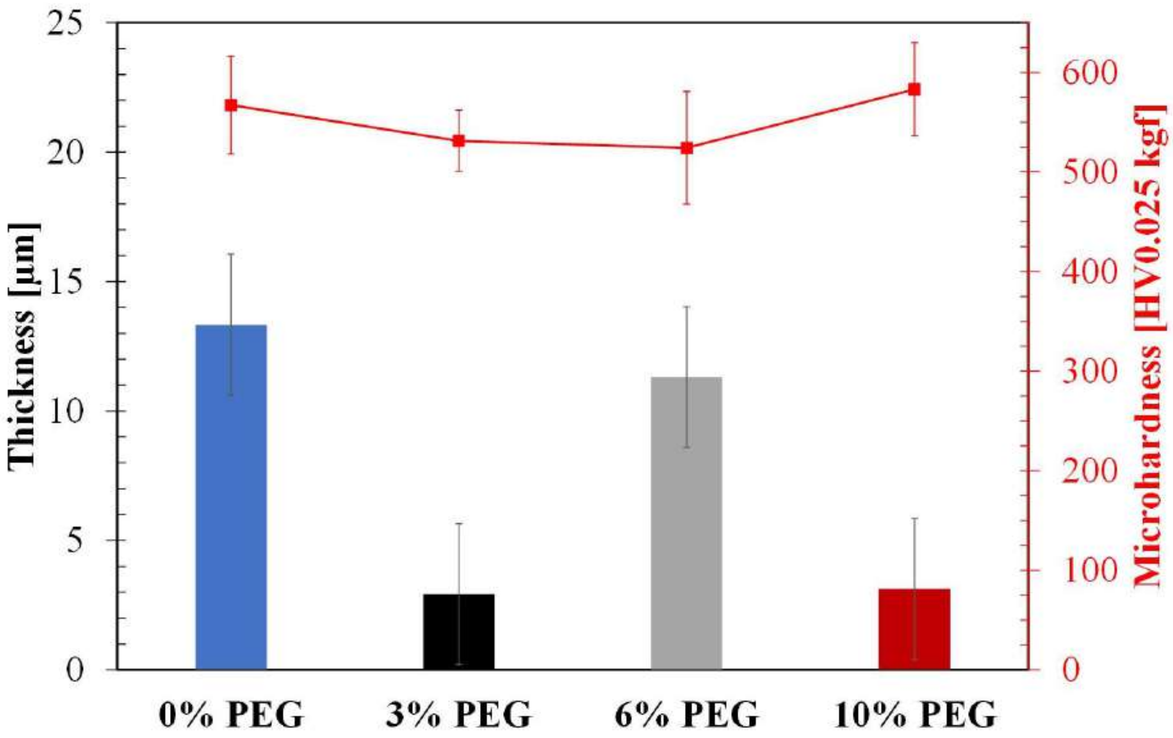

Figure 3-12 - Thickness and Vickers microhardness of obtained coatings.

0% and 6% PEG samples have similar thickness (13.3 µm and 11.3 µm respectively) as well as 3% and 10% PEG samples (2.9 µm and 3.1 µm respectively). 3% and 10% exhibited lower deviations. Thickness displayed the same trend as current peak density. Once again, the key is bubble implosion, given that it is known to be one of the main mechanisms of ion transporting [1-3]. Along with bubble implosion, cations which were concentrated around bubbles interface are accelerated towards the cathode by the void created and by the action of the high kinetic energy generated [1]. This phenomenon results in the deposition of cations onto the sample surface. Therefore, the samples which showed the larger thickness (0% and 6%) were those which had the highest current peak density.

PEG effect on the deposition has been downplayed. At the same time, it increases bubbles density on the surface of cathode due to increased viscosity, facilitating plasma discharge at lower currents. Apparently, it inhibits implosion phenomenon, which directly impairs deposition rates and hence coating thickness. HSC images showed that the higher PEG content, smaller was the implosion area. The higher viscosity could difficult bubbles coalescence, growth and collapse.

Table 3-5 shows the EDS analysis of each sample. Cobalt is the main element, but iron is also present probably due to the substrate. XRD results are shown in Figure 3-13. The peaks found matches with FCC α(200) and α(111) phase. ε-HCP (hexagonal compact) is the thermodynamically stable phase at ambient temperature, however α(FCC)→ε(HCP) is extremely slow, thus during CPED process, the cool electrolyte quenches the surface retaining metastable FCC phase. Cobalt deposits obtained by traditional electrodeposition process have HCP structures [13, 20]. Among the advantages of having a metastable FCC cobalt coating are the improved dielectric and soft magnetic properties [7] and, in a tribological perspective, strain-induced martensitic transformation (α(FCC)→ε(HCP)) during wear process can absorb part of the energy that would be used to material removal [21].

Table 3-5 - Element weight percent of coatings analyzed by EDS.

Sample	Co	Fe	O	C	Cu
0% PEG	93.7	4.9	0.8	0.3	0.3
3% PEG	94.1	2.4	1.7	1.2	0.6
6% PEG	93.5	5.5	0.5	0.2	0.3
10% PEG	94.0	5.2	0.5	0.3	-

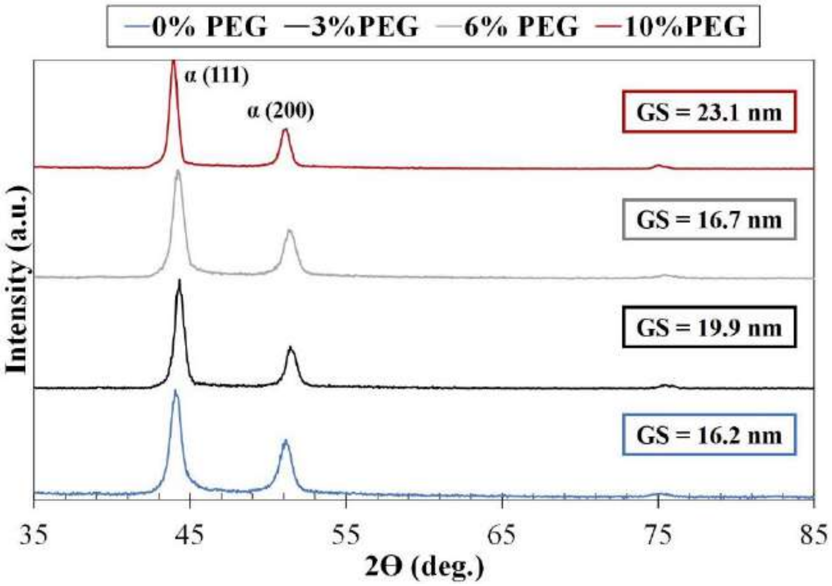

Figure 3-13 - XRD results of 0%, 3%, 6% and 10% PEG coatings. Grain size (GS) calculated by Scherrer's equation is indicated.

Friction coefficient curve with test time of the deposited coatings and the substrate (AISI 304) is shown in Figure 3-14. It is visible that coated samples, regardless of the electrolyte, have an inferior coefficient friction (0.12) when compared to the substrate. PEG effect on friction is minor. COF of 0% PEG samples is slightly superior probably due to its higher roughness. However, a greater variability between replicates is observed for samples deposited in PEG electrolytes, probably due to the higher level of porosity of those samples. Furthermore, it is interesting to note that despite the lower thickness displayed in 3% and 10% PEG coatings, friction coefficient remained low until the end of the test, indicating that the coating is still preserved on the surface.

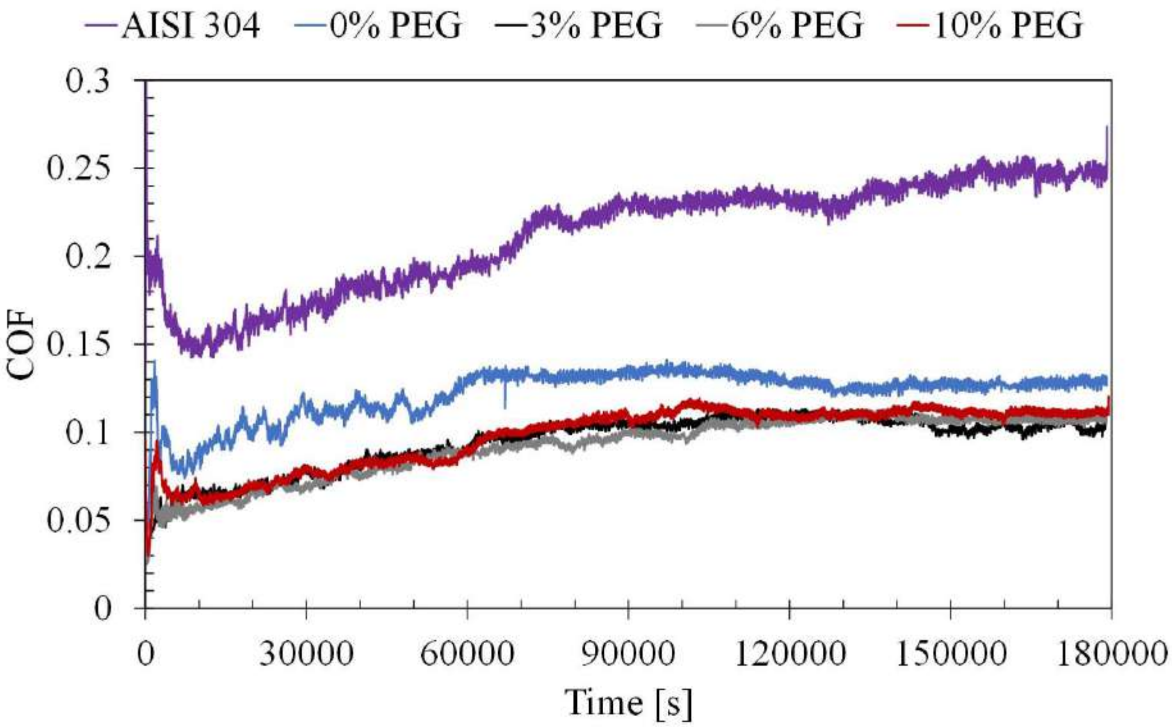

Figure 3-14 - Friction coefficient with test time for 0%, 3%, 6% and 10% PEG.

Wear losses results are displayed in Figure 3-15. Coatings deposited by CPED exhibited wear losses 2 times inferior to those of the substrate (AISI 304). Cobalt is known as a wear resistant material and its tribological properties are improved by the nanocrystalline microstructure which increases hardness and wear resistance [13, 20].

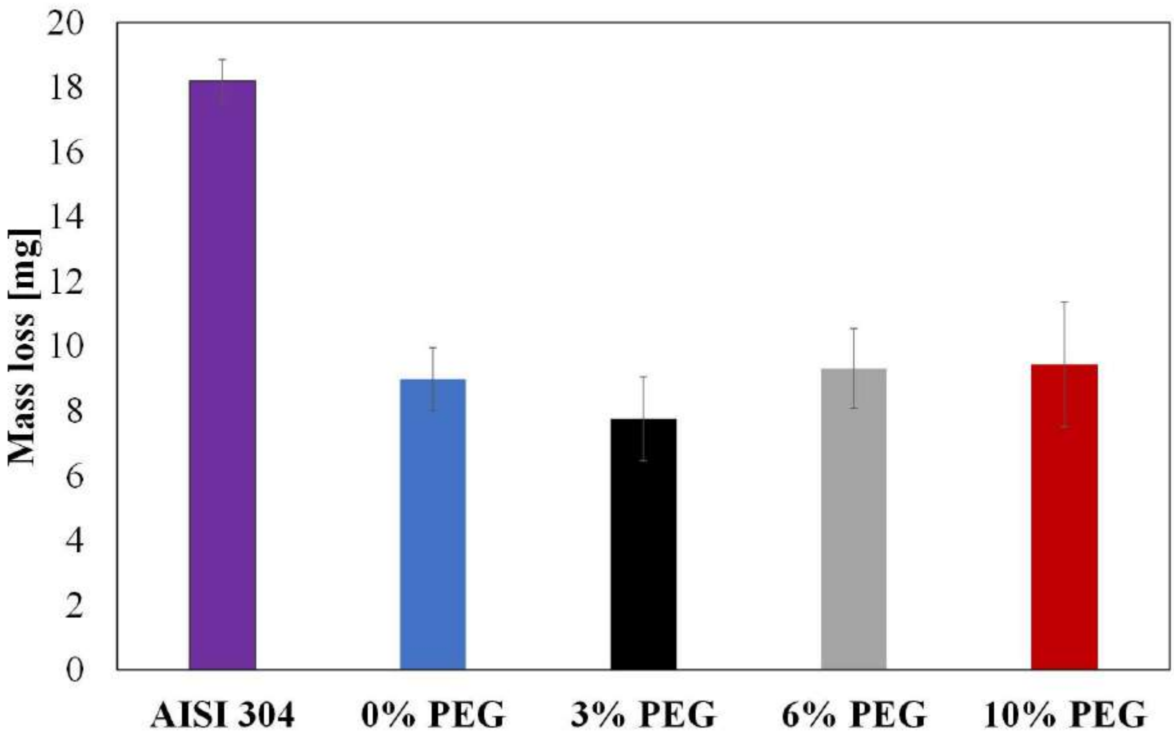

Figure 3-15 - Mass loss during test time for AISI 304, 0%, 3%, 6% and 10% PEG.

3.5. Conclusions

- A mechanism of coating deposition was proposed. When bubbles implode, a current peak is observed, due to the momentaneous contact of the conductive electrolyte with the sample surface. At this moment, cobalt ions are accelerated toward the surface, forming the deposit. Thus, a correlation between density of current peaks and thickness was established.
- PEG increased electrolyte viscosity, reducing bubble expansion and implosion severity, then, decreasing surface roughness.
- PEG addition did not alter hardness, nor friction and wear.
- 6% PEG samples exhibited thickness and adhesion forces similar to 0%PEG samples, while requiring a lower current for deposition.
- Nanocrystalline cobalt coating with high hardness and FCC metastable phase was formed. It showed 2 times wear reduction compared to the substrate AISI 304.

References

[1] Gupta, P., Tenhundfeld, G., Daigle, E. O., & Ryabkov, D. (2007). Electrolytic plasma technology: Science and engineering—An overview. Surface and Coatings Technology, 201(21), 8746-8760.

[2] Yerokhin, A. L., Nie, X., Leyland, A., Matthews, A., & Dowey, S. J. (1999). Plasma electrolysis for surface engineering. Surface and coatings technology, 122(2-3), 73-93.

[3] Paulmier, T., Bell, J. M., & Fredericks, P. M. (2007). Development of a novel cathodic plasma/electrolytic deposition technique: Part 2: Physico-chemical analysis of the plasma discharge. Surface and Coatings Technology, 201(21), 8771-8781.

[4] Parfenov, E. V., Yerokhin, A., Nevyantseva, R. R., Gorbatkov, M. V., Liang, C. J., & Matthews, A. (2015). Towards smart electrolytic plasma technologies: An overview of methodological approaches to process modelling. Surface and Coatings Technology, 269, 2-22.

[5] Pogrebnyak, A. D., Kaverina, A. S., & Kylyshkanov, M. K. (2014). Electrolytic plasma processing for plating coatings and treating metals and alloys. Protection of Metals and Physical Chemistry of Surfaces, 50(1), 72-87.

[6] Aliofkhazraei, M., & Roohaghdam, A. S. (2007). A novel method for preparing aluminum diffusion coating by nanocrystalline plasma electrolysis. Electrochemistry Communications, 9(11), 2686-2691.

[7] Quan, C., & He, Y. (2015). Microstructure and characterization of a novel cobalt coating prepared by cathode plasma electrolytic deposition. Applied Surface Science, 353, 1320-1325.

[8] Zhao, G., & He, Y. (2012). Plasma electroplating Ni coating on pure copper sheet—the effects of H2SO4 concentration on the microstructure and mechanical properties. Surface and Coatings Technology, 206(21), 4411-4416.

[9] Gupta, P., Tenhundfeld, G., Daigle, E. O., & Schilling, P. J. (2005). Synthesis and characterization of hard metal coatings by electro-plasma technology. Surface and coatings technology, 200(5-6), 1587-1594.

[10] Quan, C., & He, Y. (2015). The morphology change of Co coatings prepared by cathode plasma electrolytic deposition. Materials Letters, 153, 92-95.

[11] Landolt, D. (1994). Electrochemical and materials science aspects of alloy deposition. Electrochimica Acta, 39(8-9), 1075-1090.

[12] Mahdavi, S., & Allahkaram, S. R. (2013). Characteristics of electrodeposited cobalt and titania nano-reinforced cobalt composite coatings. Surface and Coatings Technology, 232, 198-203.

[13] Hyie, K. M., Resali, N. A., Abdullah, W. N. R., & Chong, W. T. (2012). Synthesis and characterization of nanocrystalline pure cobalt coating: effect of pH. Procedia Engineering, 41, 1627-1633.

[14] Wang, P., Deng, S., He, Y., Liu, C., & Zhang, J. (2016). Influence of polyethylene glycol on cathode plasma electrolytic depositing Al2O3 anti-oxidation coatings. Ceramics International, 42(7), 8229-8233.

[15] Liu, C., Zhang, J., He, Y., Zhang, S., Wang, P., Lian, Y., & Deng, S. (2017). Synergistic effect of PEG and hydrosol treatments of solution on preparing Al2O3 coating by cathode plasma electrolytic deposition. Materials Research Express, 4(3), 036306.

[16] Zhang, H., Zhang, N., & Fang, F. (2020). Electrodeposition of nickel/graphene oxide particle composite coatings: effect of surfactants on graphene oxide dispersion and coating performance. Journal of the Electrochemical Society, 167(16), 162501.

[17] Chen, Z., Zhou, K., Lu, X., & Lam, Y. C. (2014). A review on the mechanical methods for evaluating coating adhesion. Acta Mechanica, 225(2), 431-452.

[18] Huang, J., Zhu, J., Fan, X., Xiong, D., & Li, J. (2018). Preparation of MoS2-Ti (C, N)-TiO2 coating by cathodic plasma electrolytic deposition and its tribological properties. Surface and Coatings Technology, 347, 76-83.

[19] Alinezhadfar, M., Abad, S. N. K., & Mozammel, M. (2020). Multifunctional cobalt coating with exceptional amphiphobic properties: self-cleaning and corrosion inhibition. Surfaces and Interfaces, 21, 100744.

[20] Wang, L., Gao, Y., Xu, T., & Xue, Q. (2006). A comparative study on the tribological behavior of nanocrystalline nickel and cobalt coatings correlated with grain size and phase structure. Materials Chemistry and Physics, 99(1), 96-103.

[21] Farooq, M. U., Klement, U., & Nolze, G. (2007). The role of α-to ε-Co phase transformation on strain hardening of a Co–Cr–Mo laser clad. Materials Science and Engineering: A, 445, 40-47.

Chapter 04

4. On the tribological behavior of cobalt-based nanocomposite coatings containing ZnO@Graphene Oxide core-shell nanoparticles

4.1. Abstract

A hybrid nanocrystalline cobalt-based coating was prepared by cathode plasma electrolytic deposition (CPED). Zinc oxide and graphene oxide (GO) nanoparticles were mixed to form a core-shell structure through electrostatic self-assembly by using (3-aminopropyl)triethoxysilane (APTES) modifier. ZnO@GO nanoparticles were used as additives to improve wear and friction properties of deposited coatings. The concentration effect of core-shell ZnO@GO addition (0.1, 0.2 and 0.3 %wt) on the friction, wear, coating thickness and mechanical properties was investigated. The composition and microstructure of deposited coatings were studied by scanning electron microscope (SEM), X-ray diffraction (XRD), Raman spectroscopy and energy dispersive spectroscopy (EDS). Reciprocating sliding wear tests using a ball-on-plate configuration were carried out on a PLINT TE67 tribometer. AISI 52100 steel was used as ball and the coating deposited onto a AISI 304 stainless steel substrate was used as plate. Coatings were dense, nanocrystalline and uniform with a FCC metastable cobalt structure. Core-shell concentration above to 0.2 %wt resulted in a decrease of grain size and an increase of hardness and wear resistances. Nanoparticles act as nucleation sites for grain formation, decreasing grain sizes. Samples using 0.3% ZnO@GO displayed the lowest wear and friction coefficients. ZnO@GO nanoparticles enables the formation of a protective layer consisting of oxide and exfoliated GO on the top of worn surfaces.

Keywords: Cathode plasma electrolysis deposition; Cobalt coatings; Core-shell; Sliding wear.

4.2. Introduction

Cobalt is an important engineering material with high wear and corrosion resistances. Its unique properties such as high hardness, biocompatibility and magnetic properties justifies its use in microelectronics, sensor technology and in the defense industry [1-3]. Multiple methods have been used to deposit cobalt coatings, but among them cathodic plasma electrolysis deposition (CPED) stands out due to its high deposition rates, no need for electrolyte additives and to the deposition of nanocrystalline coatings with high hardness and adhesion. CPED emerges as a result of the combination of conventional electrolysis with atmospheric plasma processing [4-5].

Cobalt and nickel coatings are eco-friendly alternatives to conventional chromium deposits which uses hazardous and source of pollution hexavalent chromium plating [6-8]. However, cobalt outstands nickel due to its better tribological response with an increase resistance to adhesion and delamination wear, resulting in lower and stabler friction coefficient compared to nickel [8,9]. Furthermore, cobalt has an excellent thermal stability [10,11].

Nanoparticles (NPs) have been used in electrodeposition process in order to improve mechanical, wear and corrosion resistances [12]. NPs increase nucleation sites and hinder crystal grow, resulting in smaller grain sizes and in higher hardness [11]. A reduction of pore fraction is also expected, which improves corrosion resistance by prohibiting corrosive ions to enter [13].

Different composite cobalt-based coatings had been deposited using different particles such as SiC [10], carbon nanotubes [14], TiO_2 [2] and WC [15] in order to decrease wear and corrosion. Liu et al. [11] added graphene oxide (GO) NPs to cobalt coating using conventional electrolysis process. The authors observed that GO addition affected the morphology of deposits, leading to grain refinement, hardness increase and friction reduction (from 0.65 to 0.33). While cobalt pure exhibited severe adhesive wear, the coating with embedded GO showed abrasive wear and mild adhesive wear.

Toosinezhad et al. [13] electrodeposited Co/graphene coatings on ST37 steel substrate. Graphene was successfully distributed within the matrix and 0.2 g/L content led to the best tribological response, reducing the friction in 1.6 times and wear in 5.5 times compared to Co pure film. Besides, surface morphology depended on concentration, increasing graphene content morphology changed from pyramidal grains to needle shape grains.

NPs addition in CPED process has also been reported. Huang et al. [16] added Mo_2S nanoparticles to form a Ti(C,N) based composite with outstanding lubricating properties. The authors observed that Mo_2S weaken electrolyte capacity to cool the sample during CPED as it reduces electrolyte flowing capacity.

Liu et al. [17] observed that SiC nanoparticles positively affected the electrical behavior of CPED when depositing Al2O3 composite coatings. The destructive effect of plasma breakdown is diminished, resulting in a smoother and wear resistant coating. Furthermore, the authors underlined that friction and wear only decrease for appropriate NPs concentrations. Quan et al. [18] showed that the addition of Y2O3 NPs to Ni-Cr based electrolytes enabled Cr2O3 growth in a very small scale, greatly increasing corrosion resistance.

There is a lack of literature concerning the use of core-shell nanoparticles as additives to electrodeposited coatings. These particles show a synergistic effect on the tribological contact. The hard core supports the normal load while the soft shell works as a solid lubricant. In this work, cobalt-based coatings using different contents of core-shell ZnO@GO core-shell NPs as additives were deposited by CPED. The tribological behavior of those hybrid coatings were investigated and the influence of core-shell NPs addition on wear and friction was scrutinized. Mechanical properties, microstructure and surface topography were also investigated.

4.3. Experimental

4.3.1. Preparation of ZnO@GO core-shell NPs

GO was synthetized from natural graphite powder by a modified Hummers method [19]. 1 g of graphite and 0.5 g of $NaNO_3$ were added to 70 ml of H_2SO_4 and stirred in an ice bath. 3 g of $KMnO_4$ was slowly added to the solution and stirred for 2 h. Then, 3 ml of 30% H_2O_2 was gradually added and the solution was diluted with distilled water. The solid product was collected after washing and centrifugation. The product was dried at 60°C for 24 h. In order to obtain core-shell ZnO@GO NPs [20], firstly, 1 g of ZnO NPs (50 nm spherical-shaped nanoparticles supplied by Sigma-Aldrich) were dispersed in a mixture of 45 ml distilled water and 105 ml ethanol, stirred, and then mixed with 0.2 g of (3-aminopropyl)triethoxysilane (APTES) (99%, ChemImpex) to functionalize ZnO surface with positive amino groups. The solution was stirred for 7 hours at room temperature to complete hydrolysis of APTES. Functionalized ZnO nanoparticles were centrifuged, washed and dried at 80°C for 15 h.

Core-shell ZnO@GO NPs [21] were prepared by electrostatic self-assembly. 0.5 g of GO was added to a mixture of 700 ml distilled water and 35 ml of ethanol. The solution was sonicated for 20 min and stirred for 40 min to produce a well-dispersed solution. Then, 1 g of functionalized ZnO was added to the solution and stirred for 1 h. The final ZnO@GO were washed, centrifuged and dried at 70°C for 24 h.

4.3.2. CPED of cobalt-based coatings

A DC power supply (0 - 120 V) was used and a data acquisition system connected to a computer was used to monitor current and voltage. The electrolyte was recirculated and cooled by using a 200 l/h flow rate pump and an iced bath, respectively. Electrolyte temperature was monitored during the process using a thermocouple. A graphite (99.9% purity) plate was used as the anode and the anode-cathode distance was 30 mm. Austenitic stainless-steel AISI 304 plate samples were used as cathode. Samples were grounded to a 1200 grit, ultrasonically cleaned with acetone for 15 min. Deposition area was bounded and fixed in 1 cm^2 by an ABS polymer holder. The electrolyte consisted of $CoSO_4.7H_2O$ (25 g/l), H_2SO_4 (60 g/l) and distilled water was used as solvent. To deposit Co ZnO@GO hybrid coatings, ZnO@GO NPs were added to the electrolyte in different content (0, 0.1, 0.2, and 0.3 g/L). Ultrasonic sonication during 30 min prior to deposition and electrolyte recirculation ensure the homogenizing of the electrolyte. Deposition was carried out at 85 V for 3 min.

4.3.3. Characterization

ZnO@GO nanoparticles were characterized by Raman spectroscopy in a LabRam HR Evolution spectrometer, using a 633 nm laser, 50x objective and 90 mW laser power. X-ray diffraction (XRD) were carried out on a Rigaku Ultima diffractometer using molybdenum radiation ($\lambda = 7.0926\,\mathrm{nm}$) to identify each phase. A FEI-Inspect F50 field-emission scanning electron microscopy (FESEM) with an X-ray energy dispersive spectrometer (EDS) and Transmission electron microscope (TEM) were used to evaluate NPs morphology, size and composition.

Co and Co/ZnO@GO coatings were characterized by XRD and Raman spectroscopy. An 3D optical profilometer (SNeox, Sensofar) was used to evaluate surface topography. FESEM imaging was carried out to investigate surface morphology and coating thickness while EDS was used to analyze the composition of the coatings. Vickers microhardness tests were carried out using a load of 25 gf. Ten indentations were done in each sample.

Ball-on-plate sliding tests were carried out on a PLINT TE67 tribometer (Phoenix Tribology Ltd) using the AISI 304 coated samples as the plate and an AISI 52100 steel as the ball. Tests were performed with a stroke length of 2.5 mm, a sliding frequency of 3 Hz and a normal load of 500 N. The initial Hertz contact pressure was 0.7 GPa. Test duration was 30 min. Friction force was monitored throughout the test using a load cell with 10 Hz acquisition frequency. Ball and plate were ultrasonically cleaned with acetone for 15 min prior the test. Tests were performed in a random order.

Mass loss was determined using an analytical balance with 0.1 mg precision. After wear tests, main wear micro-mechanisms were determined by FESEM image analysis of the wear track. Tribolayer formation on the wear track was evaluated by EDS.

4.4. Results and discussion

4.4.1. Characterization of ZnO@GO nanoparticles

Figure 4-1 shows SEM image, TEM image, EDS spectrum, XRD pattern and Raman spectrum of ZnO@GO nanoparticles prepared in this experiment. It can be seen in Figure 4-1 that ZnO nanoparticles are imbedded in GO layers, forming a nanocluster and EDX results confirms Zn, C and O presence. Figure 4-1c confirms that ZnO nanoparticles were successfully coated with a thin GO layer, resulting in a core-shell nanostructure. The diffraction pattern depicted in Figure 4-1d shows a wide peak at 11.2° correspondent to GO [22] and several ZnO peaks indicating the formation of hexagonal wurtzite phase [23]. Figure 4-1e shows Raman spectrum of ZnO@GO nanoparticles exhibiting two characteristic peaks of GO at 1337 cm^{-1} and 1584 cm^{-1}, which correspond to disordered D band and crystalline G band, respectively [22,23]. The intensity ratio of the D band and G band (I_D/I_G) is 1.22. The spectrum also reflects the formation of hexagonal wurtzite. Peaks at 339 cm^{-1} corresponding to A1 vibration mode, at 441 cm^{-1} representing E2 high non-polar mode and a broad band at 1154 cm^{-1} corresponding to the A1 transversal optical (TO) and longitudinal optical (LO) modes [24] are present.

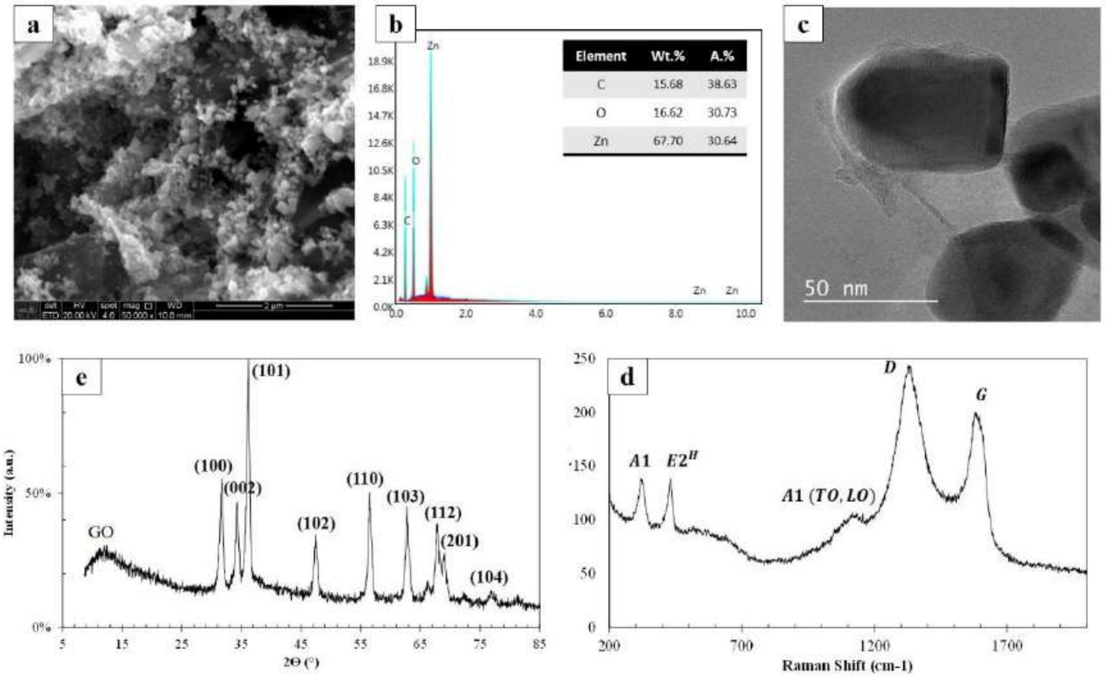

Element	Wt.%	A.%
C	15.68	38.63
O	16.62	30.73
Zn	67.70	30.64

Figure 4-1 - (a) SEM image, (b) EDS spectrum, (c) TEM image, (d) XRD pattern and (e) Raman spectrum of ZnO@GO core-shell nanoparticles.

4.4.2. Morphology and microstructure of the coatings

SEM images of surfaces and cross-sections and EDS analysis of Co and Co/ZnO@GO composite coatings are shown in Figure 4-2. Pure Co coating exhibited a porous and rough microstructure. Cross-section image shows a higher thickness when compared to composite coatings, but microcracks are clearly seen. A spheroidal nodule morphology is observed in all coatings, which is derived from the subsequent implosion and quenching of surfaces [25]. However, with nanoparticle addition, nodules are smaller and surfaces are smoother. Nanoparticles can act as new nucleation sites and hinder crystal growth process [11,13]. EDS analysis confirms the deposition of ZnO@GO nanoparticles along the cobalt matrix. The content of carbon, oxygen and zinc increase with the content of ZnO@GO added to the electrolytic bath. Besides, coatings with high-purity were obtained, since no additives were required. Using 0.3 g/L of ZnO@GO, a double layer was formed. A thicker top layer composed of Zn, C and O in a cobalt matrix was formed and a bottom layer composed of the same elements of the core-shell nanoparticles, but in an iron matrix. From these results, it can be proposed that at higher contents, more ZnO@GO is available, migrating faster and nucleating first. By the action of plasma, local melting occurs and nanoparticle are incorporated into the iron matrix, forming an iron-based coating. With the progression of plasma process, cobalt ions also migrate, enabling the cobalt-based coating formation.

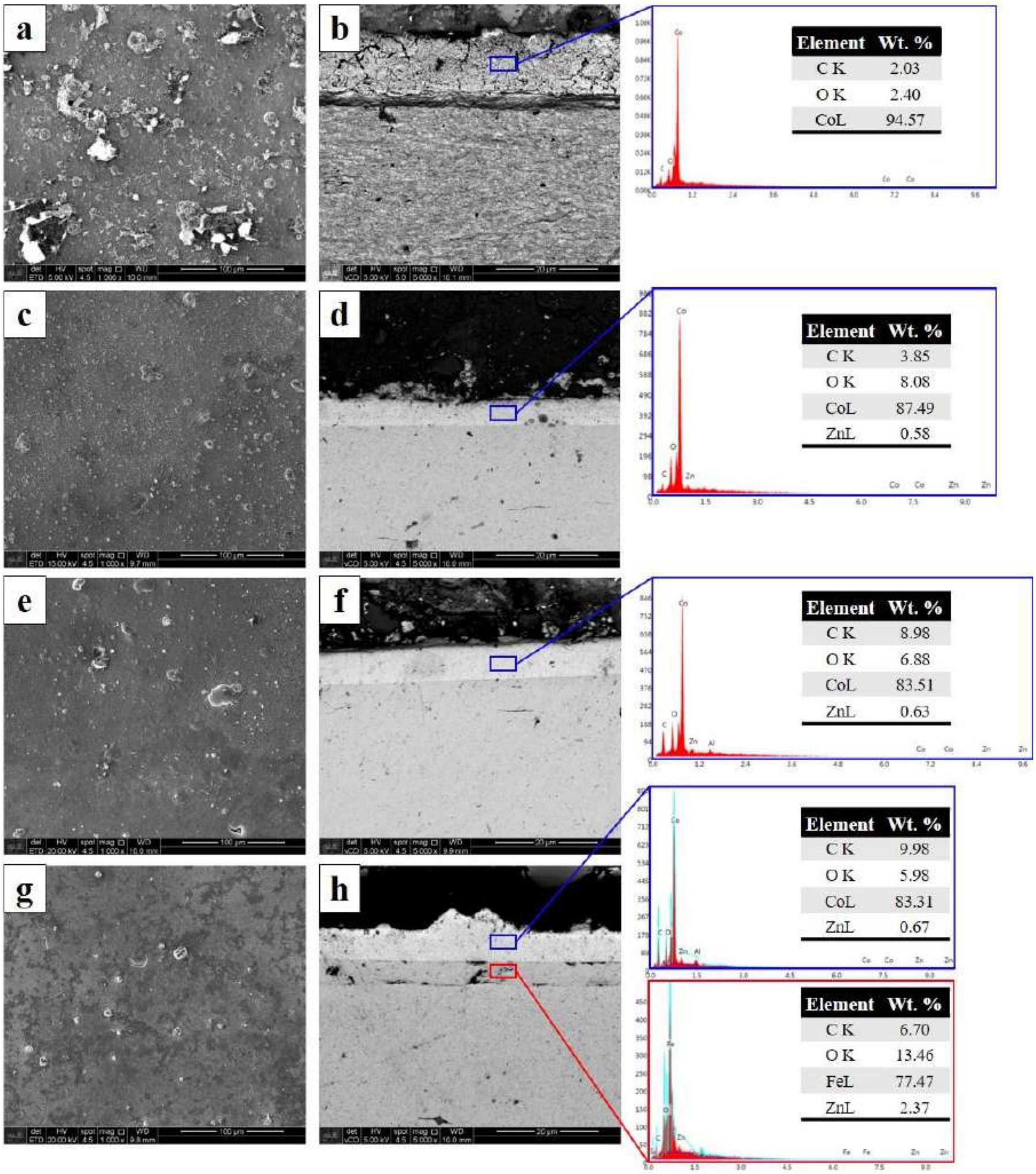

Element	Wt. %
C K	2.03
O K	2.40
CoL	94.57

Element	Wt. %
C K	3.85
O K	8.08
CoL	87.49
ZnL	0.58

Element	Wt. %
C K	8.98
O K	6.88
CoL	83.51
ZnL	0.63

Element	Wt. %
C K	9.98
O K	5.98
CoL	83.31
ZnL	0.67

Element	Wt. %
C K	6.70
O K	13.46
FeL	77.47
ZnL	2.37

Figure 4-2 - SEM images of deposited coatings by CPED: Co (a) surface (b) cross-section, Co0.1g/L ZnO@GO (c) surface, (d) cross-section, Co0.2 g/L ZnO@GO (e) surface (f) cross-section, Co0.3 g/L ZnO@GO (g) surface (h) cross-section. EDS analysis of coatings are in detail.

Figure 4-3a shows diffraction patterns of the Co and Co0.3g/L ZnO@GO. Both coatings display strong metastable face-centered cubic (FCC) α(200) and α(111) peaks [26], differently from coatings deposited through traditional electrolysis methods, which typically show hexagonal compact (HCP) structure [8]. In addition, peak broadening is observed in both samples indicating nanograin formation. Average grain size was calculated using Scherrer's equation from XRD patterns, Co has 20.1 nm grains and Co0.3 g/L ZnO@Go has 18.7 nm grains. During CPED grains are nucleated and subsequently quenched by the cool electrolyte, promoting nanograins and metastable microstructures formation [25]. Besides, when 0.3 g/L ZnO@GO was added, it resulted in grain refinement and, consequently, microhardness increase, as can be seen in Figure 4-4 [27].

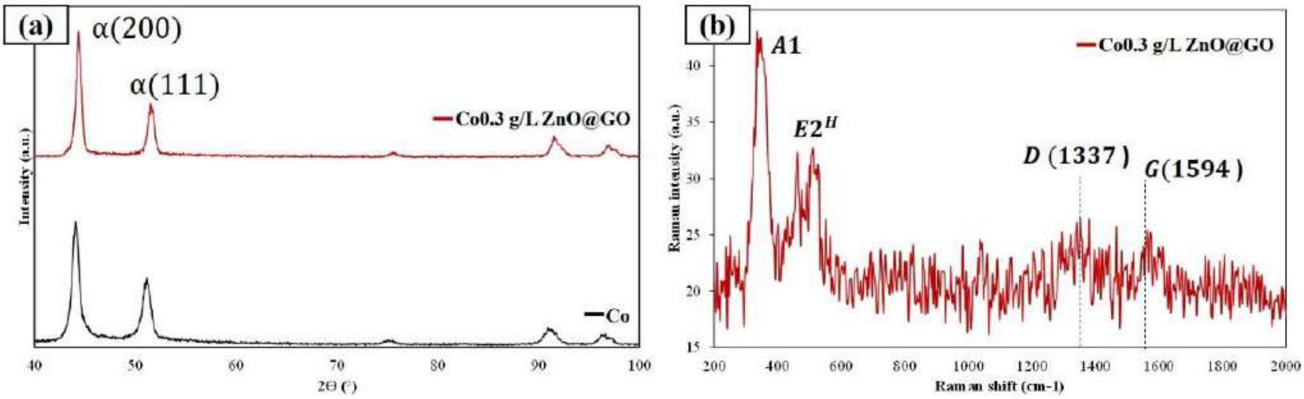

Figure 4-3 - (a) XRD patterns of Co and Co0.3g/L ZnO@GO (b) Raman spectrum of Co0.3g/L ZnO@GO.

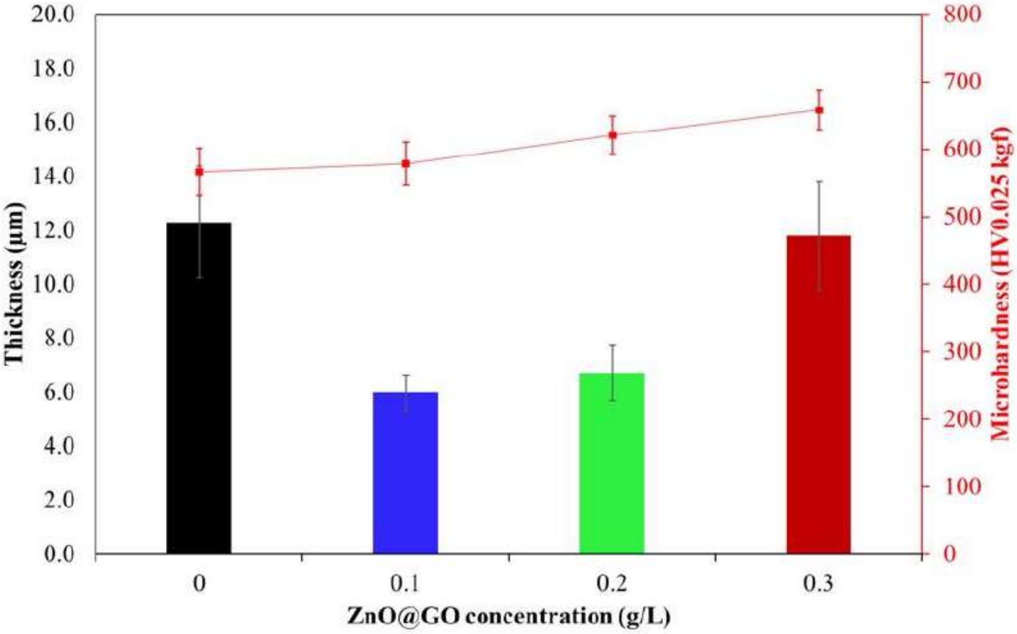

Figure 4-4 - Thickness and microhardness of Co, Co0.1 g/L ZnO@GO, Co0.2 g/L ZnO@GO and Co0.3 g/L ZnO@GO.

Thickness of coatings (Figure 4-4) were also affected by nanoparticles addition. 0.1 and 0.2 g/L ZnO@GO addition decreased coating thickness, but at the same time produced more even and smoother coatings. 0.3 g/L of ZnO@GO addition resulted in a double layer, iron-based and cobalt-based, with thickness similar to the Co coating. Raman spectroscopy results of Co0.3 g/L ZnO@GO (Figure 4-3b) confirms ZnO peaks at 339 cm^{-1} and 441 cm^{-1} and broad GO D 1337 cm^{-1} and G 1594 cm^{-1}.

3D profilometry results (Figure 4-5) shows that composite coatings are smoother, displaying smaller S_a and S_q topography parameters. Nanoparticle addition was effective in decreasing porosity and roughness.

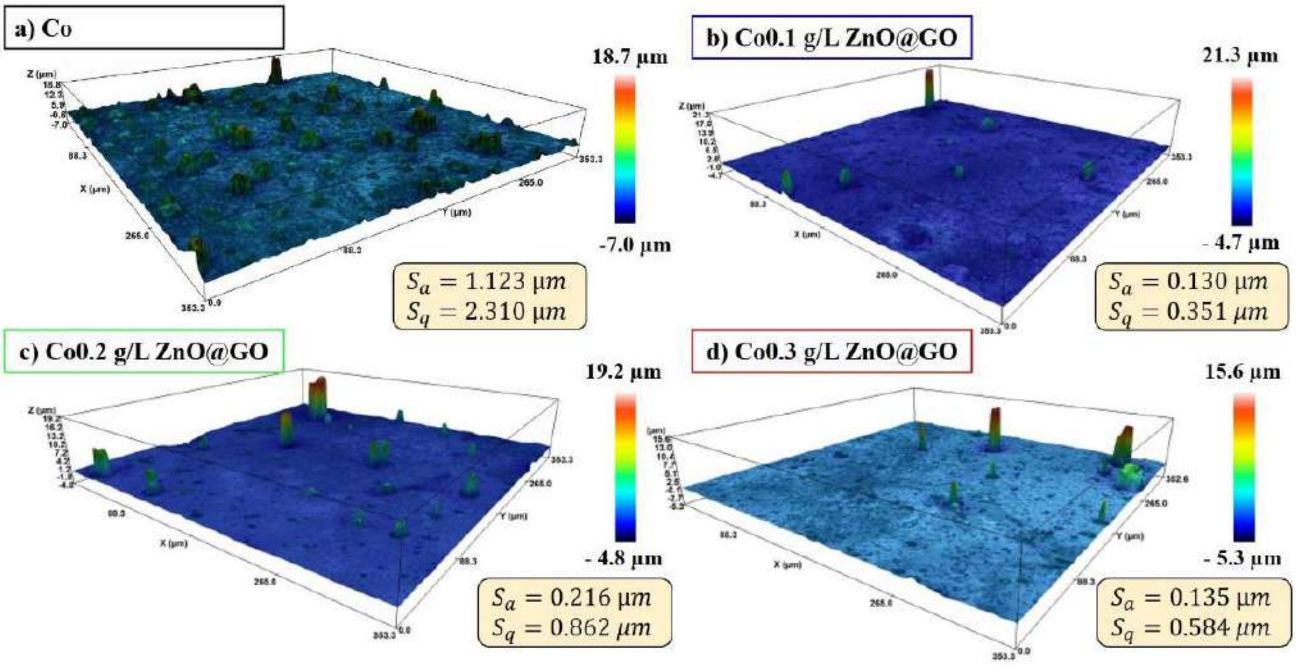

Figure 4-5 - 3D profilometry results of of Co, Co0.1 g/L ZnO@GO, Co0.2 g/L ZnO@GO and Co0.3 g/L ZnO@GO. S_a and S_q roughness parameters are displayed.

4.4.3. Tribological results

Friction coefficient curves of Co and Co composite coatings are shown in Figure 4-6. Friction coefficient of Co coating increases with time, reaching 0.12 after 700 s. This friction level is maintained throughout the rest of the test. Co0.1g/L ZnO@GO coatings displayed the same trend and friction coefficient as pure Co coatings. However, when adding higher amounts of nanoparticles, composite coating exhibited reduced friction coefficient. Both, Co0.2g/L ZnO@GO and Co0.3g/L ZnO@GO friction curves had prolonged running-in periods (1200 s) and lower steady-state friction coefficient. 0.3 g/L of nanoparticles addition resulted in the lowest friction coefficient (0.09) against the steel ball.

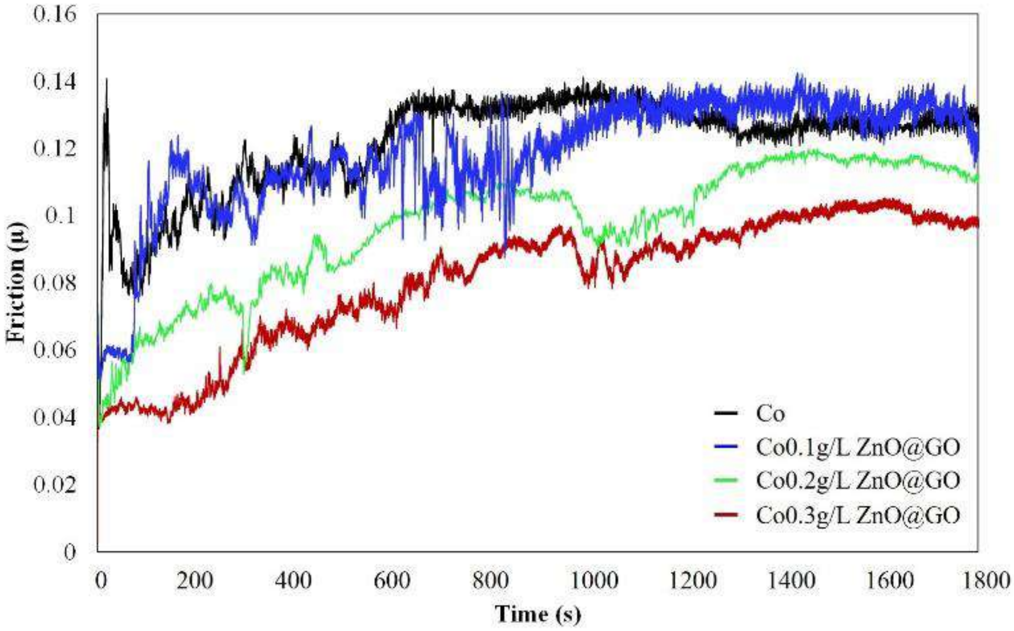

Figure 4-6 - Friction coefficient curves for Co, Co0.1g/L ZnO@GO, Co0.2g/L ZnO@GO, Co0.3g/L ZnO@GO.

The wear loss of the coatings during the tests are summarized in Figure 4-7. Compared with ZnO@GO free Co, the wear of Co0.2 g/L ZnO@GO and Co0.3 g/L ZnO@GO were reduced 20% and 22%, respectively. The wear loss of Co0.1g/L ZnO@GO was similar to Co coatings, the difference is between error bars. GO nanoparticles are known as excellent solid lubricant, which reduce friction and wear [11,28]. Moreover, the addition of core-shell nanostructures which possess the synergy of the ZnO hard core and the GO flexible shell are probably responsible for the improved wear and friction properties of Co0.2 g/L ZnO@GO and Co0.3 g/L ZnO@GO [23].

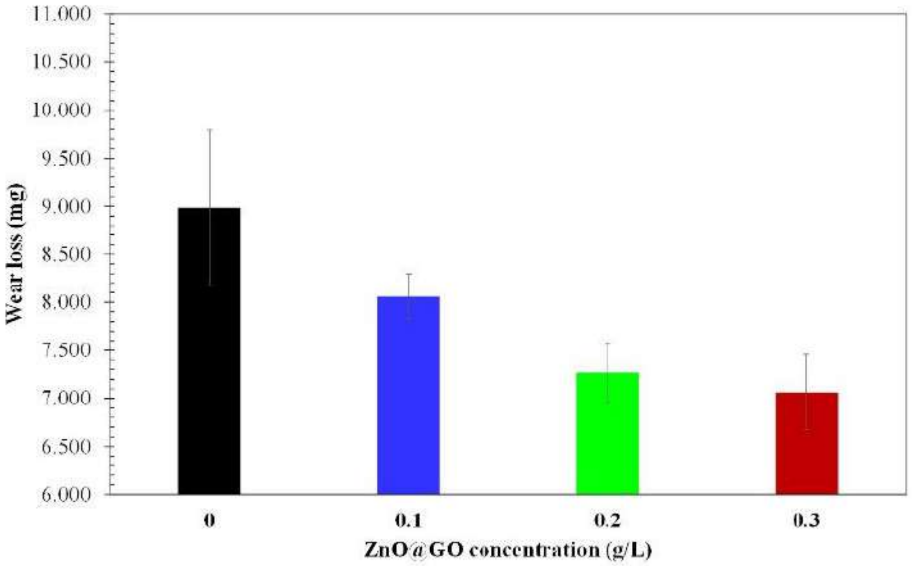

Figure 4-7 - Wear loss for Co, Co0.1g/L ZnO@GO, Co0.2g/L ZnO@GO, Co0.3g/L ZnO@GO sliding in air against AISI 52100 steel ball under a normal load of 500 N.

As shown in Figure 4-8, all deposited coatings exhibited severe plastic deformation, denoting adhesive wear. A tribo-layer formation is observed in the top of Co coatings. EDS analysis indicates that this build-up is high in oxygen and iron. Microcracks are seen inside this layer, which lead to the detachment of large oxide particles alongside with bulk material. The lower positions of the sample surface are regions with actual metal-metal contact and are severely deformed. During wear, oxide material of the ball can be transferred to the plate due to the severe contact conditions. Besides, in some regions, the Co coatings is also removed, exposing the substrate. This removed material is mixed with the iron oxide transferred material, forming a tribolayer that contributes to reduce the friction coefficient of the tribo-pair.

Co composite coatings displayed similar wear mechanisms. Co0.2/L ZnO@GO and Co 0.3g/L ZnO@GO coatings also exhibited the formation of oxide layer. However, the lower positions are less deformed. Striation marks can be observed as a result of the consecutive cycles of plastic extrusion. Abrasion grooves as well as fine wear debris are seen, indicating that three-body abrasion also takes place, but due to the small scale of the particles, its contribution to wear is minor. EDS results showed strong peaks of oxygen and iron, but also, indicates the presence of C. GO is exfoliated on the contact, contributing to form a tribolayer that exhibited lower friction and wear. Besides, C is detected only on the oxide film areas. Oxide film helps to retain exfoliated GO in the surface.

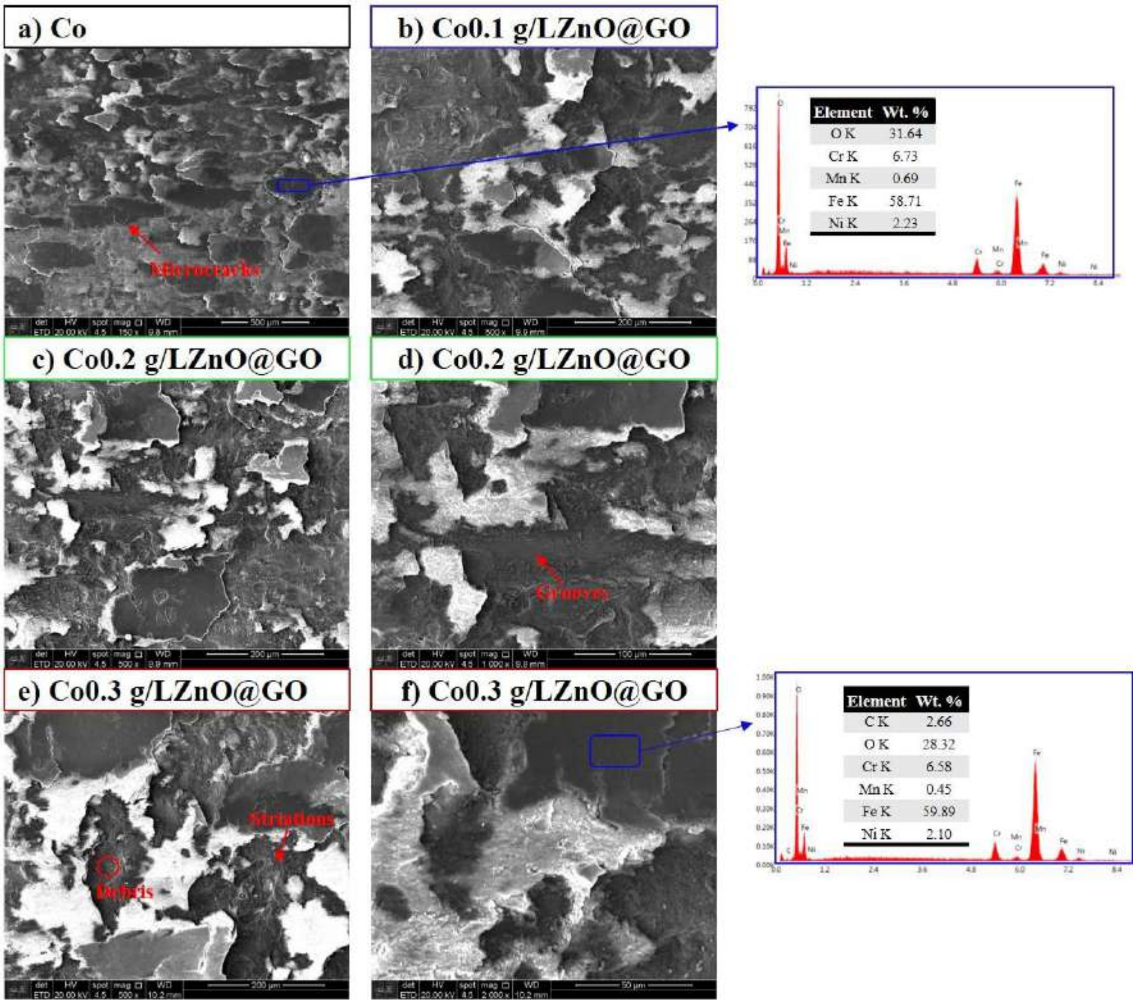

Figure 4-8 - Worn surface of (a) Co, (b) Co0.1g/L ZnO@GO, (c,d) Co0.2g/L ZnO@GO, (e,f) Co0.3g/L ZnO@GO sliding against AISI 52100 ball under a load of 500 N.

The improved tribological performance of Co composite coatings using 0.2 and 0.3 g/L of ZnO@GO addition is owing to the formation of an easy-shear oxide film, containing exfoliated GO, on the wear track. Moreover, it should be mentioned that despite there was no evidence of Zn on the wear track at the end of the test. ZnO nanoparticles could also have participated at the early stages, acting as load bearing and its effect as dispersion strengthening hinders dislocation movement. Qi et al. [28] reported the formation of oxide layer along with GO exfoliation for Ni/GO composites, which reduced in low friction coefficients.

4.5. Conclusions

In this study, the tribological behavior of CPED deposited pure Co and Co/ZnO@GO composite coatings sliding against AISI 52100 steel ball were evaluated. CPED sucessfuly produced nanostructured coatings, with high hardness and nanoparticle addition reduced surface roughness. It was observed that the incorporation of ZnO@GO core-shell nanoparticles with a content superior to 0.2 g/L can effectively increase hardness and decrease friction and wear. An oxide tribolayer was formed in all coatings, supressing friction and for higher contents of ZnO@GO, this layer entrapped exfoliated GO on the wear track, further decreasing friction and wear.

References

[1] Landolt, D. (1994). Electrochemical and materials science aspects of alloy deposition. Electrochimica Acta, 39(8-9), 1075-1090. https://doi.org/10.1016/0013-4686(94)E0022-R

[2] Mahdavi, S., & Allahkaram, S. R. (2013). Characteristics of electrodeposited cobalt and titania nano-reinforced cobalt composite coatings. Surface and Coatings Technology, 232, 198-203. https://doi.org/10.1016/j.surfcoat.2013.05.007

[3] Hyie, K. M., Resali, N. A., Abdullah, W. N. R., & Chong, W. T. (2012). Synthesis and characterization of nanocrystalline pure cobalt coating: effect of pH. Procedia Engineering, 41, 1627-1633. https://doi.org/10.1016/j.proeng.2012.07.360

[4] Parfenov, E. V., Yerokhin, A., Nevyantseva, R. R., Gorbatkov, M. V., Liang, C. J., & Matthews, A. (2015). Towards smart electrolytic plasma technologies: An overview of methodological approaches to process modelling. Surface and Coatings Technology, 269, 2-22. https://doi.org/10.1016/j.surfcoat.2015.02.019

[5] Paulmier, T., Bell, J. M., & Fredericks, P. M. (2007). Development of a novel cathodic plasma/electrolytic deposition technique: Part 2: Physico-chemical

analysis of the plasma discharge. Surface and Coatings Technology, 201(21), 8771-8781. https://doi.org/10.1016/j.surfcoat.2006.07.066

[6] Weston, D. P., Shipway, P. H., Harris, S. J., & Cheng, M. K. (2009). Friction and sliding wear behaviour of electrodeposited cobalt and cobalt–tungsten alloy coatings for replacement of electrodeposited chromium. Wear, 267(5-8), 934-943. https://doi.org/10.1016/j.wear.2009.01.006

[7] Wang, C. B., Wang, D. L., Chen, W. X., & Wang, Y. Y. (2002). Tribological properties of nanostructured WC/CoNi and WC/CoNiP coatings produced by electro-deposition. Wear, 253(5-6), 563-571. https://doi.org/10.1016/S0043-1648(02)00173-4

[8] Su, F., Liu, C., & Huang, P. (2013). Friction and wear of nanocrystalline Co and Co–W alloy coatings produced by pulse reverse electrodeposition. Wear, 300(1-2), 114-125. https://doi.org/10.1016/j.wear.2013.01.120

[9] Wang, L., Gao, Y., Xu, T., & Xue, Q. (2006). A comparative study on the tribological behavior of nanocrystalline nickel and cobalt coatings correlated with grain size and phase structure. Materials Chemistry and Physics, 99(1), 96-103. https://doi.org/10.1016/j.matchemphys.2005.10.014

[10] Rudnik, E., Burzyńska, L., & Gębka, M. (2011). Influence of CTAB cationic surfactant on codeposition of SiC particles with cobalt. Transactions of the IMF, 89(1), 33-38. https://doi.org/10.1179/174591910X12835095635187

[11] Liu, C., Su, F., & Liang, J. (2015). Producing cobalt–graphene composite coating by pulse electrodeposition with excellent wear and corrosion resistance. Applied Surface Science, 351, 889-896. https://doi.org/10.1016/j.apsusc.2015.06.018

[12] Mahdavi, S., Asghari-Alamdari, A., & Zolola-Meibodi, M. (2020). Effect of alumina particle size on characteristics, corrosion, and tribological behavior of Co/Al2O3 composite coatings. Ceramics International, 46(4), 5351-5359. https://doi.org/10.1016/j.ceramint.2019.10.289

[13] Toosinezhad, A., Alinezhadfar, M., & Mahdavi, S. (2020). Cobalt/graphene electrodeposits: characteristics, tribological behavior, and corrosion

properties. Surface and Coatings Technology, 385, 125418. https://doi.org/10.1016/j.surfcoat.2020.125418

[14] Arai, S., & Miyagawa, K. (2013). Frictional and wear properties of cobalt/multiwalled carbon nanotube composite films formed by electrodeposition. Surface and Coatings Technology, 235, 204-211. https://doi.org/10.1016/j.surfcoat.2013.07.034

[15] Zhang, Y. G., Sun, W. C., Ma, M., Tian, S. S., Liu, Y. W., & Xiao, Y. (2021). Deposition characteristics, microstructure and wear behaviour of Co–WC composite coatings. Surface Engineering, 37(6), 702-711. https://doi.org/10.1080/02670844.2020.1840694

[16] Huang, J., Zhu, J., Fan, X., Xiong, D., & Li, J. (2018). Preparation of MoS2-Ti (C, N)-TiO2 coating by cathodic plasma electrolytic deposition and its tribological properties. Surface and Coatings Technology, 347, 76-83. https://doi.org/10.1016/j.surfcoat.2018.04.059

[17] Liu, C., Zhang, S., Ji, R., Wang, P., Zhang, J., Tian, Y., ... & He, Y. (2019). Cathode plasma electrolytic deposition of Al2O3 coatings doped with SiC particles. Ceramics International, 45(4), 4747-4755. https://doi.org/10.1016/j.ceramint.2018.11.167

[18] Quan, C., Deng, S., Jiang, Y., Jiang, C., & Shuai, M. (2019). Characteristics and high temperature oxidation behavior of Ni-Cr-Y2O3 nanocomposite coating prepared by cathode plasma electrolytic deposition. Journal of Alloys and Compounds, 793, 170-178. https://doi.org/10.1016/j.jallcom.2019.04.063

[19] Hummers Jr, W. S., & Offeman, R. E. (1958). Preparation of graphitic oxide. Journal of the american chemical society, 80(6), 1339-1339. https://doi.org/10.1021/ja01539a017

[20] Baghdadi, Y. N., Youssef, L., Bouhadir, K., Harb, M., Mustapha, S., Patra, D., & Tehrani-Bagha, A. R. (2020). The effects of modified zinc oxide nanoparticles on the mechanical/thermal properties of epoxy resin. Journal of Applied Polymer Science, 137(43), 49330. https://doi.org/10.1002/app.49330

[21] Hong, J., Liu, C., Deng, X., Jiang, T., Gan, L., & Huang, J. (2016). Enhanced tribological properties in core–shell structured SiO 2@ GO hybrid fillers for epoxy

nanocomposites. RSC advances, 6(92), 89221-89230. DOI 10.1039/C6RA18207K

[22] Shankar, P., Ishak, M. H., Padarti, J. K., Mintcheva, N., Iwamori, S., Gurbatov, S. O., ... & Kulinich, S. A. (2020). ZnO@ graphene oxide core@ shell nanoparticles prepared via one-pot approach based on laser ablation in water. Applied Surface Science, 531, 147365. https://doi.org/10.1016/j.apsusc.2020.147365

[23] Ren, B., Gao, L., Li, M., Zhang, S., & Ran, X. (2020). Tribological properties and anti-wear mechanism of ZnO@ graphene core-shell nanoparticles as lubricant additives. Tribology International, 144, 106114. https://doi.org/10.1016/j.triboint.2019.106114

[24] Haghshenas, S. S. P., Nemati, A., Simchi, R., & Kim, C. U. (2019). Photocatalytic and photoluminescence properties of ZnO/graphene quasi core-shell nanoparticles. Ceramics International, 45(7), 8945-8961. https://doi.org/10.1016/j.ceramint.2019.01.226

[25] Gupta, P., Tenhundfeld, G., Daigle, E. O., & Ryabkov, D. (2007). Electrolytic plasma technology: Science and engineering—An overview. Surface and Coatings Technology, 201(21), 8746-8760. https://doi.org/10.1016/j.surfcoat.2006.11.023

[26] Quan, C., & He, Y. (2015). Microstructure and characterization of a novel cobalt coating prepared by cathode plasma electrolytic deposition. Applied Surface Science, 353, 1320-1325. https://doi.org/10.1016/j.apsusc.2015.07.080

[27] Sajjadnejad, M., Haghshenas, S. M. S., Targhi, V. T., Setoudeh, N., Hadipour, A., Moghanian, A., & Hosseinpour, S. (2021). Wear behavior of alkaline pulsed electrodeposited nickel composite coatings reinforced by ZnO nanoparticles. Wear, 468, 203591. https://doi.org/10.1016/j.wear.2020.203591

[28] Qi, S., Li, X., & Dong, H. (2019). Reduced friction and wear of electro-brush plated nickel composite coatings reinforced by graphene oxide. Wear, 426, 228-238. https://doi.org/10.1016/j.wear.2018.12.069

Chapter 5

5. Conclusion

5.1. Summary

In this work, ZnO@GO core-shell were successfully synthetized through electrostatic self-assembly of ZnO NPs positively charged with amino groups and negatively charged GO NPs. GO were also synthetized using ion-lithium batteries as precursors by a modified Hummers method. The core-shell NPs were used as additives in water-based lubricants and in Co composite coatings.

First, core-shell NPs were added to water. ZnO@GO was responsible for reducing the sliding wear of a steel/steel tribopair. When compared to water-based nanofluids which used ZnO and GO individually as additives, ZnO@GO nanofluids had a superior performance due to the formation of a long-standing graphenic protective tribo-layer. While GO undergoes a partial chemical reduction at the contact forming this tribolayer, ZnO works as a rigid skeleton increasing bearing capacity and the number of cycles that this layer is capable to withstand.

Before using ZnO@GO as additives to the Co-based coatings, CPED process was investigated. First, a CPED apparatus was developed. Then, different electrolytes were tested, focusing on examine the effect of the additive PEG on the current evolution during deposition and on the properties of produced coating. It was observed that PEG decreases density current which enables deposition on larger areas. Also, PEG influences thickness and roughness of coatings.

Regarding the deposition mechanism, it has been proposed that the actual transfer of cations to the substrate occurs on discrete pulses, when bubble implodes, electrolyte is accelerated towards the substrate, migrating metal cations. At this moment, a peak of current is observed due to the decrease of ohmic resistance. Thus, the number of peaks of current is an indirect qualitative measurement of the coating final thickness.

When ZnO@GO NPs were added to the electrolyte, the produced composite coating exhibited a decrease of grain size and surface roughness and an increase of hardness. Both coatings, pure Co and composite Co coatings have a nanocrystalline FCC metastable structure. After testing these coatings against a AISI 52100 ball in sliding wear tests, the main observable wear mechanism of delamination of the oxide layer formed on the contact. Composite coatings exhibited lower friction and wear compared to pure Co coatings due to the presence of GO on the oxide tribolayer formed on the surface.

To conclude, core-shell NPs are versatile and can be used as an excellent alternative to reduce friction and wear on coatings or lubricants. In both cases, the enhancement of tribological performance of ZnO@GO addition its associated to the formation of a graphenic tribolayer. Besides, CPED is a low cost and rapid process to produce nanocrystalline Co-based coatings with low friction and high wear resistance.

5.2. Recommendations for Future Work

For further consideration, the following points are described:

1- Water-based lubricants

- Investigate the evolution of GO partial chemical reduction on the contact during wear tests.
- Establish a relationship between GO content, I_D/I_G and friction.
- Investigate the effect of normal load on the tribological behavior of ZnO@GO-additived nanofluids. This can explain why I_D/I_G decreases while literature observed the contrary effect.

2- Cathode plasma electrolytic deposition of Co coatings

- Deposit composite coatings using an electrolyte containing PEG to investigate if PEG facilitates ZnO@GO deposition.
- Tribological test using milder contact conditions, such as lower loads. In those tests, coating detachment could possibly be hindered.
- Use a surface modifier to positively charge ZnO@GO core-shell nanoparticles to facilitate their migration toward the substrate. Investigate if this addition would increase NPs particle content on the coating.

- Include an agitation system of the electrolyte during deposition.
- Design a different sample holder to facilitate HSC camera imaging and decrease edge effects.
- Deposit coatings using ZnO and GO as additives in order to compare its effect on tribological performance with ZnO@GO.
- Use a bubble inhibiting additive such as simethicone to confirm the proposed relationship between bubble implosion, peak of current and coating thickness.
- Test composite coatings against a non-metal ball to investigate the contribution of core-shell NPs in the absence of oxide layer.